NASA CR-2631

A NUMERICAL INVESTIGATION OF SEVERE THUNDERSTORM GUST FRONTS

Kenneth E. Mitchell

Prepared by
THE PENNSYLVANIA STATE UNIVERSITY
University Park, Pa.
for George C. Marshall Space Flight Center

NATIONAL AERONAUTICS AND SPACE ADMINISTRATION • WASHINGTON, D. C. • DECEMBER 1975

TECHNICAL REPO

1. REPORT NO.	2. GOVERNMENT ACCESSION NO.	3. RECIPIENT'S CATALOG NO.
NASA CR-2635		

4. TITLE AND SUBTITLE	5. REPORT DATE
A Numerical Investigation of Severe Thunderstorm Gust Fronts	December 1975
	6. PERFORMING ORGANIZATION CODE
7. AUTHOR(S)	8. PERFORMING ORGANIZATION REPORT #
Kenneth E. Mitchell	M157
9. PERFORMING ORGANIZATION NAME AND ADDRESS	10. WORK UNIT NO.
The Pennsylvania State University Department of Meteorology	11. CONTRACT OR GRANT NO. NAS8-27334
12. SPONSORING AGENCY NAME AND ADDRESS	13. TYPE OF REPORT & PERIOD COVERED
National Aeronautics and Space Administration Washington, D. C. 20546	June 73-March 75 Contractor
	14. SPONSORING AGENCY CODE

15. SUPPLEMENTARY NOTES

This report was prepared under the technical monitorship of the Aerospace Environment Division, Space Sciences Laboratory, NASA/Marshall Space Flight Center.

16. ABSTRACT A numerical model is developed to simulate the temporal evolution and structure of the severe thunderstorm gust front. The model is a non-hydrostatic, fine resolution, cross-sectional primitive equation model. The numerical calculations are derived from the two-dimensional horizontal and vertical equations of motion, the continuity equation, and the thermodynamic energy equation. The unfiltered forms of these equations are approximated by finite differences of second order accuracy centered in time and space.

The effect of evaporative cooling in producing a vigorous downdraft is parameterized by a local cooling function. This function is applied in a unique manner that sustains a steady cold downdraft, which drives the cold outflow and associated gust front.

It is shown that two dominant factors influencing gust front configuration are surface friction and the solenoidal field coincident with the front. The circulation theorem is invoked to suggest that solenoidal accelerations oppose the deceleration of surface friction. After a downdraft is initiated in the model, it turns out that these opposing tendencies soon reach a balance and the gust front achieves a quasi-steady configuration. Thus, the experiments indicate that surface friction does not induce a cycle of front formation and collapse as limited observational evidence has previously suggested.

The magnitude of cooling in the downdraft and the ambient air stability are found to be important variables. Greater cooling in the downdraft results in a more intense gust front that exhibits stronger wind maximums and greater shears. The ambient air stability is shown to be an important factor influencing the depth of the cold outflow.

17. KEY WORDS	18. DISTRIBUTION STATEMENT
Thunderstorm Wind Profile Aircraft Response Aircraft Control System	Category 47

19. SECURITY CLASSIF. (of this report)	20. SECURITY CLASSIF. (of this page)	21. NO. OF PAGES	22. PRICE
Unclassified	Unclassified	104	$5.25

FOREWORD

This research was conducted by The Pennsylvania State University for the National Aeronautics and Space Administration, George G. Marshall Space Flight Center, Huntsville, Alabama. Dr. George H. Fichtl of the Aerospace Environment Division, Aero-Astrodynamics Laboratory, was the Scientific Monitor. Professor John A. Dutton, Department of Meteorology, The Pennsylvania State University, was the Principal Investigator. The support for this research was provided by Mr. John Enders of the Aeronautical Operating Systems Division, Office of Advanced Research and Technology, NASA Headquarters.

This research reported here was motivated by the need to understand the structure of thunderstorm gust fronts in considerable detail in order to anticipate conditions that would be encountered by aeronautical vehicles penetrating them. As explained in the report, the scarcity of the data on these phenomena made a numerical simulation of their properties particularly attractive.

This is the last in a series of three reports devoted to the effect of severe atmospheric forcing on aeronautical systems. The first report (NASA CR-2289, Variation of Low Level Winds During the Passage of a Thunderstorm Gust Front by R. W. Sinclair, R. A. Anthes, and H. A. Panofsky, 1973) discussed empirical data on the gust front. The second report (NASA CR-2361, Determination of Critical Nondimensional Parameters in Aircraft Dynamic Response to Random Input, S. E. Hillard and M. M. Sevik, 1974) developed a nondimensional model applicable to all subsonic jet transport aircraft and indicated the critical parameters to be considered in severe environments. An article on evolutionary stochastic processes, which are important in the present context, was published during the course of the investigation (Dutton, J. A., Representations for a Class of Evolutionary Stochastic Processes, Methoden und Verfahren der Mathematischen Physik, 10, 57-80, 1973.

AUTHOR'S ACKNOWLEDGMENTS

I would like to express my sincere appreciation to Dr. John B. Hovermale who first developed the numerical model adapted for use in this research, and who provided valuable guidance throughout the course of this work.

I also gratefully acknowledge the constant support and advice of Professor John A. Dutton.

Not least of all, I thank my wife, Kathy, for her patient encouragement and immeasurable assistance during the development of this thesis.

Support for this research was provided in part by the National Aeronautics and Space Administration through Contract NAS8-27334 with The Pennsylvania State University. In addition, extensive computer facilities were made available by the National Center for Atmospheric Research, which is sponsored by the National Science Foundation.

TABLE OF CONTENTS

LIST OF FIGURES

LIST OF FIGURES (Continued)

LIST OF FIGURES (Continued)

LIST OF FIGURES (Continued)

LIST OF FIGURES (Continued)

TABLE OF MATHEMATICAL SYMBOLS

A	area
c	wave phase speed
C_D	surface drag coefficient
c_p	specific heat of dry air at constant pressure
c_{s_o}	phase speed of sound wave in motionless air
c_s	phase speed of sound wave in moving air
c_V	specific heat of dry air at constant volume
C	circulation
F_r	linear diffusivity term
$F(t)$	any function of time
g	acceleration of gravity
h	length of grid domain in the z-direction
i	horizontal grid coordinate
$\underset{\sim}{i}$	unit vector in the x-direction
k	vertical grid coordinate
$\underset{\sim}{k}$	unit vector in the z-direction
K_x	horizontal diffusion coefficient
K_z	vertical diffusion coefficient
l	length of grid domain in the x-direction
L_x	wavelength measured in the x-direction
L_z	wavelength measured in the z-direction
n	superscript notation denoting the time step
o	subscript notation denoting the initial state

P	pressure
P'	perturbation pressure $P-P_o$
R	gas constant for dry air
s	distance along a closed curve
t	time
T	temperature
u	horizontal wind velocity component
V	volume
$\underset{\sim}{V}$	wind velocity vector $u\,\underset{\sim}{i} + w\,\underset{\sim}{k}$
w	vertical wind velocity component
x	horizontal coordinate in the right-handed Cartesian coordinate system
z	vertical coordinate
Δt	time step
ΔT	temperature increment
Δx	horizontal grid interval
Δz	vertical grid interval
α	specific volume
$\underset{\sim}{\eta}$	unit vector normal to a surface enclosed by a curve ($\underset{\sim}{\tau} \times \underset{\sim}{\eta}$ points away from center of enclosed surface)
Θ	potential temperature
Θ'	perturbation potential temperature $\Theta - \Theta_o$
μ	any scalar dependent variable
ν	temporal filter parameter

TABLE OF MATHEMATICAL SYMBOLS (continued)

ξ	vorticity
π	3.1416
ρ	density
ρ'	perturbation density $\rho - \rho_o$
τ	surface stress
$\underset{\sim}{\tau}$	unit vector tangent to a closed curve, pointing in the counterclockwise direction around the curve
ϕ_x	horizontal phase parameter
ϕ_z	vertical phase parameter
ψ	stream function
ω	Brunt-Vaisälä frequency
$\lvert\ \rvert$	absolute value
$\overline{(\ )}$	mean value
$\nabla(\ )$	two-dimensional Hamiltonian operator $\frac{\partial(\ )}{\partial x}\underset{\sim}{i} + \frac{\partial(\ )}{\partial z}\underset{\sim}{k}$

1.0 INTRODUCTION

The thunderstorm has awed mankind for centuries with its towering cumulonimbus clouds, spreading anvils, dramatic displays of lightning, and rumbles of thunder. It has also been a cause of concern, for the thunderstorm is one of the most destructive natural phenomena, producing intense rainshowers, hailstones, and tornadoes. Another, but often unrecognized, destructive product of the thunderstorm is the sudden, intense wind surge or gust front that develops at the surface. These gust fronts, often called "straight-line winds" to distinguish them from tornadoes, have received increased attention during the past two decades, primarily because of their effect on aircraft operations.

1.1 Statement of the Problem

A severe thunderstorm often generates a vigorous rain-cooled downdraft, which spreads out horizontally as it reaches the surface. The resulting cold outflow is led by a strong gusty wind surge, here called the gust front, which causes rapid wind speed and direction changes in the lowest 2 km of the atmosphere. The chief danger of the gust front is its sudden onslaught of high winds as much as 20 km ahead of the parent storm cell without prior warning. During frontal passage, wind speeds may increase from a relative calm to 60 knots in just five minutes and then decrease just as suddenly.

Such gust front occurrences are a major hazard to aircraft flying at low levels. The effect of sudden wind speed and direction

changes on control of an aircraft during a critical stage of take-off or landing can be disastrous. The wind surges can also cause heavy damage to utility lines, buildings, and crops.

The challenge for meteorologists is to develop the capability to predict the occurrence, intensity, and position of these gust fronts using readily available rawinsonde, satellite, radar, and surface observations. This is a formidable problem as most observations are obtained on time and space scales much larger than the scale of the gust front. The cold outflow associated with a gust front is on the order of 10 km long and 2 km deep with a duration of about an hour (Charba, 1972).

Several previous efforts to predict gust front variables have attempted, statistically or empirically, to relate large scale parameters to small scale events. Foster (1958) proposed a technique of calculating downdraft velocities based on a buoyancy equation, and then correlated them to peak wind gusts at the surface. The correlation coefficient was disappointingly small. Sinclair (1973), in a step-up multiple linear regression procedure, considered combinations of parameters, rather than a single one, as predictors of the maximum surface wind gust. However, the statistically significant parameters in the resulting regression equation explained only 34 percent of the variance of peak gusts, and therefore were of limited use in prediction. The conclusions from these and similar studies are less than encouraging and serve to emphasize the lack of complete understanding of the complex mechanisms of the gust front.

The gaps in our knowledge of gust front structure derive from the scarcity of data, which again is a result of the small scale of the

phenomenon. Only a high density surface observation network can resolve the surface features of a gust front. Furthermore, data on the vertical structure of gust fronts is woefully lacking. It can be obtained from a few instrumented wind towers, but these have limited potential due to their restricted height and fixed position. Aircraft measurements, although ideal in principle, are very difficult on an operational basis and too costly in most cases. Radar and other remote sensing devices hold promise, but are largely untried in this application. Gust front data, then, is restricted at best, and consequently so is our understanding. Thus, successful prediction schemes can only be anticipated after a more rigorous definition of gust front processes is achieved.

1.2 Approach to the Problem

A numerical model is utilized here in an effort to partially overcome the present limitations in gust front data and to obtain more information on the structure and mechanism of the gust front phenomenon.

In brief, the numerical model used is a non-hydrostatic, high resolution, two-dimensional primitive equation model. The calculations are made with the two-dimensional primitive equations, including the horizontal and vertical equations of motion, the continuity equation, and the thermodynamic energy equation. The non-hydrostatic, unfiltered forms of these equations are approximated by finite differences centered in time and space using the semi-momentum differencing scheme.

In order to study the small scale motions of the gust front circulation, these equations are applied on a fine resolution grid system that has 40 vertical levels spaced 175 m apart (providing a

total model depth of about 7 km), along with a horizontal grid spacing of approximately 230 m extending over a total horizontal distance of 16 km.

The basic technique is to develop a steady downdraft of cold dense air within the model, and then study the temporal evolution of the gust front that develops as this cold downdraft spreads out at the lower surface. A typical gust front circulation is determined by a number of model integrations; then, several parameters are varied individually to indicate the role each one might play in governing a gust front's configuration and severity.

2.0 DEVELOPMENT OF THE NUMERICAL MODEL

The most important questions left unanswered by gust front data now available are concerned with the vertical structure of gust front motions. Surface observations provide little insight; and, although a fair amount of high resolution wind tower data is available, instrumented towers reach to heights that, in general, represent only a small fraction of total gust front depths. However, the present model simulates the motion patterns within a complete vertical cross section of the thunderstorm cold outflow, and thus serves to partly compensate for the low-altitude bias in gust front observations.

2.1 Basic Characteristics of the Model

The model is a non-hydrostatic, unfiltered primitive equation model. It allows not only the gravity waves of interest here, but also sound waves, whose presence necessitates a very short time step to maintain computational stability. An alternative approach might have been to make certain scale assumptions, consistent with deep or shallow convection, to modify the system of equations. However, with the gust front phenomenon, there is uncertainty as to what the appropriate scale assumptions should be. The unfiltered primitive equations, then, are a reasonable choice in a first attempt to model the gust front phenomenon; and furthermore, are desirable because of their straightforwardness.

2.1.1 System of Equations. The model is integrated over a domain in the x-z plane of a Cartesian coordinate system. The gust front motions are assumed to be two-dimensional in the x-z plane and homogeneous

throughout the lateral y-direction. All v wind components and all y derivatives are thus set to zero in the model equations. In addition, the Coriolis force is ignored in the momentum equations since the Rossby number is large on the gust front scale.

The forcing in the model is provided by a simulated cold downdraft. Although evaporative cooling initiates the cold downdraft in the atmosphere, no explicit treatment of water vapor is included in the model equations. Instead, downdraft generation is parameterized since the detailed microphysics of evaporative cooling are not of interest.

The treatment of the boundary layer is rather simple. No attempt is made to specify non-linear eddy viscosity terms in the equations. Instead, surface friction is modeled by a bulk aerodynamic drag applied at the lowest level. Vertical diffusion of momentum between the surface and levels above is accomplished by the Fickian or linear diffusion terms that are added to the equations to maintain computational stability.

With these considerations, the analytic equations including the u and w component equations of motion, the thermodynamic energy equation, and the complete form of the continuity equation are

$$\text{(1)} \qquad \frac{\partial u}{\partial t} + u\frac{\partial u}{\partial x} + w\frac{\partial u}{\partial z} + \frac{1}{\rho}\frac{\partial P}{\partial x} + F_r(u) = 0 \quad ,$$

$$\text{(2)} \qquad \frac{\partial w}{\partial t} + u\frac{\partial w}{\partial x} + w\frac{\partial w}{\partial z} + \frac{1}{\rho}\frac{\partial P}{\partial z} + g + F_r(w) = 0 \quad ,$$

$$\text{(3)} \qquad \frac{\partial P}{\partial t} + u\frac{\partial P}{\partial x} + w\frac{\partial P}{\partial z} + \frac{c_p}{c_v} P \left(\frac{\partial u}{\partial x} + \frac{\partial w}{\partial z}\right) + F_r(P) = 0 \quad , \text{ and}$$

$$\text{(4)} \qquad \frac{\partial \rho}{\partial t} + u\frac{\partial \rho}{\partial x} + w\frac{\partial \rho}{\partial z} + \rho \left(\frac{\partial u}{\partial x} + \frac{\partial w}{\partial z}\right) + F_r(\rho) = 0 \quad .$$

This set of equations forms a complete system in the dependent variables u, w, P, and ρ, which are functions of the independent variables x, z, and t. The F_r term in each equation represents the linear diffusivity term, which will be explicitly formulated in a later section (See Table of Mathematical Symbols for definition of all terms).

The temperature, T, is recovered from the equation of state for dry air given by

$$T = \frac{P}{\rho R} \quad , \tag{5}$$

and the potential temperature, Θ, is obtained from Poisson's equation which is

$$\Theta = T\left(\frac{1000}{P}\right)^{R/c_p} \tag{6}$$

2.1.2 Finite Difference Scheme. The terms in equations (1) - (4) are approximated by finite differences and the system is then integrated numerically in time. The finite difference method used is the centered-in-space, centered-in-time, semi-momentum scheme. This differencing scheme was developed by F. G. Shuman (1962), and is currently employed in the National Meteorological Center's operational six-layer primitive equation model (Shuman and Hovermale, 1968).

When applied to an inviscid form of (1) - (4), this scheme conserves mass and energy exactly in the interior of the grid, with some negligible error at the top and bottom boundaries. The error at the boundaries is especially negligible for models, such as the present one, that have high vertical resolution. Addition of the friction terms makes

the scheme somewhat nonconservative, but over the longest periods of integration, the net changes of mass and energy in the model are very small.

In the semi-momentum scheme, space derivatives are calculated with an average centered difference within a grid box to obtain a time tendency representative of that grid box. Then, the tendency values from four adjacent boxes are averaged to obtain a mean tendency for the grid point that is common to all four grid boxes. The centered-in-time or leapfrog scheme is then used to integrate these tendencies forward in time.

This method is more successful in suppressing computational instability than most other schemes, and does so without damping wave amplitude. As a result, the implicit numerical diffusion often found in other differencing schemes is not present. However, this scheme does produce some phase lags, and hence some wave speeds in the model are somewhat less than their true values.

In order to ensure computational stability, the stability criterion $c\Delta t/\Delta x < 1$ must be satisfied. The phase speed equation that can be derived from a linear perturbation analysis of (1) - (4) shows that the maximum wave speed allowed in the present model is given by

$$(7) \qquad c_s = |\underset{\sim}{V}|_{max} + \left(\frac{c_P}{c_V} P T_{max} \right)^{1/2} \quad ,$$

which is the speed of sound in dry air moving at velocity $\underset{\sim}{V}$. Therefore, the time step is taken as

$$(8) \qquad \Delta t = \min \left\{ \frac{0.70\ \Delta x}{c_{s_o} + |u|_{max}} \right. , \left. \frac{0.70\ \Delta z}{c_{s_o} + |w|_{max}} \right\}$$

where c_{s_o} is 350 m/sec (the speed of sound in still air at 308 K) and u_{max} and w_{max} are the maximum anticipated horizontal and vertical velocities respectively.

Thus, for the previously given $\Delta z = 175$ m and $\Delta x = 230$ m, Δt is on the order of 0.35 seconds. It is recognized that this is an extremely short time step, which is of course the main, and maybe only, disadvantage of using the unfiltered, non-hydrostatic equations in the present application. The factor 0.70 is used instead of 1.0 in (8) as a precaution against the possibility of boundary effects producing instability in cases where $c\Delta t/\Delta x$ approaches one.

To further maintain computational stability, some mechanism is required to control non-linear aliasing and computational growth of short wavelengths. Thus, linear or Fickian diffusion terms, represented by F_r in (1) - (4), are added to damp short wavelengths. For a given dependent variable, μ, the diffusion term is formulated analytically as

$$(9) \qquad F_r(\mu) = K_x \frac{\partial^2 \mu}{\partial x^2} + K_z \frac{\partial^2 \mu}{\partial z^2} ,$$

where K_x and K_z are constant coefficients. Typically, in the interior of the model grid, the effective diffusion coefficients are

$$(10) \qquad K_x = 2.25 \times 10^6 \text{ cm}^2/\text{sec}$$

$$(11) \qquad K_z = 1.25 \times 10^6 \text{ cm}^2/\text{sec} .$$

At the boundaries, K_x and K_z are set to zero to prevent the possible generation of spurious waves.

The diffusion terms in the model are represented by a difference scheme that is forward in time and centered in space to ensure computational stability. Also, the terms are formulated so that the amplitude of a $2\Delta x$ wave is damped by the same percentage as that of a $2\Delta z$ wave. This explains the somewhat large value for K_z and the rather small value for K_x, and furthermore, emphasizes that the diffusion terms were added for computational purposes and not as an attempt at eddy viscosity parameterization.

2.1.3 Boundary Conditions. The model is integrated with a flat, rigid, and free-slip lower boundary at $z = 0$ where $w = 0$ and $\partial u/\partial z = 0$. The free-slip condition is desired here because a gust front is characterized by strong winds at the surface. These strong winds prevail much closer to the surface than one vertical grid interval in this model. The no-slip condition, $u = 0$, would have prevented strong surface winds. The free-slip formulation with a surface drag parameterization gives the model extra freedom at the lower boundary.

Surface drag was modeled by a bulk aerodynamic stress term that was added to (1) at the lowest grid level only. This stress term is given at level 1 by

$$\tau/\rho = \frac{C_D \, |u_1| \, u_1}{\Delta z} \quad , \tag{12}$$

where C_D is constant and represents the average drag coefficient over the depth of the first grid layer. This simplified form of drag is meant to emphasize the effects of drag at the ground only. It should

also be noted that this term, like the linear diffusion terms, is integrated using a forward time step to maintain computational stability.

Pressure at the lower boundary is determined hydrostatically from the pressure at the next level above by

$$(13) \qquad p_1^n = p_2^n + g \frac{(\rho_1^n + \rho_2^n)}{2} \Delta z \quad ,$$

where n represents the time step and subscripts 1 and 2 refer to the first and second grid levels respectively. However, the model is only hydrostatic in this lowest layer and similarly in the uppermost layer.

The time tendency of density at the lower boundary is determined by the tendency of the next higher level by

$$(14) \qquad \rho_1^n = \rho_1^{n-1} + (\rho_2^n - \rho_2^{n-1}) \quad .$$

This technique results in surface temperatures being essentially determined by advection. No mechanism is included that allows the surface to act as a heat source or sink and subsequently modify the air above it by turbulent transfer or diffusion. This is entirely reasonable in this application because in the region of an active gust front and associated cold outflow, surface temperature changes due to cold advection overwhelmingly dominate changes due to turbulent heat transfer from the ground within the time span of an active gust front.

The upper boundary conditions at z = h are analogous to those just described for the lower boundary. Only the lower half of the troposphere is considered and the model is truncated at a height of 7.0 km

by a rigid, flat, free-slip lid with $w = 0$ and $\frac{\partial u}{\partial z} = 0$. Pressure is determined hydrostatically from the pressure of the next lower level by

$$(15) \qquad P_k^n = P_{k-1}^n - g \frac{(\rho_k^n + \rho_{k-1}^n)}{2} \Delta z \quad ,$$

where k is the topmost grid level in this case. The time tendency of density at the top boundary is determined by the tendency of the next lower level by

$$(16) \qquad \rho_k^n = \rho_k^{n-1} + (\rho_{k-1}^n - \rho_{k-1}^{n-1}) \quad .$$

Due to obvious computational limitations, it is necessary to truncate the horizontal domain of the model at $x = 0$ and $x = \ell$, where some artificial boundary conditions need to be introduced. Rigid, free-slip boundaries are imposed, across which there are no horizontal density or pressure gradients. Thus, the boundary conditions at $x = 0$, ℓ are

$$(17) \qquad u = 0 \quad , \qquad \frac{\partial w}{\partial x} = 0 \quad ,$$

$$(18) \qquad \frac{\partial P}{\partial x} = 0 \quad , \text{ and } \frac{\partial \rho}{\partial x} = 0 \quad .$$

In general, mass conservation constraints are more easily satisfied with rigid walls than with open boundaries. More specifically, the mass conserving property of the semi-momentum differencing scheme, which is used in this model, is easily preserved on rigid boundaries by the given conditions on P and ρ.

2.1.4 Introduction of a Temporal Filter. The system of equations integrated by this model allows sound waves, but they are of no interest in the present work. Therefore, a high frequency filter is utilized to effectively damp the high frequency sound wave modes. For any function of time, F(t), the filtered function, $\overline{F(t)}$, is obtained by

$$\overline{F(t)} = F(t) + 0.05\,\nu\,[\overline{F(t-\Delta t)} - 2F(t) + F(t+\Delta t)] \quad , \tag{19}$$

where the overbar indicates the filtered value of the function and ν is the filter parameter. This filter was shown by Asselin (1972) to have a response function that discriminates well between frequencies. It effectively damps high frequency motions while damping low frequency motions only slightly.

The value of the ν parameter that gives the optimum response function is dependent on the time step, Δt, and the frequency of the oscillations to be damped. In this model, the filter function with $\nu = 0.50$ rapidly damps the sound modes, while leaving the relatively low frequency internal gravity wave solutions of interest virtually untouched. This filter function also provides excellent control of the computational mode arising from the centered-in-time integration scheme.

2.1.5 Introduction of Streamlines and Trajectories. As aids in the analysis and interpretation of model results, both the streamline flow pattern and air parcel trajectories are calculated. Kinematic trajectories of several air parcels are obtained by a forward integration in time of the parcel velocity components as determined by a double linear extrapolation within the appropriate grid box. The details of these calculations are analogous to those described by Schlesinger (1973).

Streamlines are derived from a streamfunction, ψ (x,z), defined by

$$(20) \qquad u = -\frac{\partial \psi}{\partial z} \qquad \text{and} \qquad w = \frac{\partial \psi}{\partial x} \quad .$$

The streamfunction is calculated using a Liebmann over-relaxation technique as described by Haltiner (1971) to solve the elliptic equation

$$(21) \qquad \frac{\partial^2 \psi}{\partial x^2} + \frac{\partial^2 \psi}{\partial z^2} = \left(\frac{\partial w}{\partial x} - \frac{\partial u}{\partial z}\right) \quad ,$$

where ψ is set to zero on the boundaries. This is Poisson's equation, with the right side known from the given velocity fields.

It is recognized that ψ represents only the rotational part of a flow field that is composed of both rotational and divergent components. However, an analysis of (1) - (4) with the non-divergent assumption, $\frac{\partial u}{\partial x} + \frac{\partial w}{\partial z} = 0$, in place of the full continuity equation, shows that this new system of equations permits all the gravity wave modes of the original system, but does not allow the sound wave modes.

It follows, then, that in the present model the divergent component of the flow must be associated almost entirely with the sound waves which are being damped. The gravity waves, therefore, are represented well by the irrotational component of the flow and thus the streamfunction depicts the gravity wave solutions accurately.

2.2 Application of the Model to the Gust Front Phenomenon

It has been shown by Browning (1964), Newton (1966), and others that severe thunderstorms existing in a strongly sheared environment are often comprised of an intense tilted updraft and a vigorous rain-cooled downdraft coexisting in a quasi-steady state. Such updraft-downdraft couplets are comprised of interdependent but separate circulations. In fact, it is the separate nature of the updraft and downdraft that enable them to persist for long periods of time.

In this study, however, we are not concerned with all the circulations associated with a large cumulonimbus cell. Rather, we are only interested in the details of the wind structure within gust fronts that are produced by severe thunderstorm downdrafts. Accordingly, the present model focuses on the separate downdraft circulation in the lower half of the troposphere.

Schlesinger's (1973) numerical model of moist, deep convection serves to further illustrate the small part of the thunderstorm being modeled here. Figure 1 is an example of the flow pattern that develops during the mature stage of a thunderstorm, as derived from a typical integration of Schlesinger's model. A shallow reverse eddy is evident in the low levels behind the cloud stem (boxed-in in Figure 1).

This eddy represents the circulation associated with the downdraft. Schlesinger noted that the intensity of this separate downdraft circulation diminished for larger values of low-level relative humidity because the potential for evaporative cooling was reduced. In addition, Schlesinger pointed out that the accelerated horizontal flow at the surface associated with this downdraft eddy might well

represent the gust front; but, he also emphasized that the resolution of his model was too crude to depict the structure of the gust front in any detail.

The present model, however, simulates only the downdraft circulation and therefore is able to resolve the details of the gust front generated in that part of the thunderstorm circulation represented by the boxed-in region of Figure 1.

2.2.1 The Initial State of the Model. The vertical temperature profile for the initial state in the model is taken from actual sounding data obtained near Fort Morgan, Colorado, on a day during which four severe convective storms occurred within the local area. The soundings were taken in ambient regions around the storms by members of the National Hail Research Experiment of the National Center for Atmospheric Research.

The initial state pressures are determined by hydrostatically integrating the vertical temperature profile. The resulting initial state sounding is shown in Figure 2. The low surface pressure is due to Fort Morgan's 1378 m height above sea level. The model integrations also start from a state of rest. Thus, the effect of an ambient wind shear on an imbedded cold outflow circulation is not considered. Initially, then, the dependent variables are specified as

$$-\frac{\partial \ln P_o}{\partial z} = \frac{-g}{RT_o} \quad , \tag{22}$$

$$\rho_o = \frac{P_o}{RT_o} \quad , \tag{23}$$

$$\frac{\partial P_o}{\partial x} = \frac{\partial \rho_o}{\partial x} = \frac{\partial T_o}{\partial x} = 0 \quad , \text{ and} \tag{24}$$

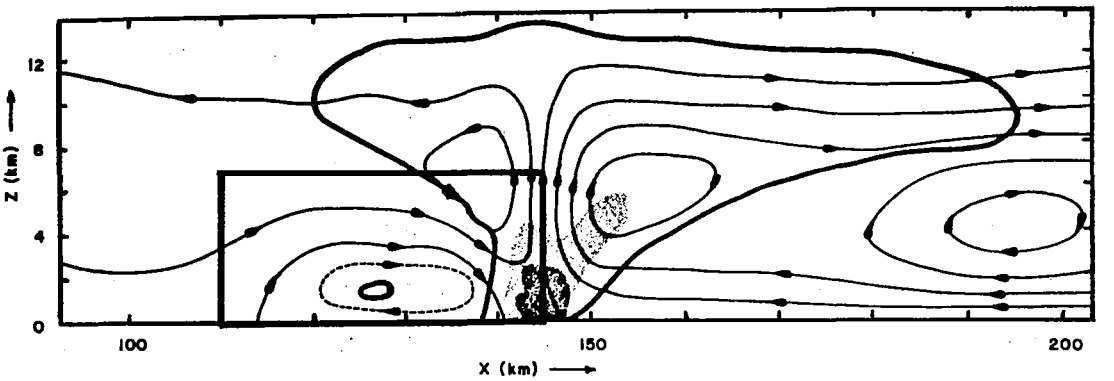

Figure 1. A representative result from Schlesinger's model of moist, deep convection. The boxed-in region outlines the downdraft circulation.

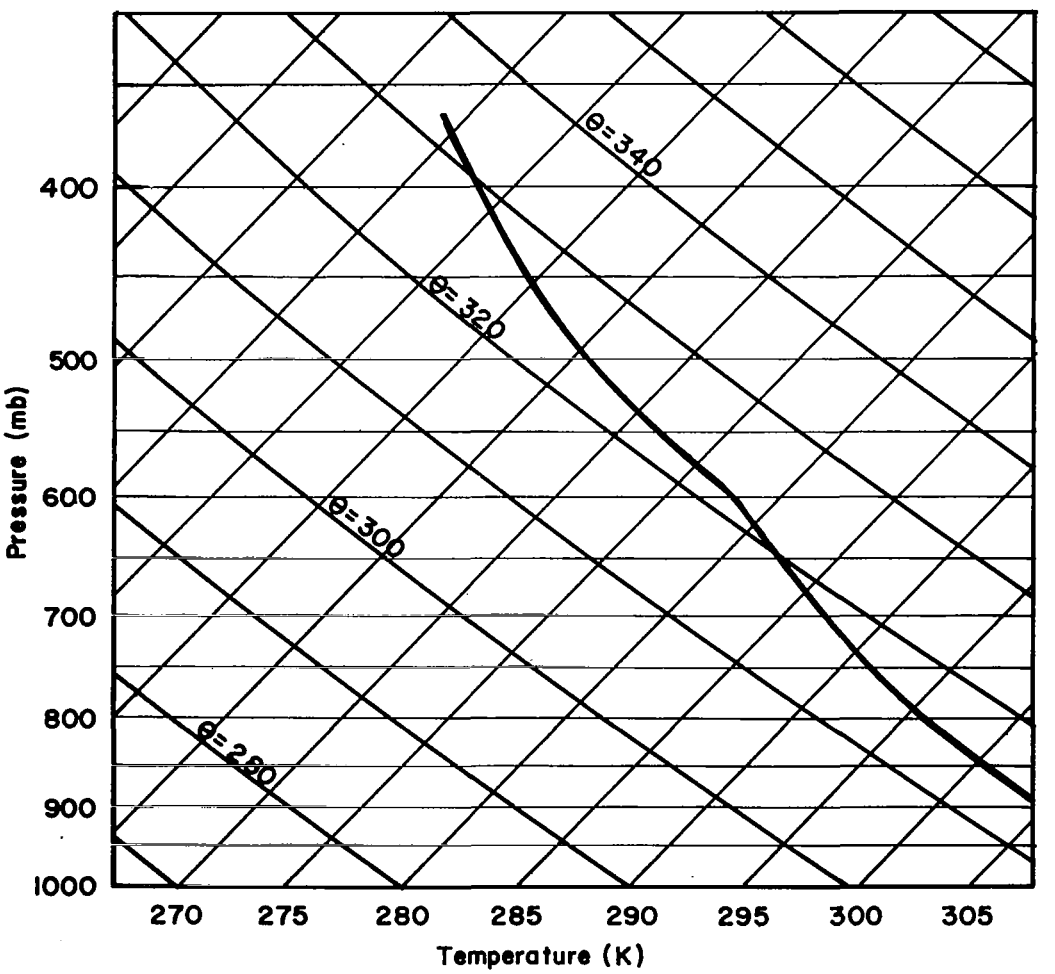

Figure 2. Skew T-Log P diagram showing the initial ambient temperature profile.

$$u_o = w_o = 0 \tag{25}$$

where the zero subscript indicates the initial state.

2.2.2 Parameterizing the Cold Downdraft. An organized circulation is initiated in the model by parameterizing a cold downdraft. Again, the microphysical details of evaporative cooling are not of interest. Rather, the model generates cold dense air by arbitrarily imposing local cooling.

This local cooling is accomplished by subtracting a small increment of temperature from the temperature values at predetermined grid points according to the relation

$$T^n_{i,k} = \frac{p^n_{i,k}}{R\,\rho^n_{i,k}} - \left[\cos\frac{2\pi}{L_z}\Delta z\,(k-\phi_z)\,\cos\frac{2\pi}{L_x}\Delta x\,(i-\phi_x)\right]\Delta T \quad , \tag{26}$$

where n indicates the time step and i and k specify the horizontal and vertical grid coordinate respectively. Accordingly, the density values at these grid points are adjusted to account for this local cooling by

$$\rho^n_{i,k} = \frac{p^n_{i,k}}{R\,T^n_{i,k}} \quad . \tag{27}$$

Although the cooling effect at a given time step first appears in the density field, the integration process, through interaction of the vertical equation of motion with the rest of the system, spreads the influence of the cooling rapidly to the pressure and u velocity fields as well.

The cooling function in (26) is applied at each time step during approximately the first half minute of each experiment. The resulting "cold blob" is illustrated in the potential temperature field of Figure 3. The L_z and L_x parameters in (26) specify the vertical and horizontal wavelengths of the cold blob respectively, while ϕ_z and ϕ_x are phase parameters that determine the position of the cold blob within the grid.

The value of ϕ_x is the same in all experiments and is chosen so that the maximum temperature depression always occurs at the left edge of the domain. Thus, the resulting downdraft always occurs within the far left portion of the grid. Specifying the cold air source in this manner implicitly assumes that the resulting cold outflow is symmetric about the downdraft. This assumption requires us to model only half of the symmetric circulation. We thereby gain additional horizontal extent without sacrificing resolution. This symmetric assumption makes additional sense since no ambient wind shear is included.

Larger magnitudes of cooling are obtained by simply applying the cooling function over a longer time, that is, more time steps. This is done so that ΔT in (26) can be kept relatively small (about 0.33 K), thereby reducing the shock effect of the instantaneous cooling and inhibiting the growth of sound waves. In Figure 3, the cooling function has been applied at each time step during the first 0.40 minutes of the model integration and has produced a maximum temperature depression of 10 K.

After the cold blob is generated, the density values of the grid points above the potentially coldest level of the blob are held

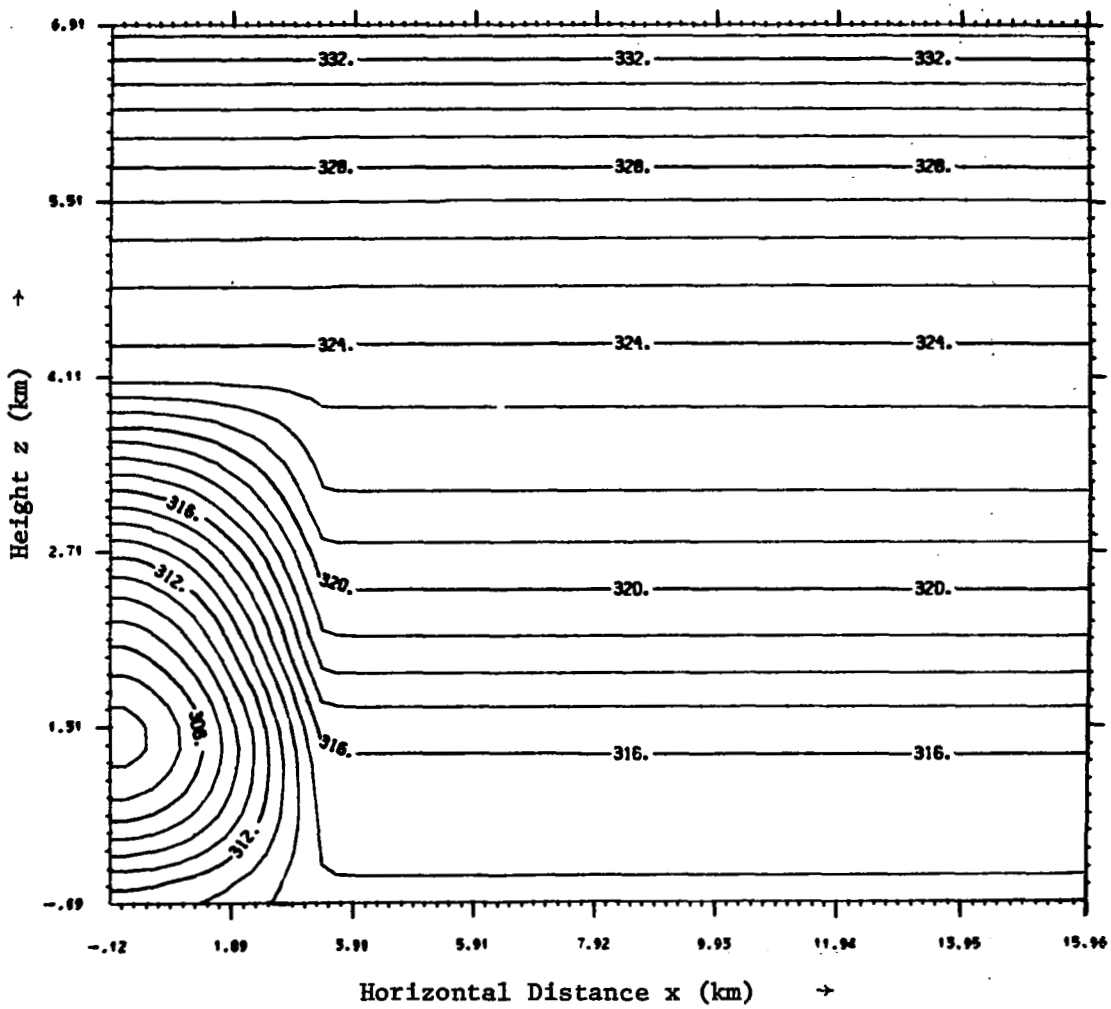

Figure 3. Potential temperature field (K) at 0.40 minutes illustrating the local cooling produced by applying equation (26) at each time step during the initialization. The maximum temperature depression is 10 K.

constant. The potential temperatures for the upper portion of the cold blob are thus effectively held fixed because pressure variations turn out to be small. This can be seen by expressing a form of Poisson's equation in perturbation notation as

$$\frac{\Theta'}{\Theta_o} = \frac{c_V}{c_P}\frac{P'}{P_o} - \frac{\rho'}{\rho_o} \quad , \tag{28}$$

where Θ', ρ', and P' are deviations from the basic initial state. It turns out that

$$\left|\frac{P'}{P_o}\right| << \left|\frac{\rho'}{\rho_o}\right| \quad , \quad \text{thus} \tag{29}$$

$$\frac{\Theta'}{\Theta_o} \simeq - \frac{\rho'}{\rho_o} \quad , \tag{30}$$

where << implies a factor of 1/10. Thus by holding ρ'/ρ_o constant in the upper half of the cold blob, Θ'/Θ_o essentially remains constant.

In Figure 4, which is the result of integrating the initial state in Figure 3 out to 12.0 minutes, the boxed-in area shows the grid region in which the potential temperatures are arbitrarily held fixed by the model. This region of fixed temperatures has been maintained throughout the 12.0 minute integration. It is obvious that some "noise" is generated at the edges of the region of fixed temperatures. However, no apparent computational problems resulted from this, further illustrating the computational stability of the model.

By 12.0 minutes (Figure 4), a cold outflow has developed at the surface and a sharp temperature front has formed at its forward edge.

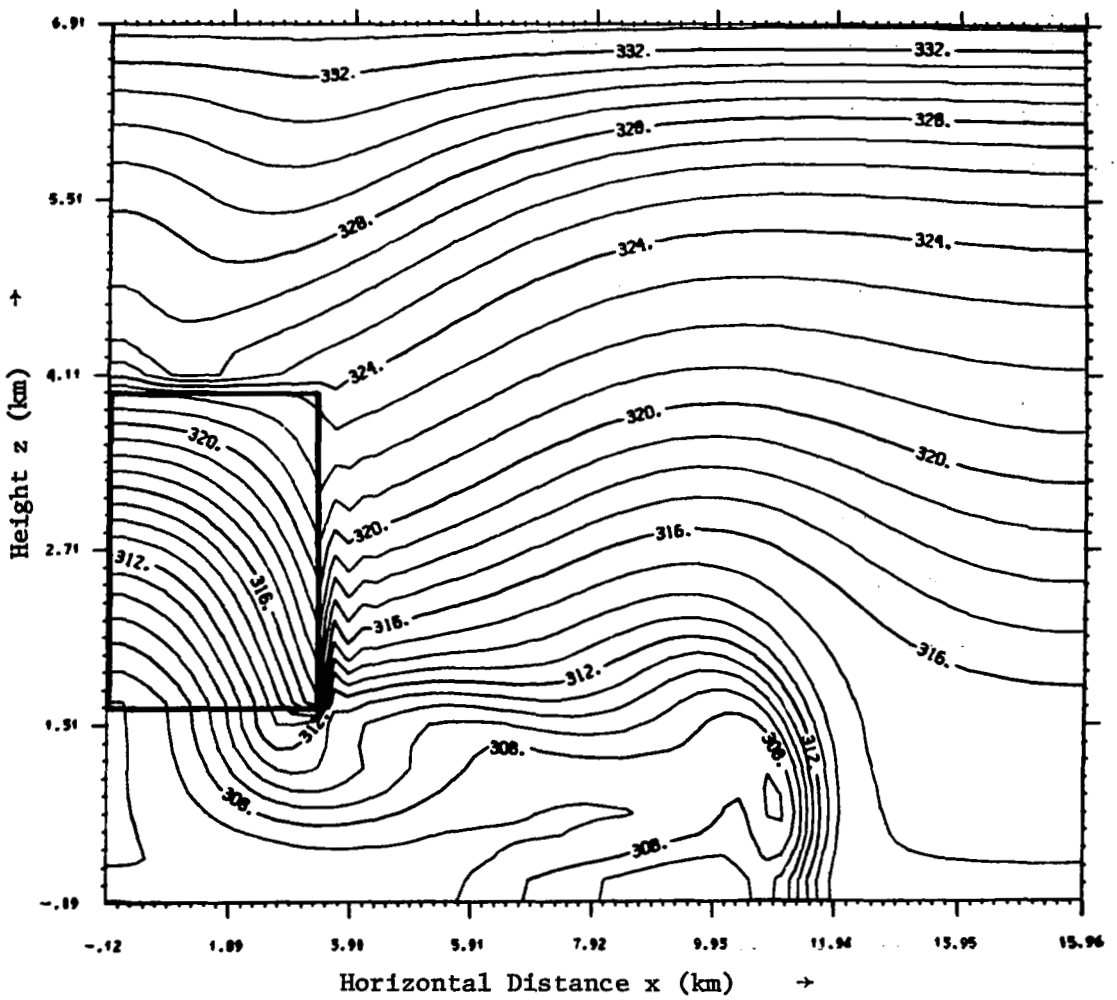

Figure 4. The potential temperature field (K) at 12.00 minutes showing the strong cold outflow outlined by the 314 K isotherm. The boxed-in region indicates where the potential temperatures are held fixed.

Figure 5 illustrates how this cold outflow is maintained by air parcels that have been cooled in the parameterized downdraft.

In Figure 5, the kinematic trajectories of certain air parcels are shown. Each parcel trajectory represents the displacement of a parcel from its initial position (Figure 3) to its final position (Figure 4). Since each trajectory represents the same amount of travel time, the longer trajectories represent the fastest moving parcels.

The parcel trajectory labeled C-D is representative of those parcels entering the top of the downdraft region with potential temperatures near 324 K. These air parcels are quickly cooled as they rapidly accelerate downward in the cold downdraft and take on the lower values of the potential temperatures maintained there. Eventually these parcels are cooled to as low as 306 K before exiting the region of fixed temperatures. Then, they conserve their low potential temperatures as they continue to subside and eventually encounter the lower boundary, where they begin to spread out horizontally to form the cold surge.

The cold surge thus formed propagates rapidly outward and is maintained by the continuous source of cold air supplied by the steady downdraft. This cold downdraft parameterization is very useful in that is produces a steady convective downdraft without specific attention to water vapor.

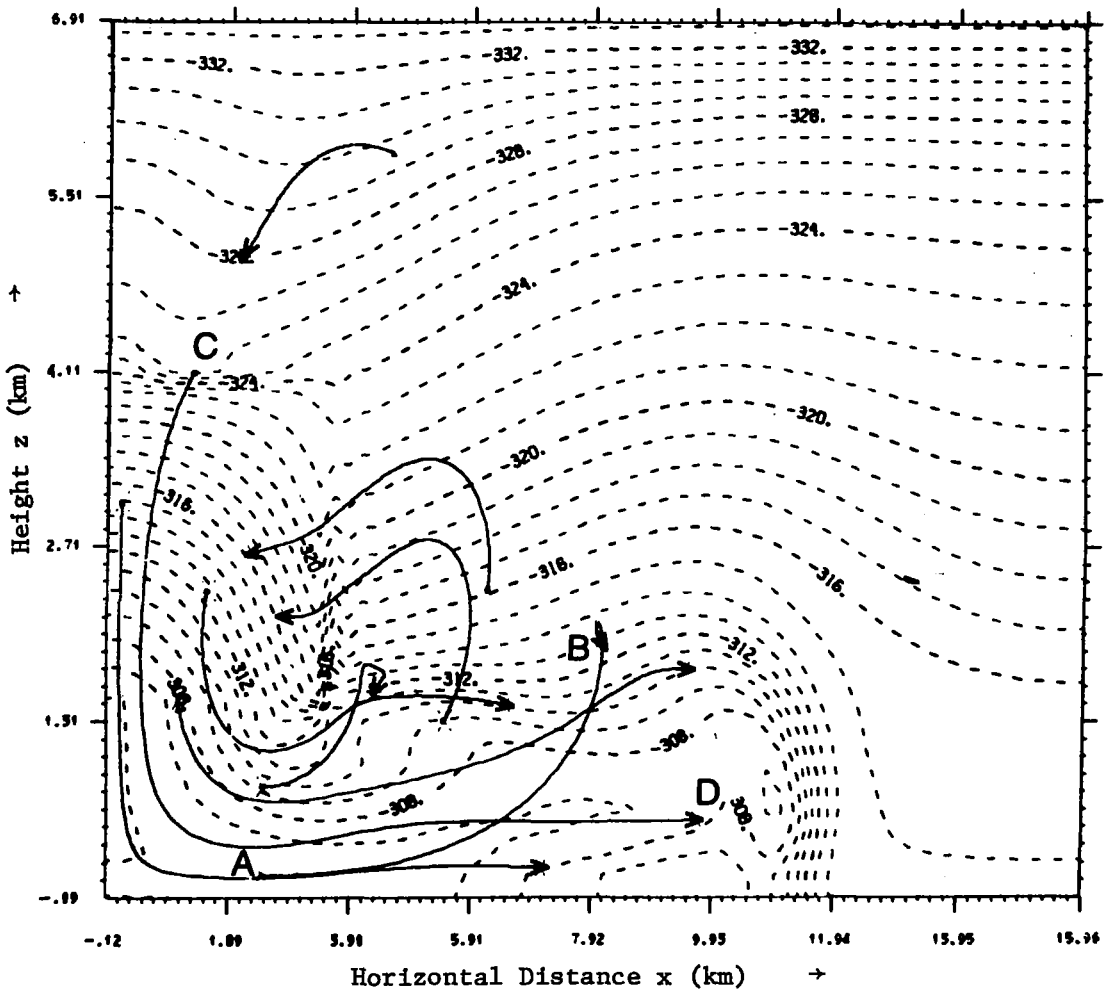

Figure 5. Kinematic trajectories showing the paths traversed by certain air parcels between 0.40 minutes and 12.00 minutes. The dashed contours represent the potential temperature field of Figure 4.

3.0 EVOLUTION OF THE GUST FRONT

The development of a typical gust front is presented in this chapter in order to illustrate certain features that were common to all model trials and to establish nomenclature to be used throughout. In particular, the following two aspects of gust front development are emphasized: 1) the gust front is the result of a direct circulation, and 2) the gust front in its mature stage is characterized by a distinct, quasi-steady configuration.

3.1 Development of a Direct Circulation

The local cooling during the initialization process (Figure 3) produces a high pressure dome (Figure 6) at the surface due to the hydrostatic weight of the cold dense air. Such a high pressure dome is commonly observed under the cold downdrafts of severe thunderstorms (Fujita, 1959). The stage is then set for the development of a direct circulation, in which geopotential energy is converted to kinetic energy, as the cold dense air sinks and the large surface pressure gradient generates strong horizontal winds flowing outward from the center of the downdraft in the low levels.

The beginning of the circulation is apparent in Figures 7 and 8, which show the rapidly developing downdraft with the accompanying pattern of inward horizontal winds at high levels and outward horizontal winds at low levels. By 6.0 minutes, a sharp temperature front (Figure 9) has formed at the forward edge of the cold air surging outward from the lower portion of the now vigorous downdraft evident in Figure 10. This cold surge induces strong upward motion

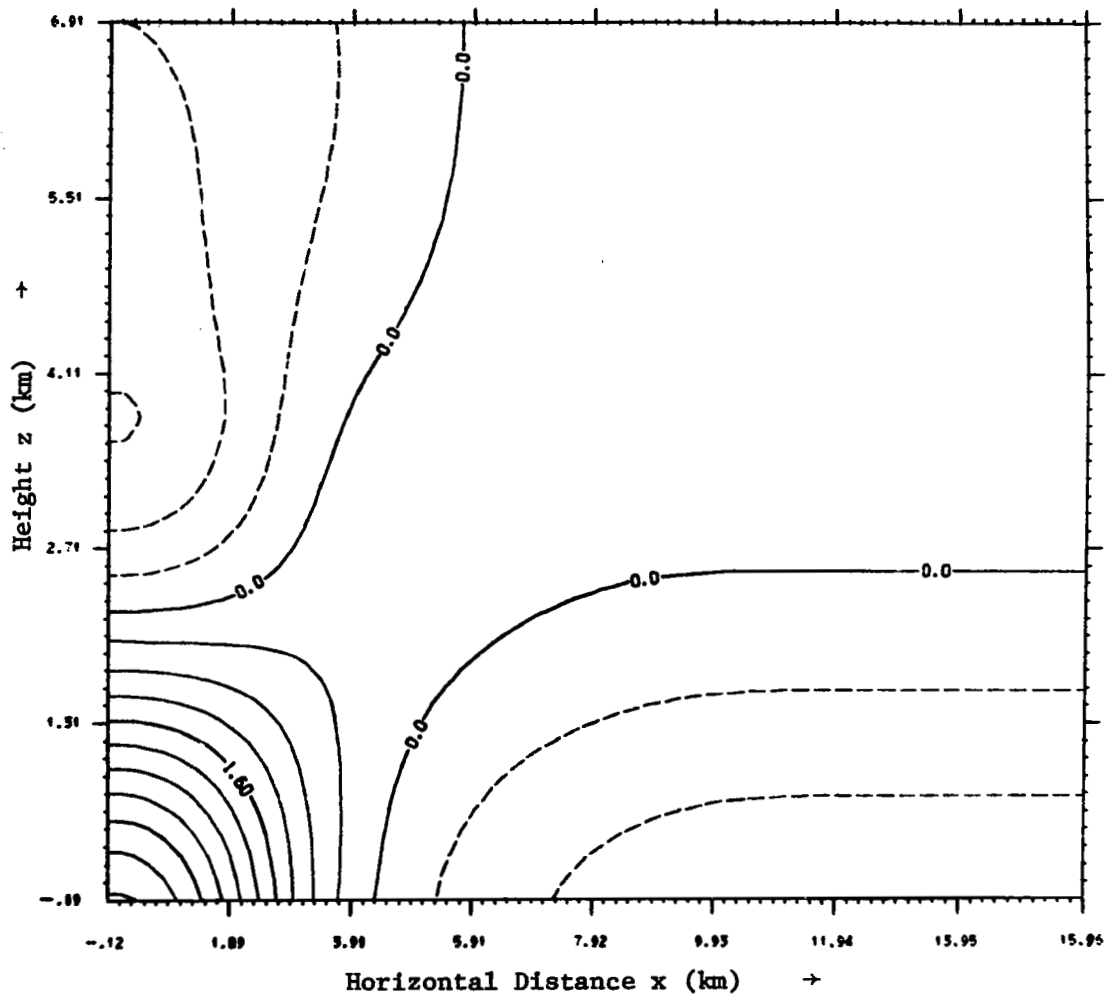

Figure 6. Pressure deviations (mb) from a mean value at each level at 0.40 minutes when initialization is complete. Solid contours at intervals of 0.40 mb indicate positive deviations.

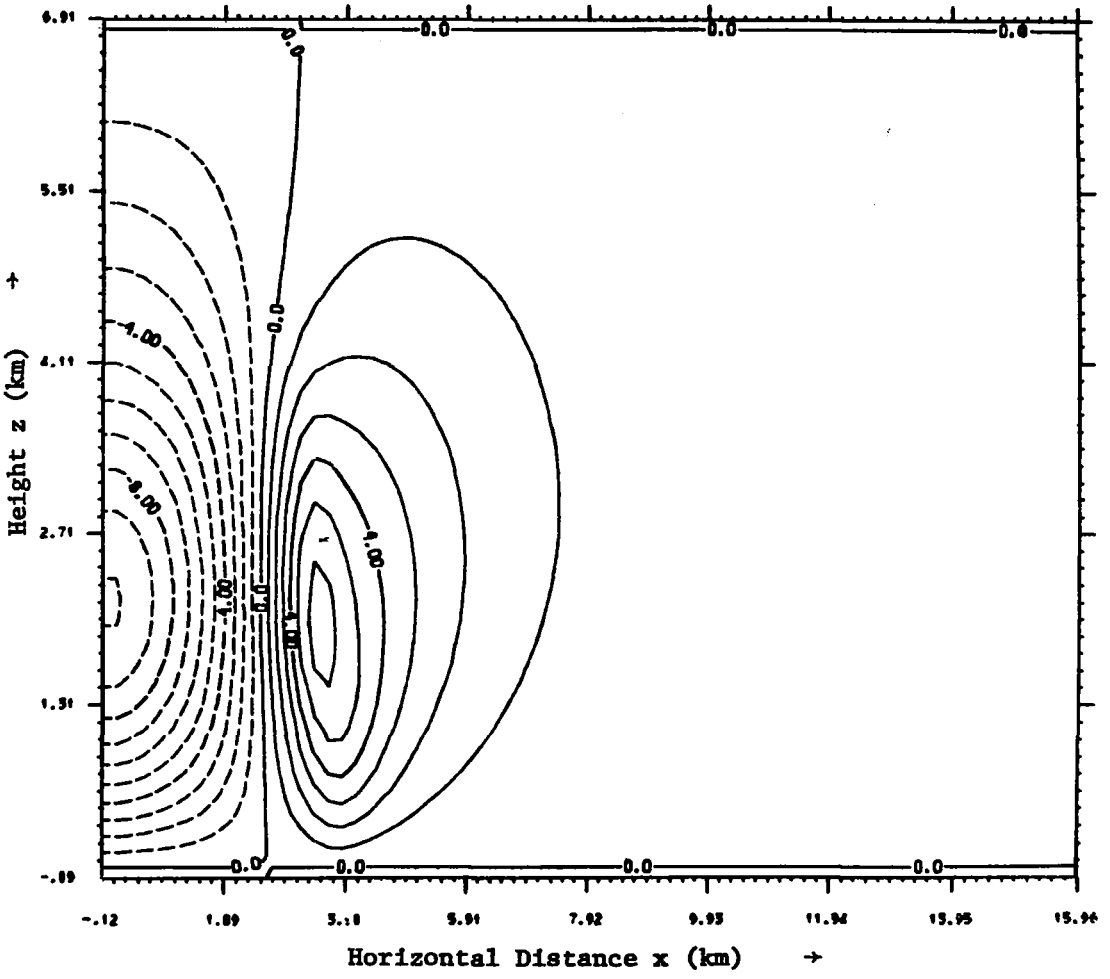

Figure 7. Vertical velocity field (m/sec) at 2.00 minutes. The left boundary represents the central axis of the developing downdraft. Contour interval is 1.0 m/sec and dashed contours (negative valued) indicate downward velocities.

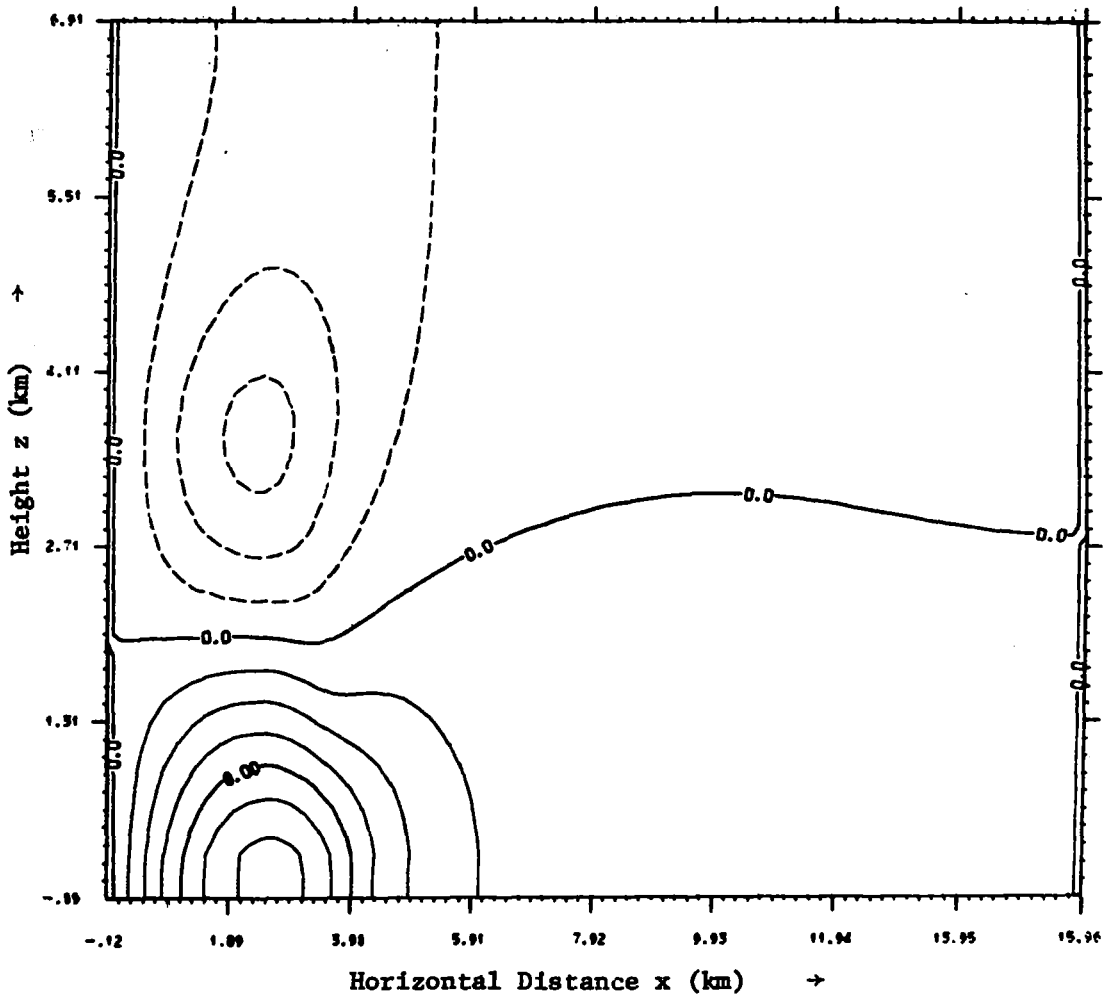

Figure 8. The horizontal wind field (m/sec) at 2.00 minutes. Contour interval is 2.0 m/sec and solid contours (positive valued) indicate wind velocities directed in the positive x-direction.

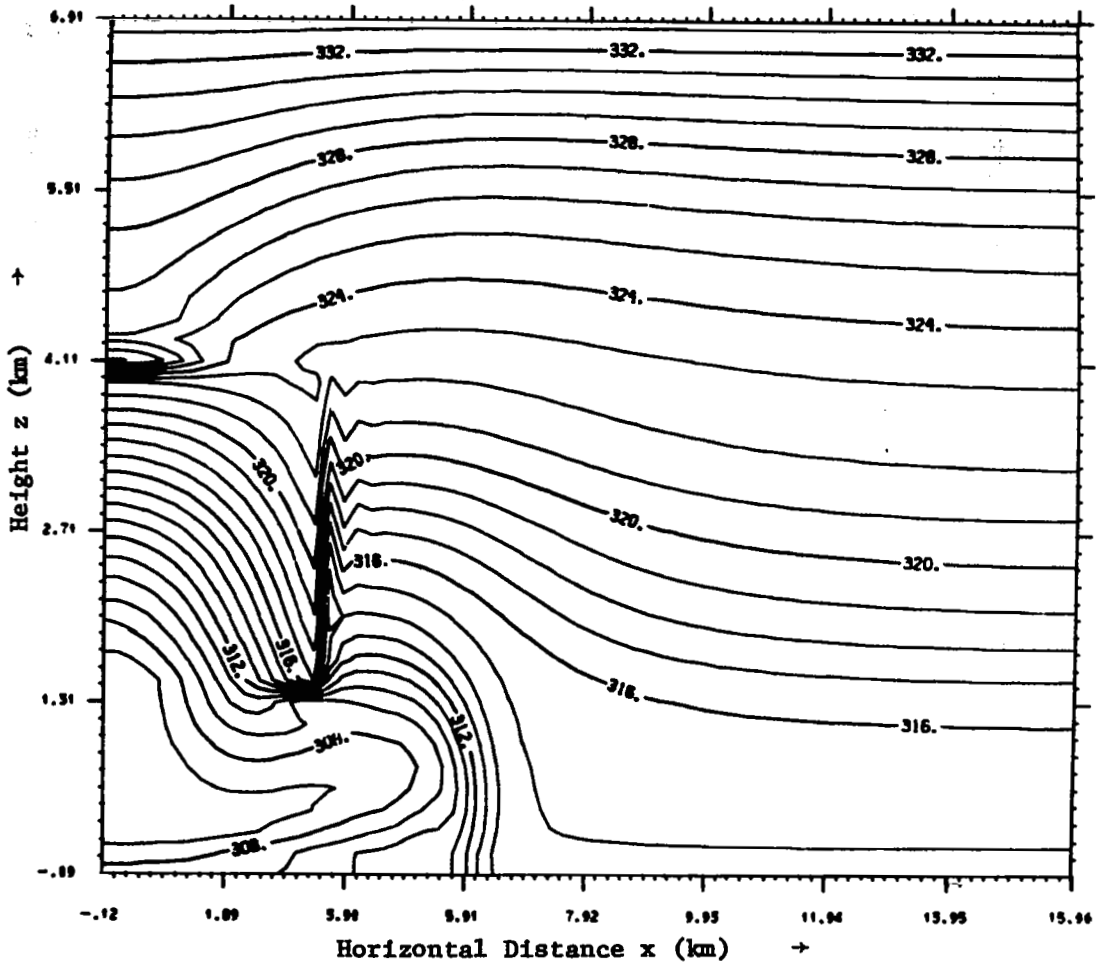

Figure 9. Potential temperature field (K) at 6.00 minutes. The developing cold outflow is evident in the low levels and a strong horizontal temperature gradient has formed at its forward edge at x = 6.0 km. Contour interval is 1.0 K.

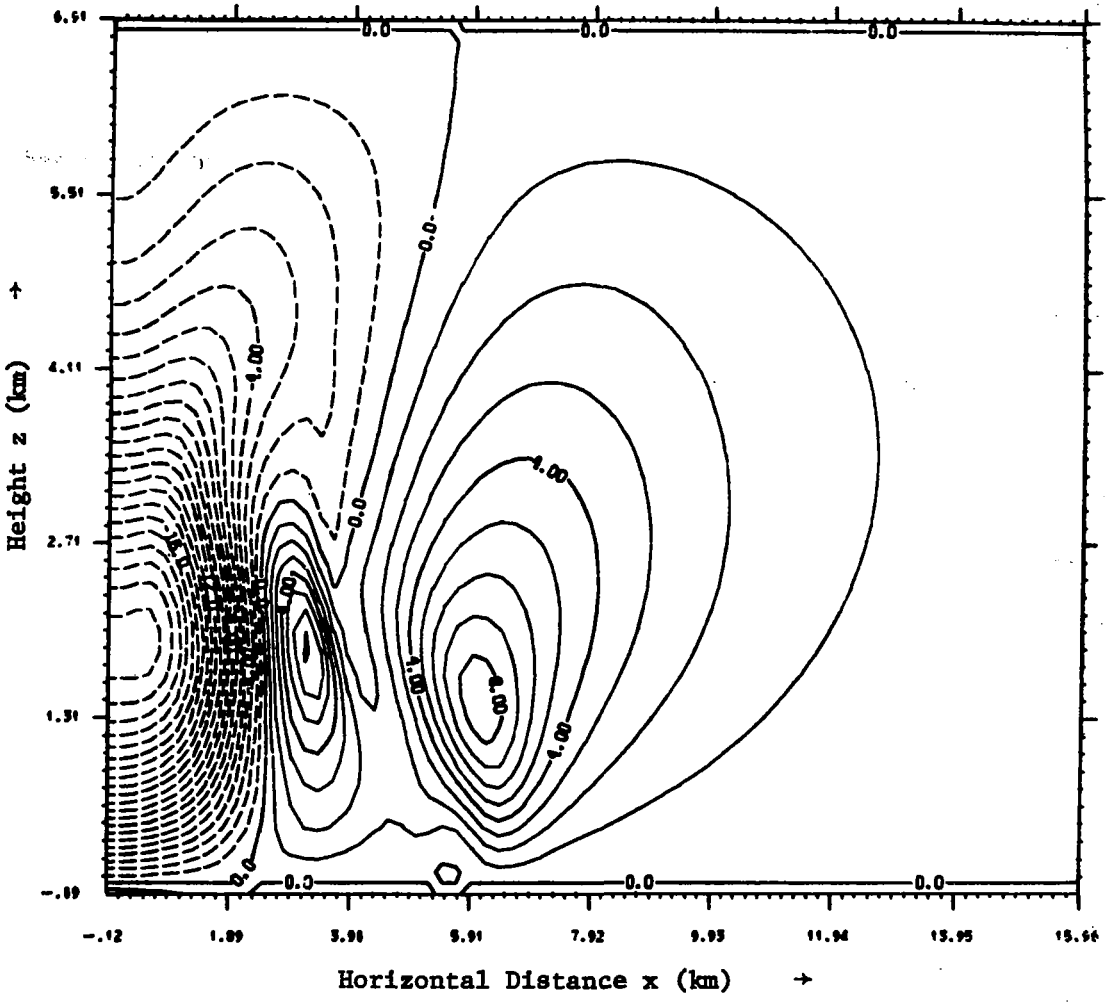

Figure 10. Vertical velocity field (m/sec) at 6.00 minutes showing the vigorous downdraft at the left boundary and the strong upward motion coincident with the forward edge of the cold outflow at x = 6.0 km. Contour interval 1.0 m/sec.

(Figure 10) as it propagates forward and undercuts the less dense ambient air.

In Figure 11, the strong horizontal winds associated with the cold surge have developed a maximum of horizontal speed shear coincident with the sharp temperature front in Figure 9. This is the beginning of the gust front. At this early stage, only one wind speed maximum is evident at the surface.

Figure 12 gives an overview of the developing direct circulation by depicting several air parcel trajectories. The general counterclockwise flow pattern of the air parcels is produced by cold air sinking in the downdraft and warm ambient air rising in the updraft ahead of the front.

3.2 The Quasi-Steady Configuration

By the time the cold surge has propagated about 12 km outward from its downdraft source, it and the associated gust front have achieved a steady configuration. This marks the beginning of the mature stage, since the characteristic circulations, geometric shape and structure, and intensity have now been determined. As long as a steady cold downdraft is sustained, the gust front maintains this configuration and simply propagates further outward from the downdraft.

The geometric shape of the cold surge was evident in Figure 4. The 314 K isotherm represented the density or frontal interface between the cold air and warm ambient air. Figure 13, an enlargement of Figure 4, presents in detail the potential temperature configuration at the front. The frontal interface is nearly vertical at the surface,

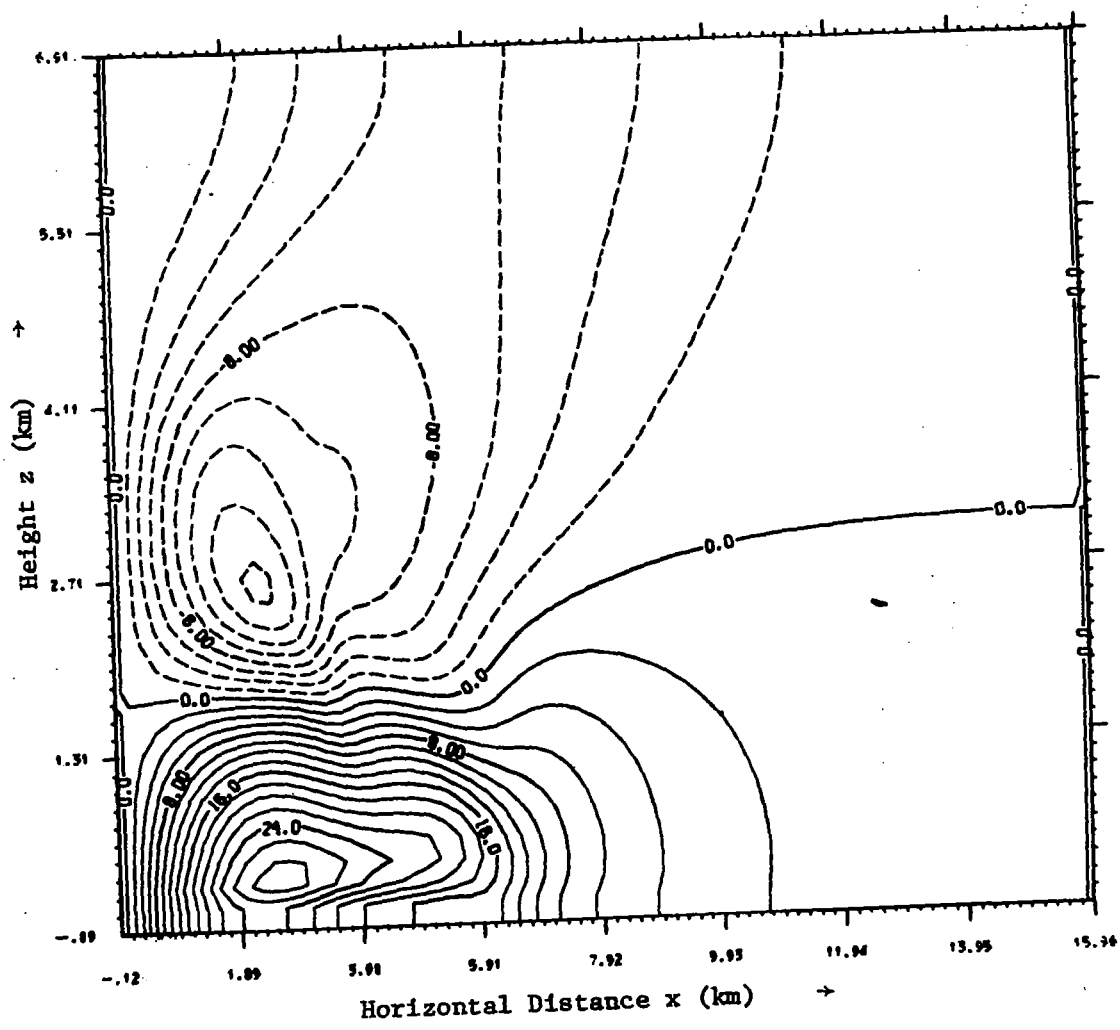

Figure 11. The horizontal wind field (m/sec) at 6.00 minutes. The packing of the isotachs in the low levels at x = 6.0 km represents the developing gust front. Contour interval is 2.0 m/sec.

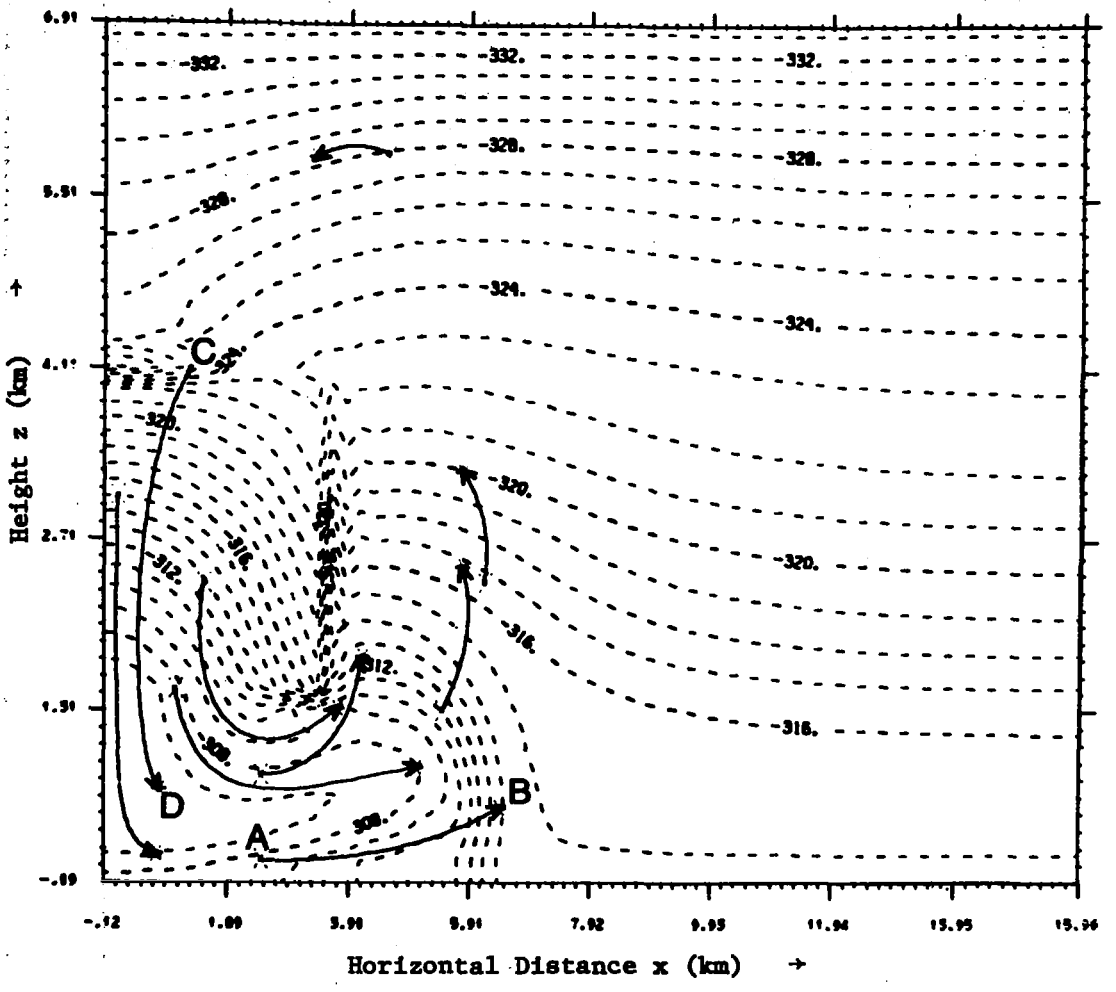

Figure 12. Kinematic trajectories showing the paths traversed by certain air parcels between 0.40 minutes and 6.00 minutes. The dashed contours represent the potential temperature field of Figure 9.

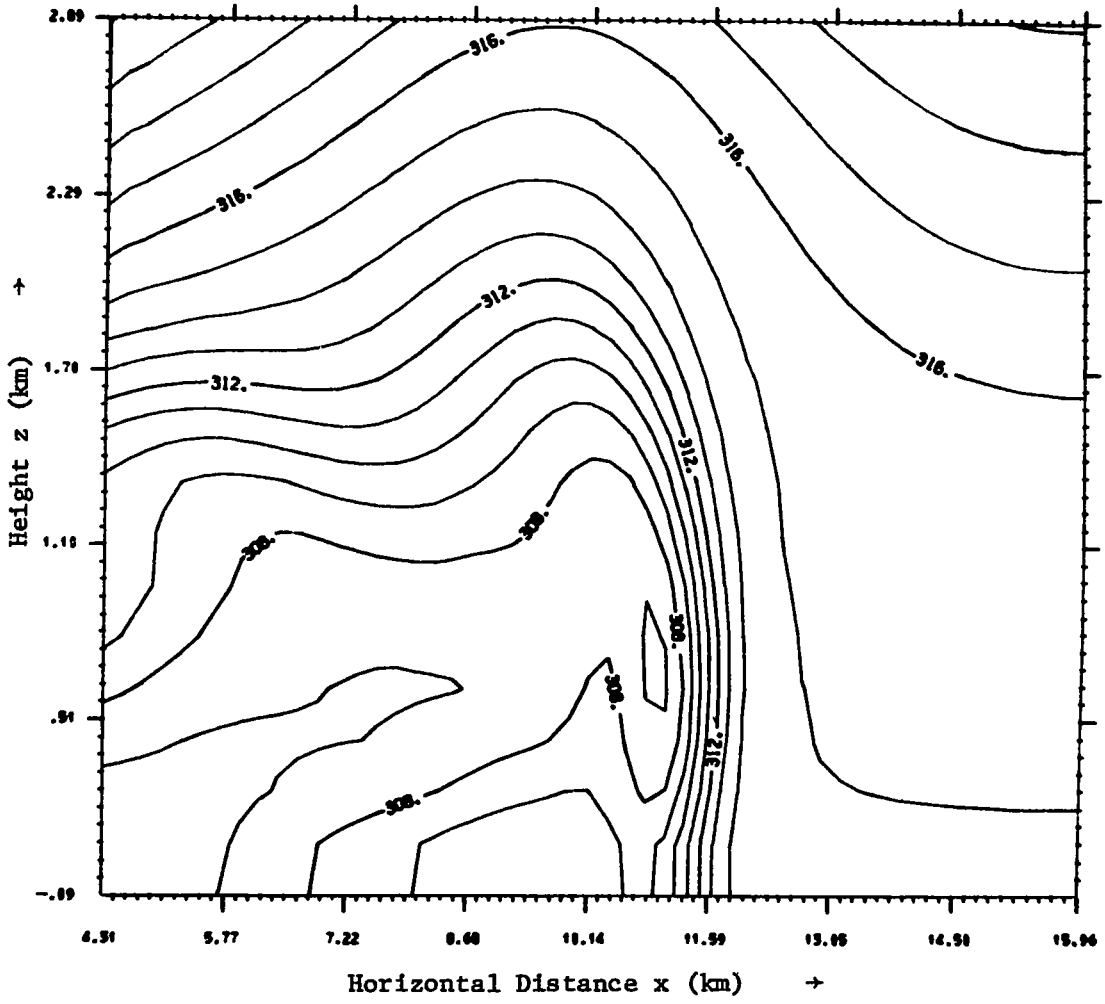

Figure 13. An enlargement of Figure 4 showing the potential temperature field (K) at 12.00 minutes at the front. The 314 K isotherm outlines the elevated head of cold air. The contour interval is 1.0 K.

with a slight forward slope. It then rises to form an elevated head of cold air that is higher than the average depth of cold air upstream. Such a feature was clearly present in all model trials. Similar heads of cold air at the leading edge of cold fronts have been inferred in several observational studies (Berson, 1958, Clarke, 1961, Charba, 1972) and have been observed in laboratory tank studies of density surges (Middleton, 1966, Simpson, 1969).

Figure 14 gives a complete picture of the horizontal wind field in the mature stage. In Figure 15, an enlargement of Figure 14 in the vicinity of the front, the dashed line represents the frontal interface between the cold air and warm ambient air. It is evident in Figure 15 that the cold outflow is led by an intense wind surge, which is slightly retarded at the ground. This intense wind surge shall be referred to now as the gust front.

The gust front is characterized by a rapid increase of wind speed from 6 m/sec to 20 m/sec over a horizontal distance of just 2.0 km. This represents a horizontal wind speed shear of 7.0 m sec^{-1} km^{-1}. Given this shear and the frontal propagation speed of 15 m/sec, the wind velocity at a fixed point will increase from 6.0 m/sec to 20.0 m/sec in 2.3 minutes.

It is obvious that the model cannot resolve actual turbulent wind gusts. Consequently, the maximum wind speeds that develop in the model may be somewhat less than are commonly observed. In relation to this, the wind fields presented in this work must be considered, in some sense, as time averaged winds that represent the general overall wind structure rather than the turbulent features of atmospheric gust fronts.

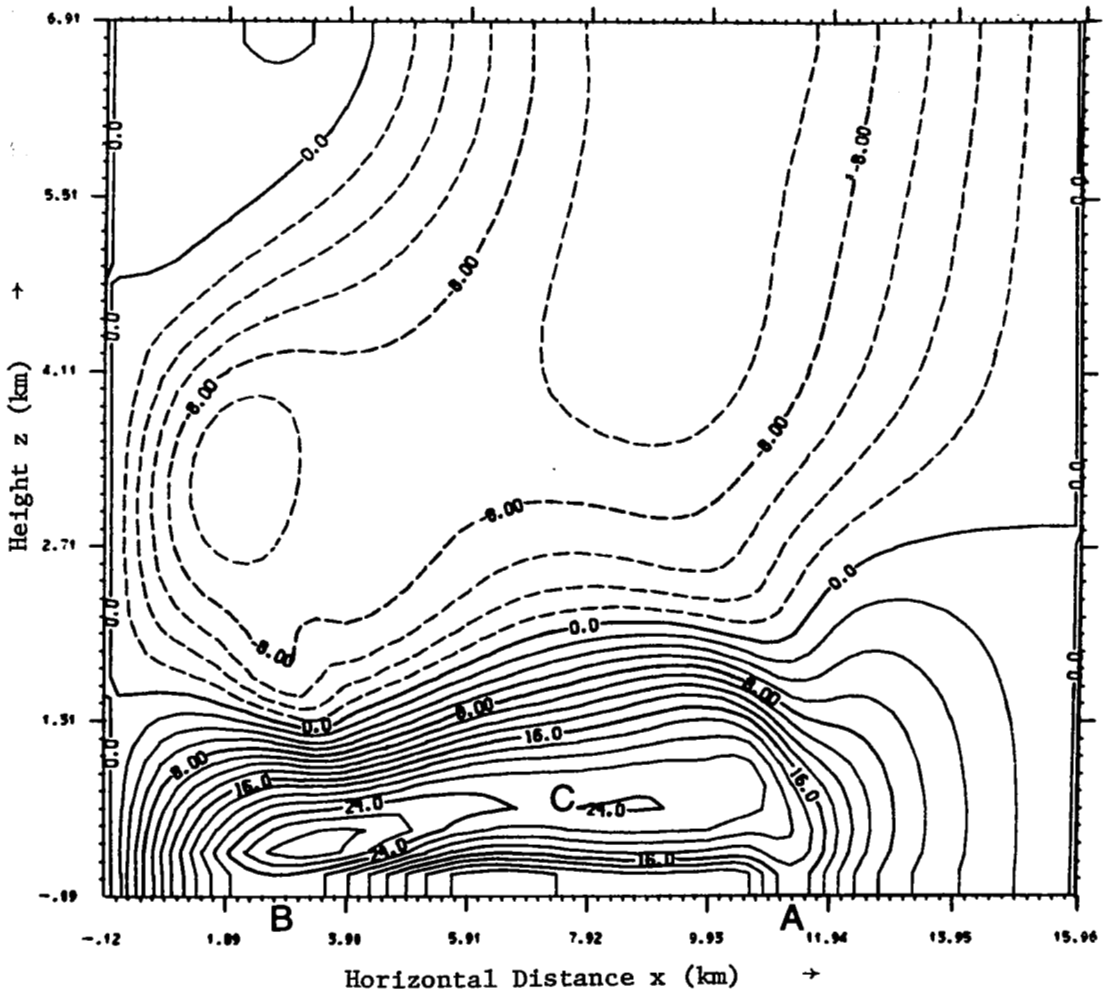

Figure 14. The horizontal wind field (m/sec) at 12.00 minutes during the mature stage. Two surface wind maxima are denoted by A and B, and C denotes the core of maximum winds above the surface. The contour interval is 2.0 m/sec.

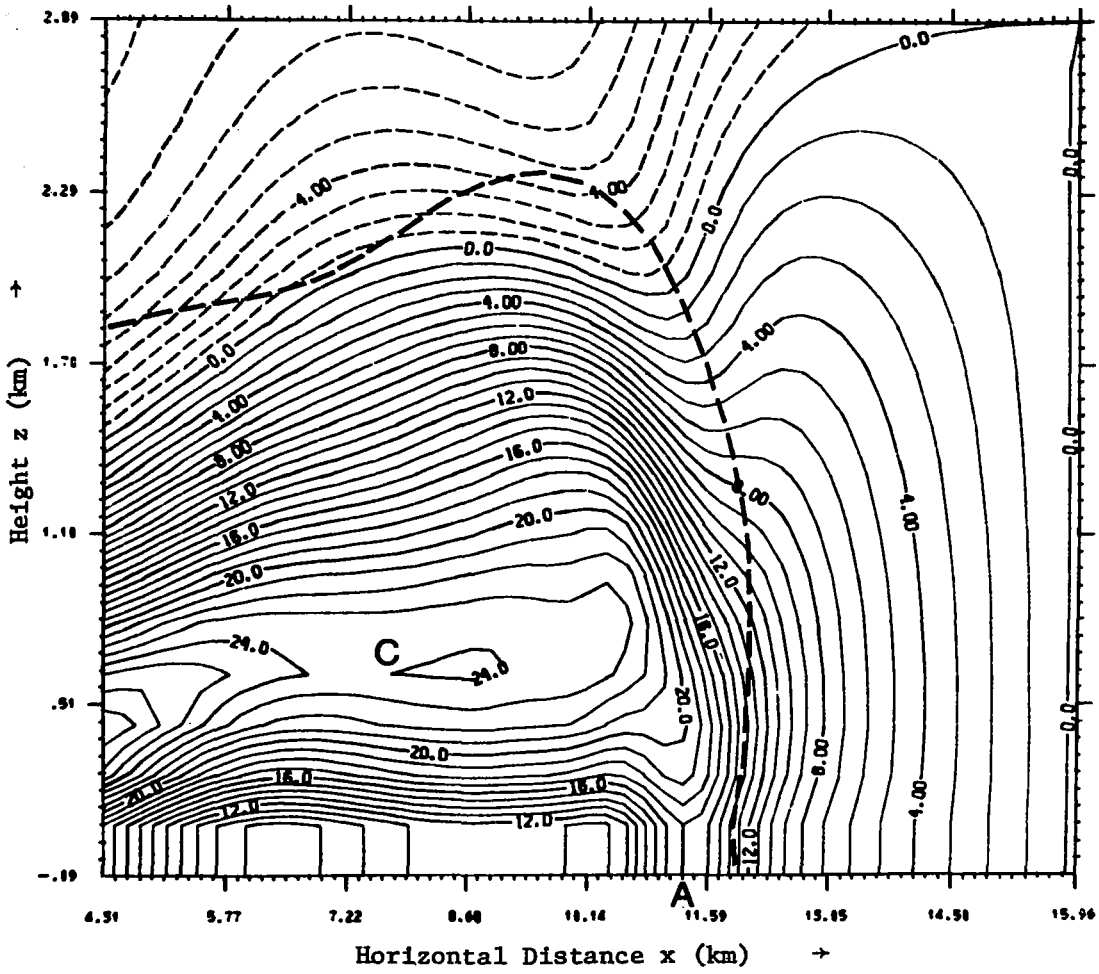

Figure 15. An enlargement of Figure 14 showing the horizontal wind field (m/sec) at 12.00 minutes at the front. The contour interval is 1.0 m/sec. The dashed line (314 K isotherm of Figure 13) represents the density or frontal interface of the cold outflow.

In Figure 14, two distinct surface wind maxima are apparent, one immediately behind the front (labeled A) and one further upstream near the downdraft (labeled B). Similar double wind maxima have been observed during the passage of severe squall line systems (Charba, 1972). The model suggests an explanation. Quite typically the forward edge of a thunderstorm cold surge lies within several miles of the main rain area when the convective cell is in the initial part of its mature stage. During this period, the strong surface winds may show a continuous gradient increasing towards a single wind maximum near the downdraft (as in Figure 11).

However, in the late mature and dissipation stages of the thunderstorm, the gust front may lie ahead of the parent cell by as much as 20 km (Colmer, 1971). Then, two surface wind maxima may develop as in Figure 14, one associated with the gust front and one further upstream associated with the downdraft.

Referring again to Figure 15, we may examine the structure of the cold surge winds above the surface. At the front and below 1.0 km, there is only a slight vertical shear of the horizontal speed since the isotachs are nearly vertical. This correlates closely with the nearly vertical slope of the frontal interface.

However, upstream of the front, large vertical shears of wind speed on the order of 15 m sec^{-1} km^{-1} are evident between the surface and the 550 m level. At this level, a distinct "core" of maximum winds (labeled C) extends nearly the entire length of the cold surge. This core of maximum winds represents the strongest outward current of cold air. It was a distinct feature in all model experiments and its magnitude in all cases was greater than the surface wind maximum (A).

It is worth pointing out that in each model experiment, the level of this maximum wind core varied somewhat, but it always occurred at an altitude higher than the tallest wind towers now in operation. This result, of course, was dependent on the surface drag parameterization and vertical resolution within the model. Nevertheless, it may be reasonable to expect that the wind maxima recorded by wind towers during gust front occurrences are exceeded by stronger winds further aloft. This was also suggested by Sinclair (1973) in his gust front study using tower observations.

While the speeds in the strong wind core (C) average more than 20 m/sec with maximum values of 24 m/sec, the front only propagates forward at a rate of 15 m/sec. Thus, behind the frontal interface, the horizontal speed of the winds in the wind core is much greater than the rate of advance of the front. This suggests that as the strong forward current of cold air approaches the frontal interface, it might develop a larger vertical speed component at the expense of the horizontal component. This does indeed occur, as will be shown below.

Figure 16 illustrates the streamline pattern of the flow within the cold surge and in the ambient environment. The dotted line represents the density interface. The strong downdraft evident at the left boundary is deflected by the solid lower boundary and is transformed into the strong horizontal current of cold air comprising the cold surge. However, the horizontal orientation of the streamlines within the cold surge ends abruptly just behind the density interface where the flow curves sharply upward. Thus, the horizontal component of the cold current does change abruptly near the front.

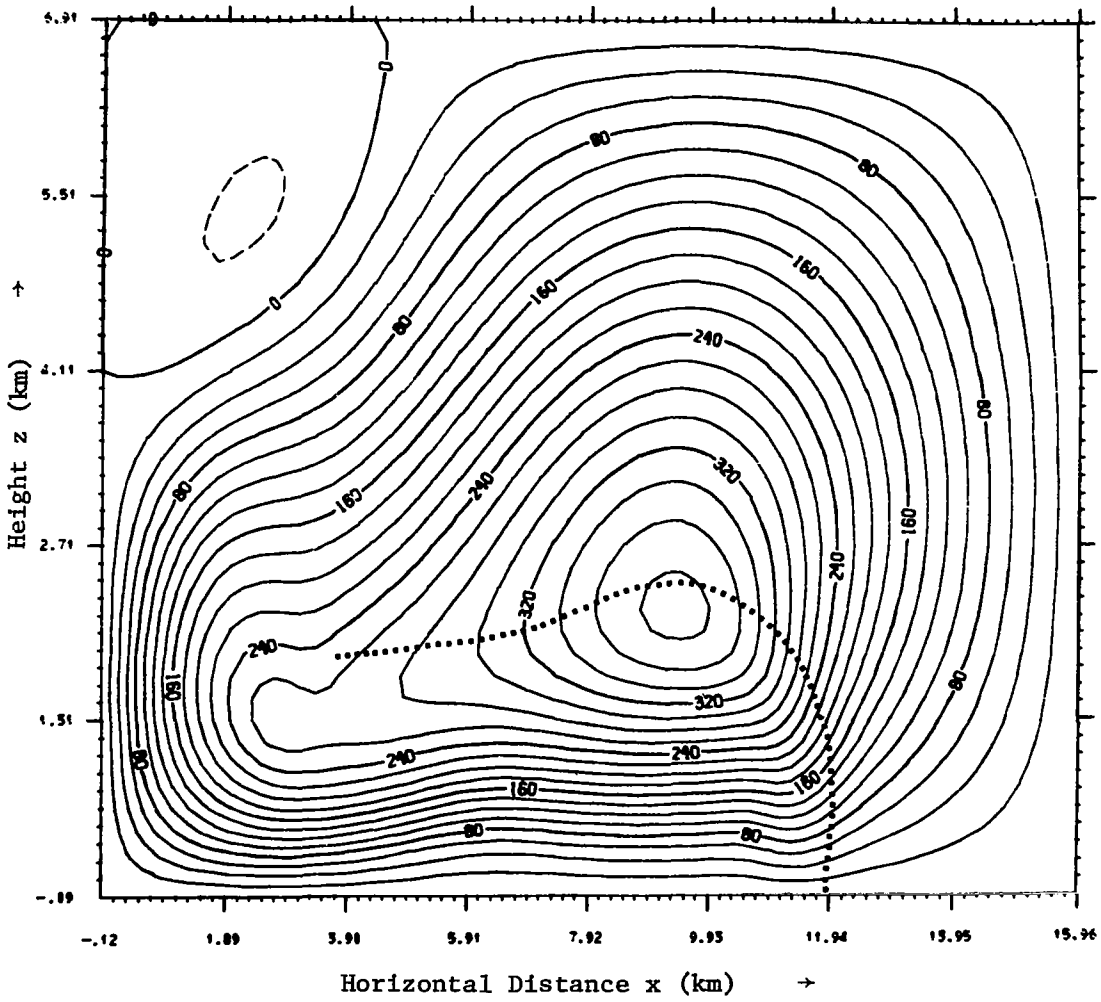

Figure 16. The streamline flow pattern at 12.00 minutes during the mature stage. The solid streamlines depict counter-clockwise flow and the dotted line represents the frontal interface. Contour interval is 2.0 x 10^7 cm^2/sec and labels are scaled by 1.0 x 10^{-6}.

From the streamline pattern (Figure 16), it appears that cold air may in fact be crossing the frontal boundary. But streamlines are a reasonable representation of actual air parcel trajectories only if the streamline pattern is invariant in time. In all model trials, since the front propagation speed is large and the character of the flow pattern changes significantly at the front, streamlines poorly represent the trajectories of air parcels that are near the frontal boundary.

Figure 17 depicts several kinematic trajectories traversed during the first 10 minutes by several air parcels within the cold surge. Note especially the parcel trajectory labeled A-B that has been deflected sharply upward. Earlier at 6 minutes (Figure 12), this parcel has just approached the frontal interface. However, even though it travels faster than the front between 6 and 10 minutes, this parcel has <u>not</u> crossed the frontal boundary (Figure 17), but rather it has curved sharply upward to form (along with many other parcels following similar paths) the upward bulge of cold air referred to previously as the elevated head. Actual trajectories, then, further verify the upward deflection of the strong forward current of cold air as it approaches the front.

At 10 minutes, parcel A-B has reached its highest point within the elevated head crest. Subsequently, at 12 minutes (Figure 5), this parcel has started downward after traversing a small eddy-like loop in the wake of the head crest. Other model experiments (Figure 18) show trajectories with even more pronounced eddy-like loops in the wake region of the head crest, suggesting that the flow in this region is characterized by turbulent mixing and entrainment of warm ambient

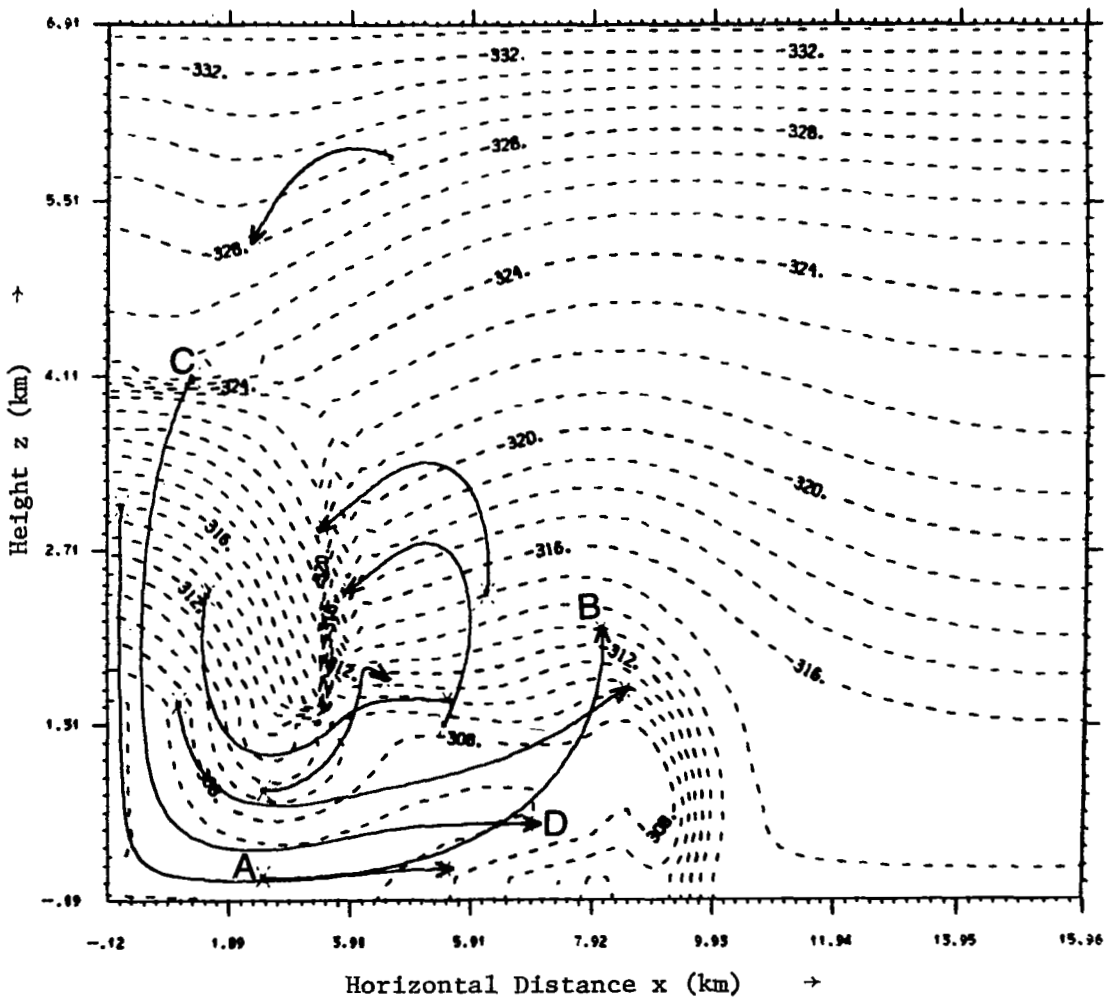

Figure 17. Kinematic trajectories showing the paths traversed by certain air parcels between 0.40 minutes and 10.00 minutes. Trajectory A-B illustrates the upward deflection of cold air into the elevated head. The dashed contours represent the potential temperature field at 10.00 minutes.

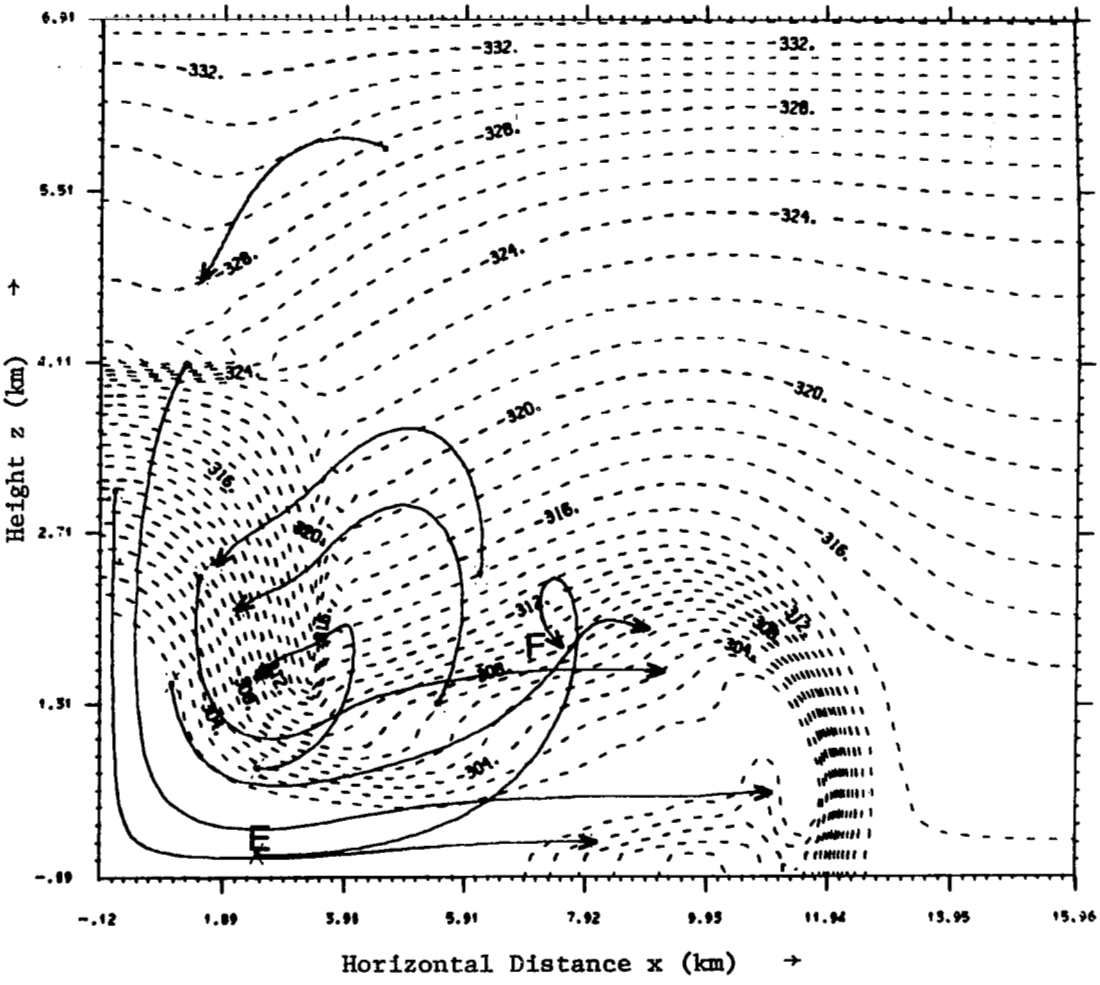

Figure 18. A different model experiment that more clearly shows, by trajectory E-F, the eddy-like looping of air parcel trajectories in the wake of the elevated head crest. The dashed contours represent the potential temperature field at 10.00 minutes for a case presented later in Section 4.1.

air from aloft. A region of turbulent mixing has in fact been observed in the immediate wake regions of the heads of density surges in laboratory tank experiments (Keulegan, 1958, and Simpson, 1969).

The unique vertical motions generally associated with the elevated head are further illustrated in Figures 19 and 20. In Figure 20, a sharp division between upward motion and downward motion within the head crest is readily apparent. Furthermore, a narrow but distinct region of strong upward velocities is observed immediately behind the frontal interface (Figure 20). These features correlate strongly with the eddy-like looping of trajectories within the head crest and the sharp upward deflection of trajectories at the front.

Ahead of the front, the sudden horizontal wind surge is inducing strong low level convergence and rapid upward displacement of the ambient air. Upward velocities as large as 10 m/sec (Figure 20) are attained in the ambient air being lifted over the elevated head. These values may be somewhat large due to the proximity of the right boundary; however, they are still representative because observational studies of gust fronts have inferred upward velocities as large as 5 m/sec ahead of the cold surge (Charba, 1972).

In the upper part of Figure 19, a large region of upward velocities is compensated by a large region of downward velocities -- the dividing line bisecting the crest of the elevated head (Figure 20). It is evident, then, that the cold surge has induced a large circulation (Figure 16) that may easily be viewed as one mechanism for maintaining a severe thunderstorm, or the mechanism responsible for the generation of a new one.

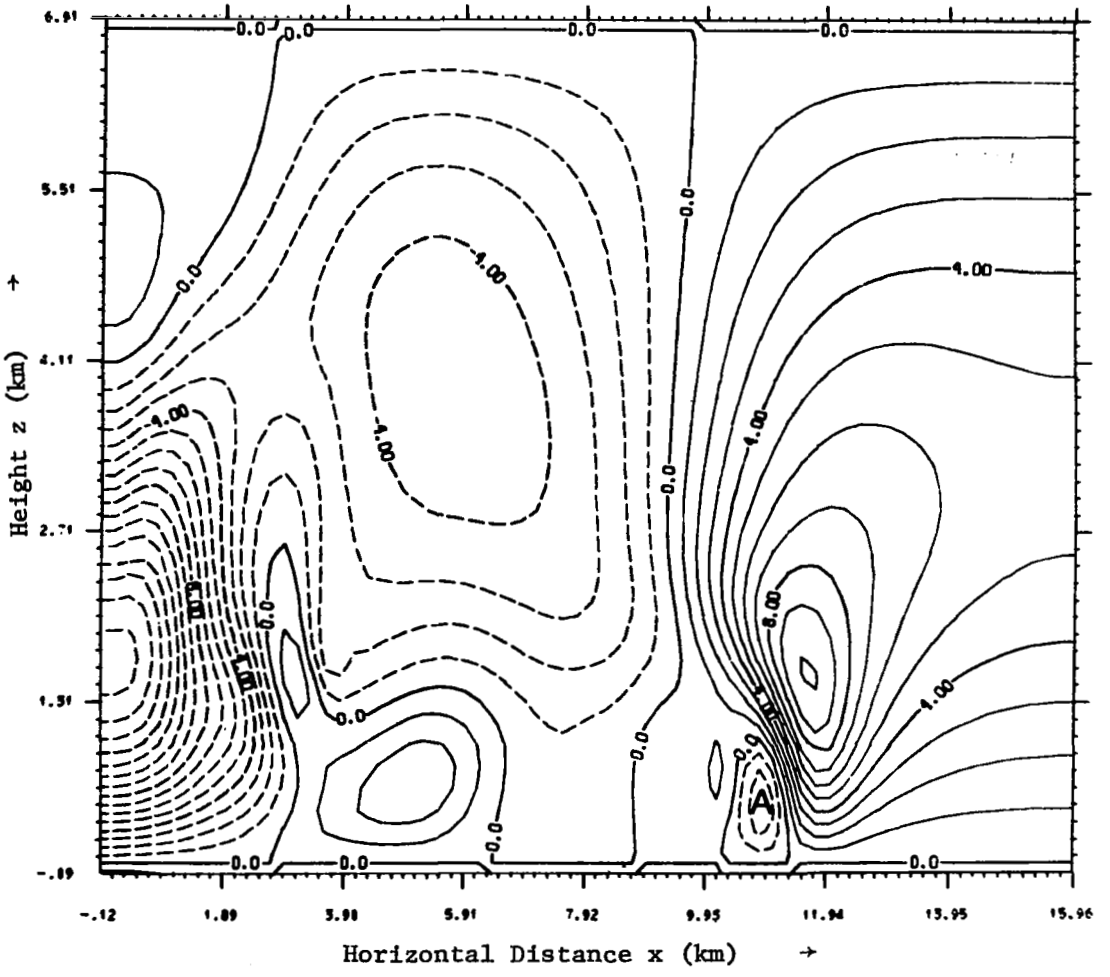

Figure 19. Vertical velocity field (m/sec) at 12.00 minutes during the mature stage. The relative maximum of downward motion just behind the front is labeled A. The maximum downdraft velocity is 15 m/sec. Contour interval is 1.0 m/sec.

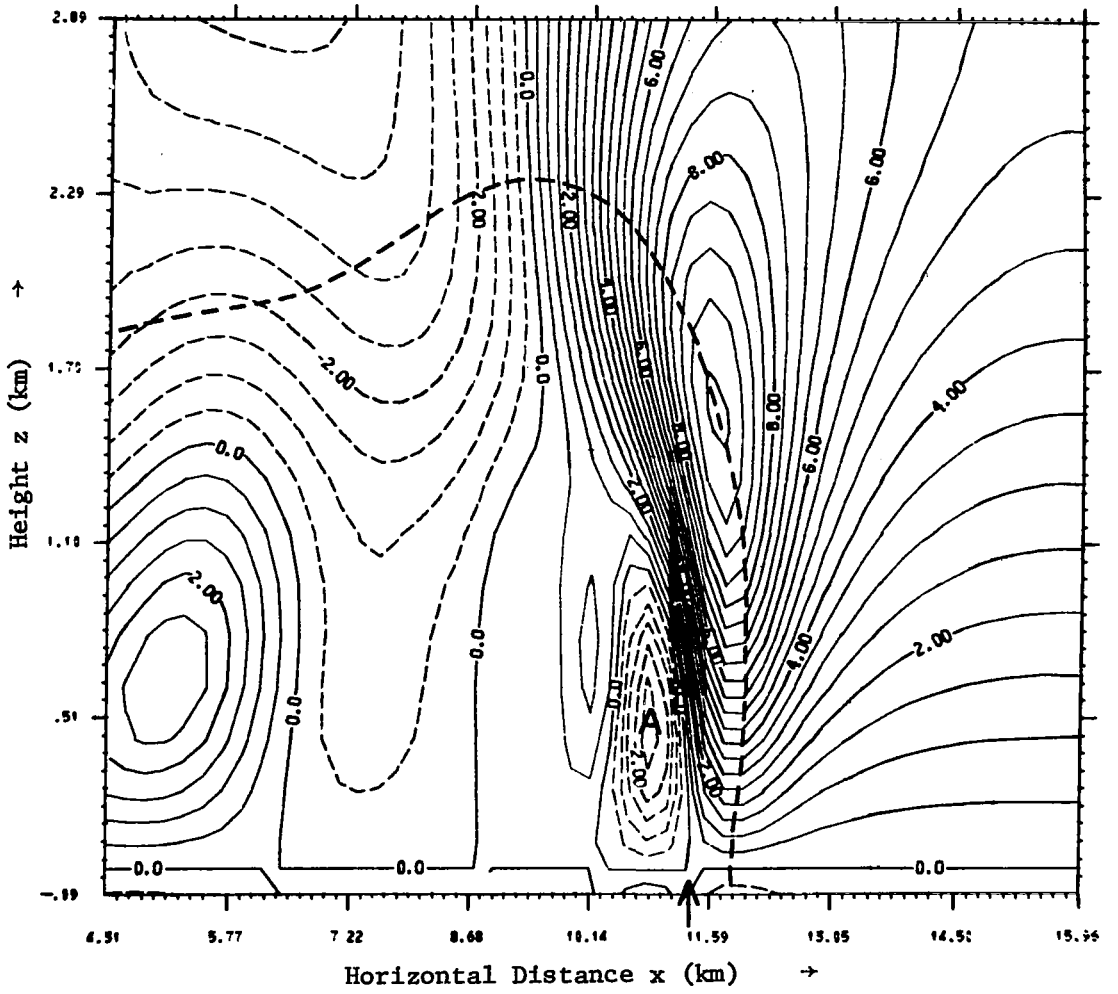

Figure 20. An enlargement of Figure 19 showing the vertical velocity field (m/sec) at 12.00 minutes at the front. The arrow denotes the position of the surface wind maximum in Figure 15 and the dashed line represents the frontal interface. Contour interval is 0.50 m/sec.

About 1.0 km behind the frontal interface near the surface, a relative maximum of downward motion is observed (labeled A in Figures 19 and 20). A comparison with Figure 13 reveals that this downward motion is coincident with the coldest, densest air behind the front and also with the surface wind speed maximum (A in Figure 15). In the next chapter it will be shown that this feature is a factor that helps to maintain the surface wind speed maximum against surface drag. Upstream within the cold outflow, a general region of subsidence is followed even further upstream by a region of upward motion (Figure 19) that results from a slight "rebounding" off the bottom surface of the downrush of air in the vigorous downdraft.

The features of the mature gust front presented in this section were observed in virtually all model experiments. In subsequent sections, this particular model trial we have been discussing shall be called the reference case. The structure that has been described is representative of the quasi-steady configuration that the model gust front achieves after propagating about 10 km from the downdraft. As long as a steady downdraft source is maintained, this general configuration is preserved as the gust front continues to advance, with only some decrease in peak wind values and front propagation speed.

It is recognized that the figures that have been presented here depict the gust front for only the first 12 minutes of development. However, model trials that were integrated on larger domains, where Δx was increased from 230 m to 450 m, allowed the gust front to evolve for 30 minutes and propagate 24 km from its source. During these longer trials, a front structure such as that described here also developed by the time the front was 10 km from its source, and persisted

throughout the remainder of the integration. However, the results from model trials integrated on the smaller domain have been presented in order to take advantage of the detail enhancement afforded by the finer resolution.

4.0 DEPENDENCE OF GUST FRONT STRUCTURE ON CERTAIN MODEL PARAMETERS

Numerous parameters in the model can be varied in order to test their influence on the development of the gust front, but the scope of experiments is necessarily limited. In this work, three parameters are chosen for further investigation: 1) the magnitude of the downdraft temperature depression, 2) surface drag, and 3) the initial ambient stability. This final choice is motivated by an intuitive physical conception of the gust front gained through reference to previous studies.

4.1 Magnitude of the Downdraft Temperature Depression

Surface observations taken during thunderstorm gust fronts have measured temperature decreases across the front ranging from 3 K to 13 K (Idso, 1972). The magnitude of these temperature falls is very strongly correlated to the intensity of the gust fronts. In general, much stronger surface winds and larger amplitude pressure jumps are recorded simultaneously with the larger temperature decreases. The thermal contrast at the front, in turn, is dependent on the efficiency of evaporative cooling in the downdraft; therefore, some relationship between downdraft temperature depression and maximum surface wind might be expected.

Fawbush and Miller (1954) applied this idea by developing the "downrush temperature technique" for forecasting peak surface wind gusts occurring during thunderstorms. In this technique, the coldest downdraft temperature is estimated and then used in an empirical

relationship to calculate a peak surface wind. However, this and similar empirical techniques have not been too successful. Nevertheless, the observations that motivated them suggest using the downdraft parameterization in the present model to produce downdrafts with different temperature depressions. Then, the effects on the intensity and structure of the resulting gust fronts can be checked.

In this section, we examine results from three model trials in which temperature differences of 3 K, 9 K, and 12 K developed across the front during the mature stage. The model trial presented in Chapter 3.0 serves as the reference case in which a 6 K temperature difference develops. In each case, the temperature difference across the front is about 4 K less than the maximum temperature depression in the downdraft. Other than the differences in downdraft temperature, all four cases were integrated with identical model parameters, including a surface drag coefficient of $C_D = 0.02$ and a vertical temperature profile as shown in Figure 2. To check the following results, we shall frequently compare the 12 K case, which is shown in Figures 21 through 24, with the 6 K reference case.

By producing colder, more dense air in the initialization (Figures 3 and 21), larger downdraft velocities are induced (Figures 19 and 24). The upper diagram of Figure 25 shows that the maximum downdraft velocity during the mature stage increases by 6 m/sec over the range of experiments. These larger velocities, which are coupled with more dense air, result in a large increase in the mass transport through the downdraft, as shown in the lower diagram of Figure 25. Qualitatively then, we are examining in this section the characteristics of gust fronts that are associated with more intense thunderstorms that subject greater volumes of air to greater degrees of cooling.

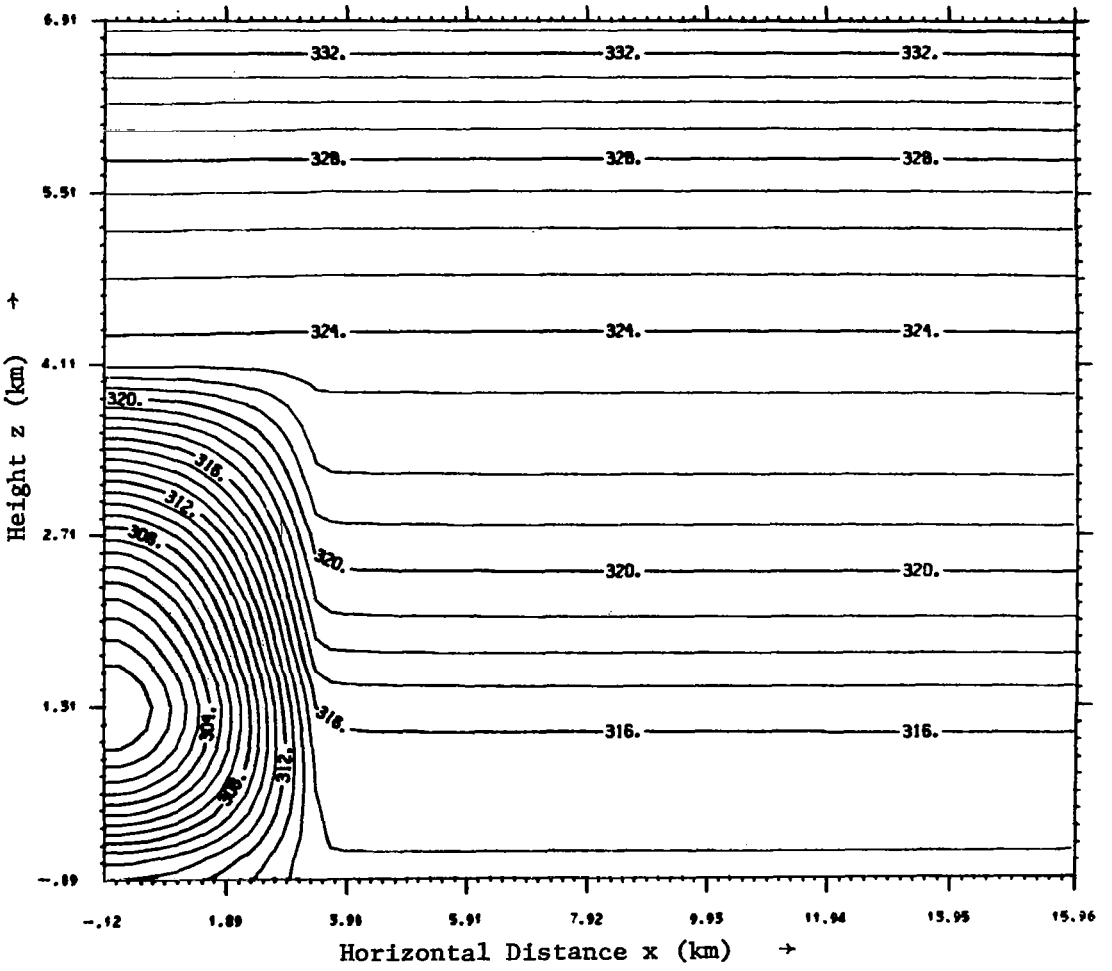

Figure 21. The potential temperature field (K) at 0.67 minutes showing the increased local cooling in the initialization that results in a 12 K temperature decrease across the front. The maximum downdraft temperature depression is 16 K.

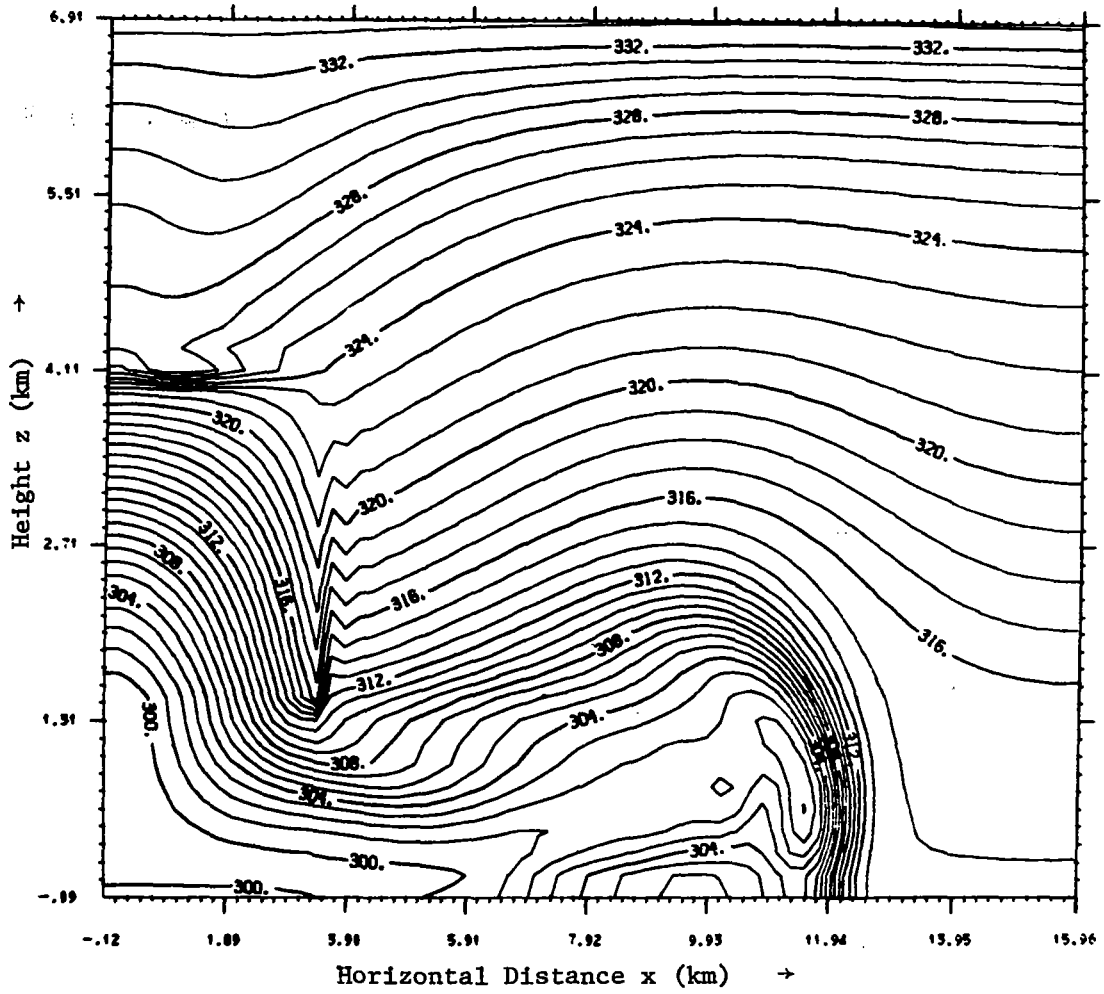

Figure 22. The potential temperature field (K) at 10.00 minutes showing the cold outflow that develops from the initial field in Figure 21. A 12 K temperature difference is apparent at a height of 700 m between the 314 K and the 302 K isotherms at the front. The contour interval is 1.0 K.

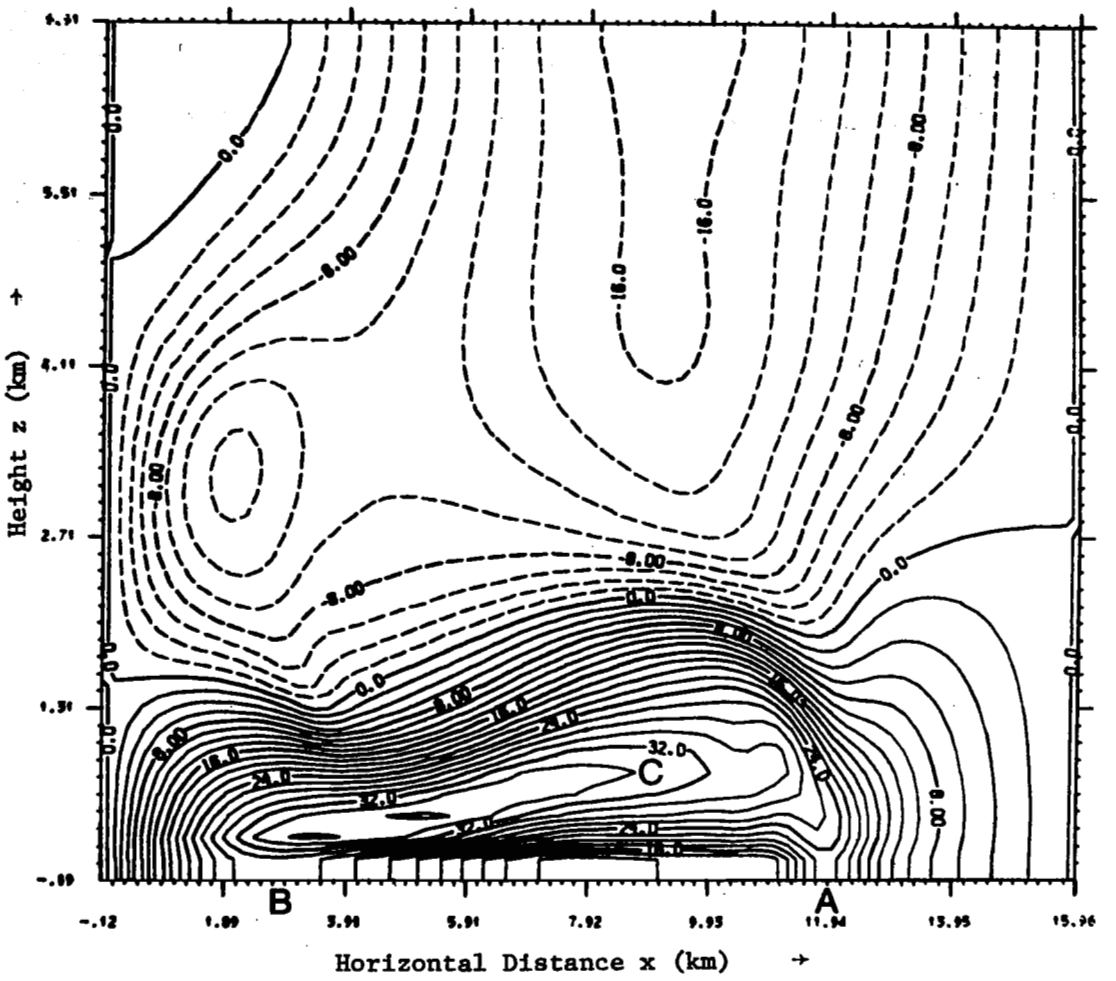

Figure 23. The horizontal wind field (m/sec) at 10.00 minutes for the 12 K case. Two surface wind maxima (labeled A and B) are again observed. A strong vertical wind shear is also evident below the core of maximum winds labeled C. Contour interval is 2.0 m/sec.

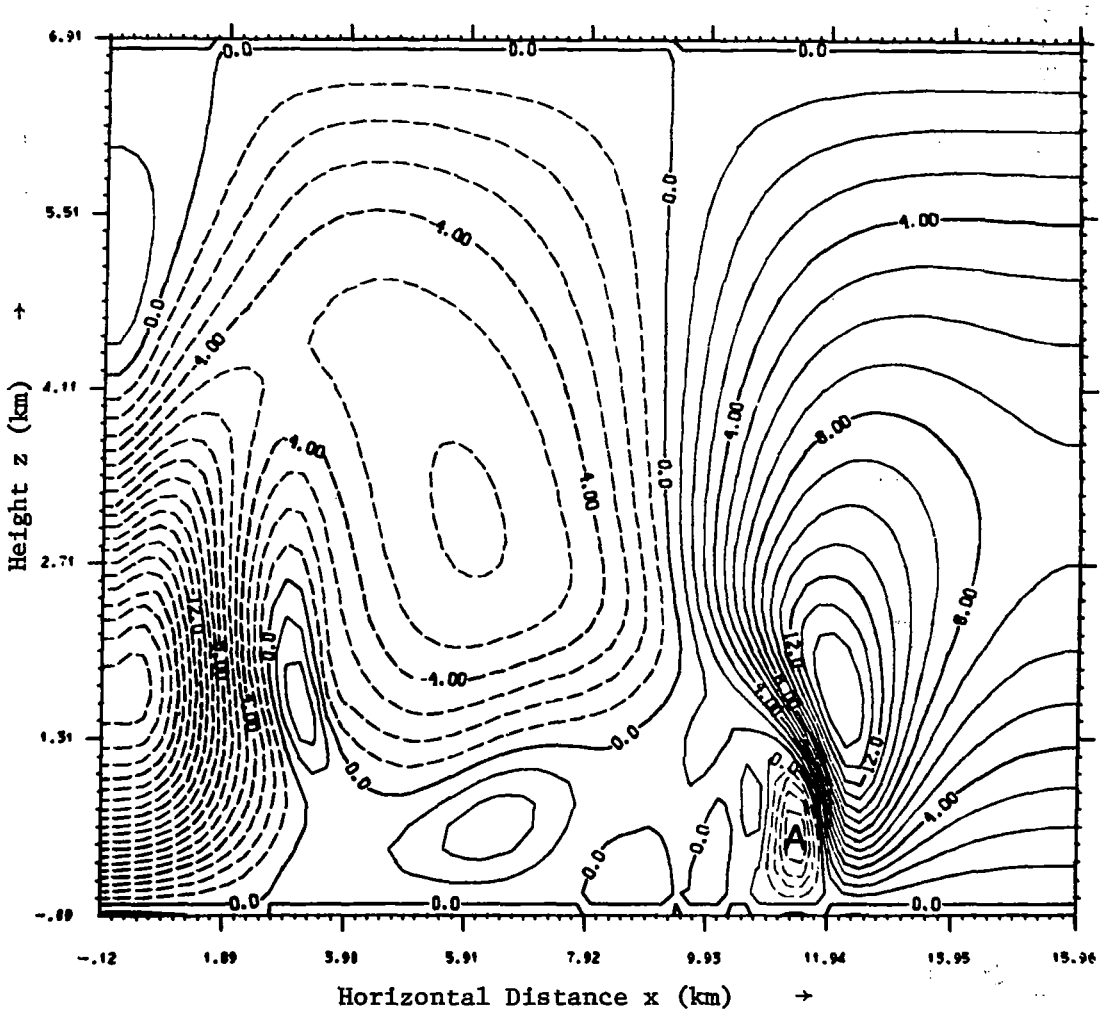

Figure 24. The vertical velocity field (m/sec) at 10.00 minutes for the 12 K case. The relative maximum of downward motion behind the front is labeled A. The maximum downdraft velocity is 19 m/sec. Contour interval is 1.0 m/sec.

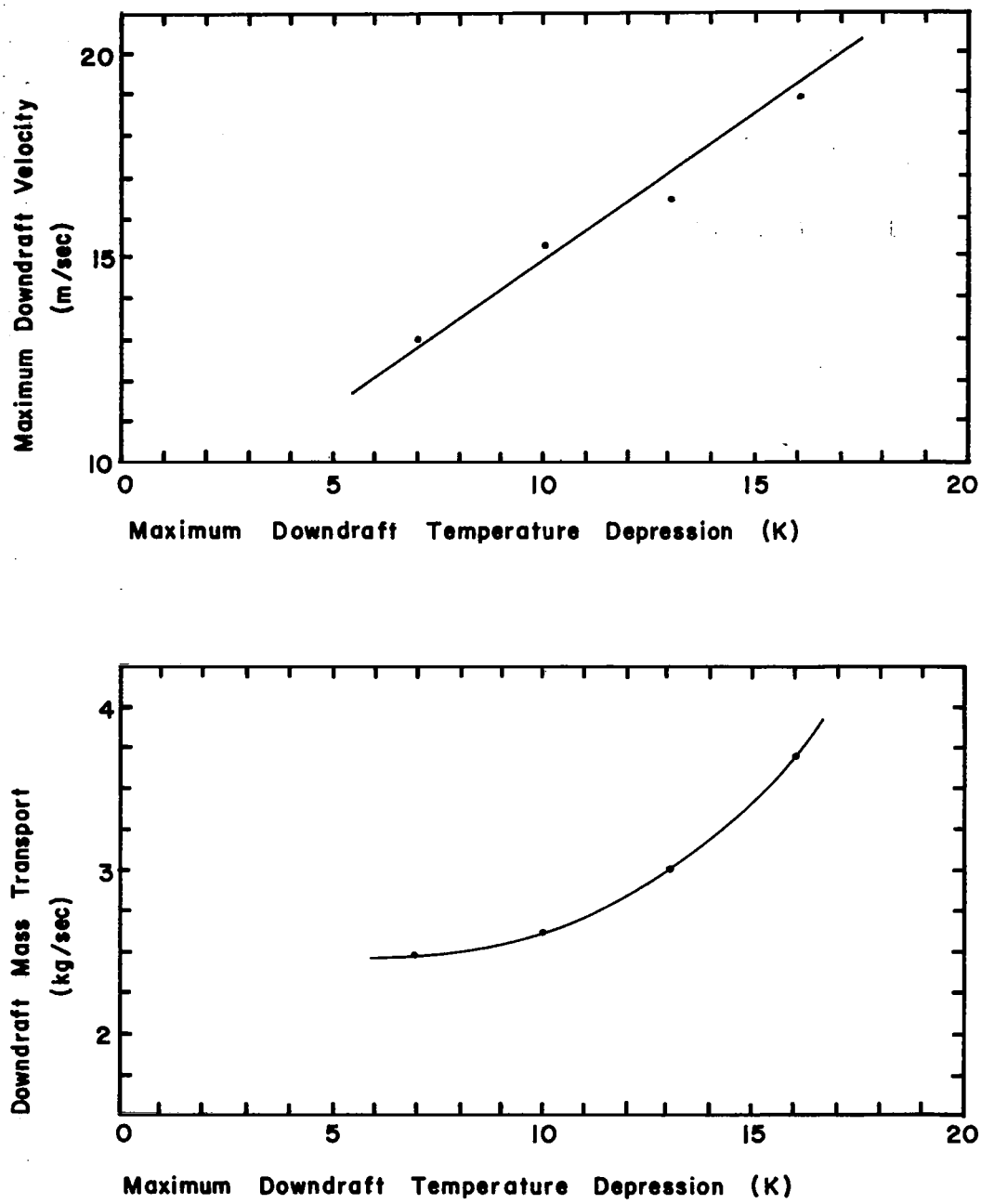

Figure 25. Maximum downdraft velocity is greater (upper diagram) and the transport of mass through the downdraft is greater (lower diagram) in those cases with larger downdraft temperature depressions. The point values in the graphs were determined when the front in each of the four cases had propagated outward 12 km.

From continuity considerations, a larger flux of cold air through the downdraft requires a larger flux of cold air away from the downdraft region at the surface. The two diagrams in Figure 26 show that this is accomplished by an increase in the depth of the resulting cold surge (Figures 4 and 22) and by an increase in the maximum horizontal winds within the cold surge (labeled C in Figures 14 and 23). The maximum cold outflow depth increases from 2.0 to 2.8 km and the maximum wind velocity in the strong wind core nearly doubles from 18 m/sec to 32 m/sec for the 4 K and 12 K cases respectively.

In Figure 27, the variation of the surface wind speed with time is examined in each of the four cases as the gust front approaches and then passes a fixed point. In general, the passage of the gust front is characterized by a distinct wind velocity jump as the wind speeds increase rapidly to a peak value and then decrease rapidly behind the front. The peak in each velocity profile corresponds to the surface wind maximum, such as the one labeled A in Figure 23.

It is evident in Figure 27 that the gust front is significantly more intense in the colder trials for two reasons: 1) the peak wind values are greater and 2) the winds increase to this peak value over a shorter time interval. In accordance with observations then, the model indicates that gust fronts accompanied by larger temperature decreases should tend to exhibit stronger wind surges.

The shorter time interval mentioned in reason (2) above is directly related to the faster front speeds that are exhibited in the colder trials. During the mature stage, the frontal interface propagated at a mean speed of 12.1 m/sec, 15.7 m/sec, 17.8 m/sec, and 20.1 m/sec in

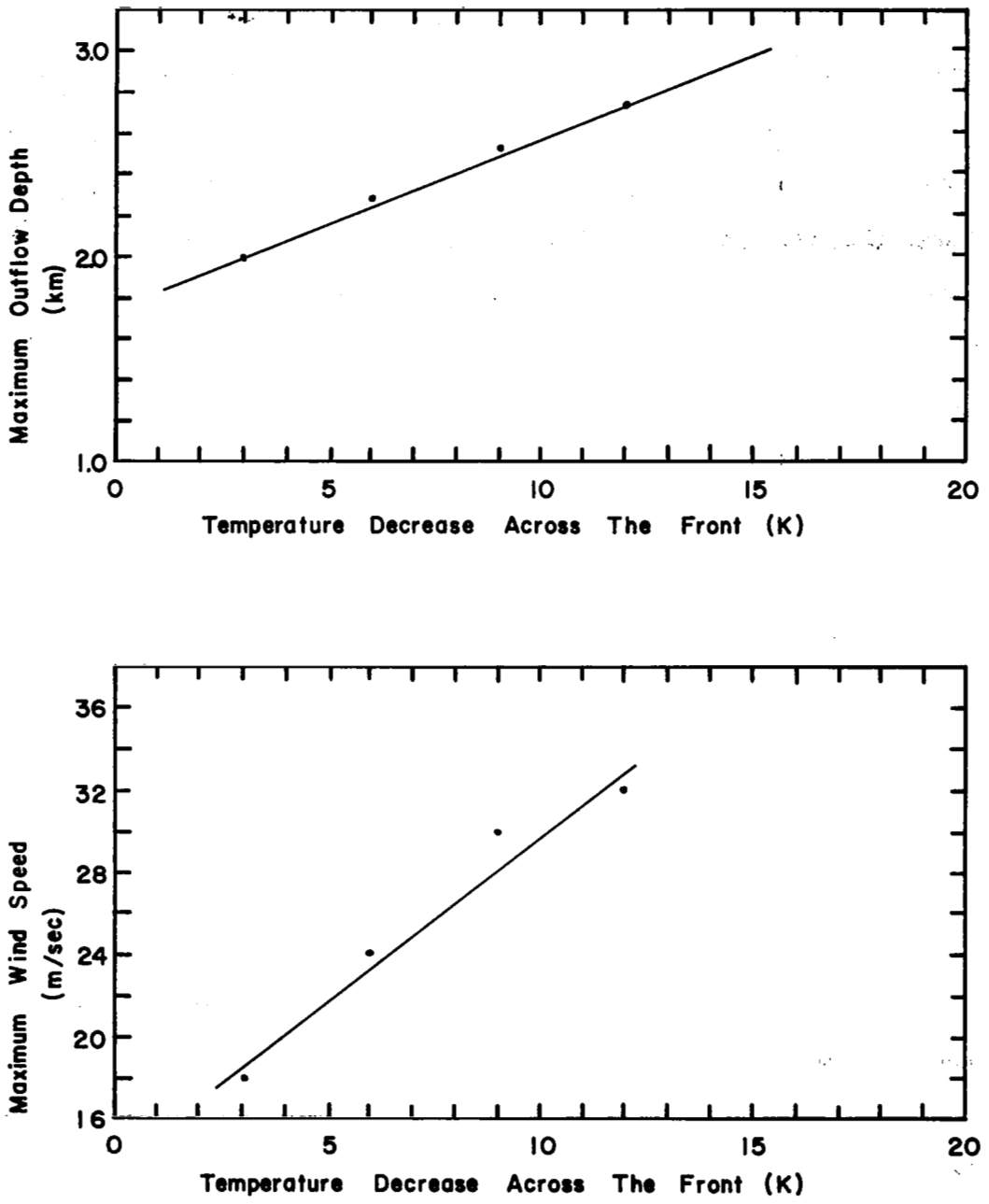

Figure 26. Maximum cold outflow depth is larger (upper diagram) and maximum horizontal wind speed is larger (lower diagram) in those cases that have larger temperature decreases across the front. The temperature decrease in each case was 4 K less than the maximum downdraft temperature depressions indicated by the point values in Figure 25.

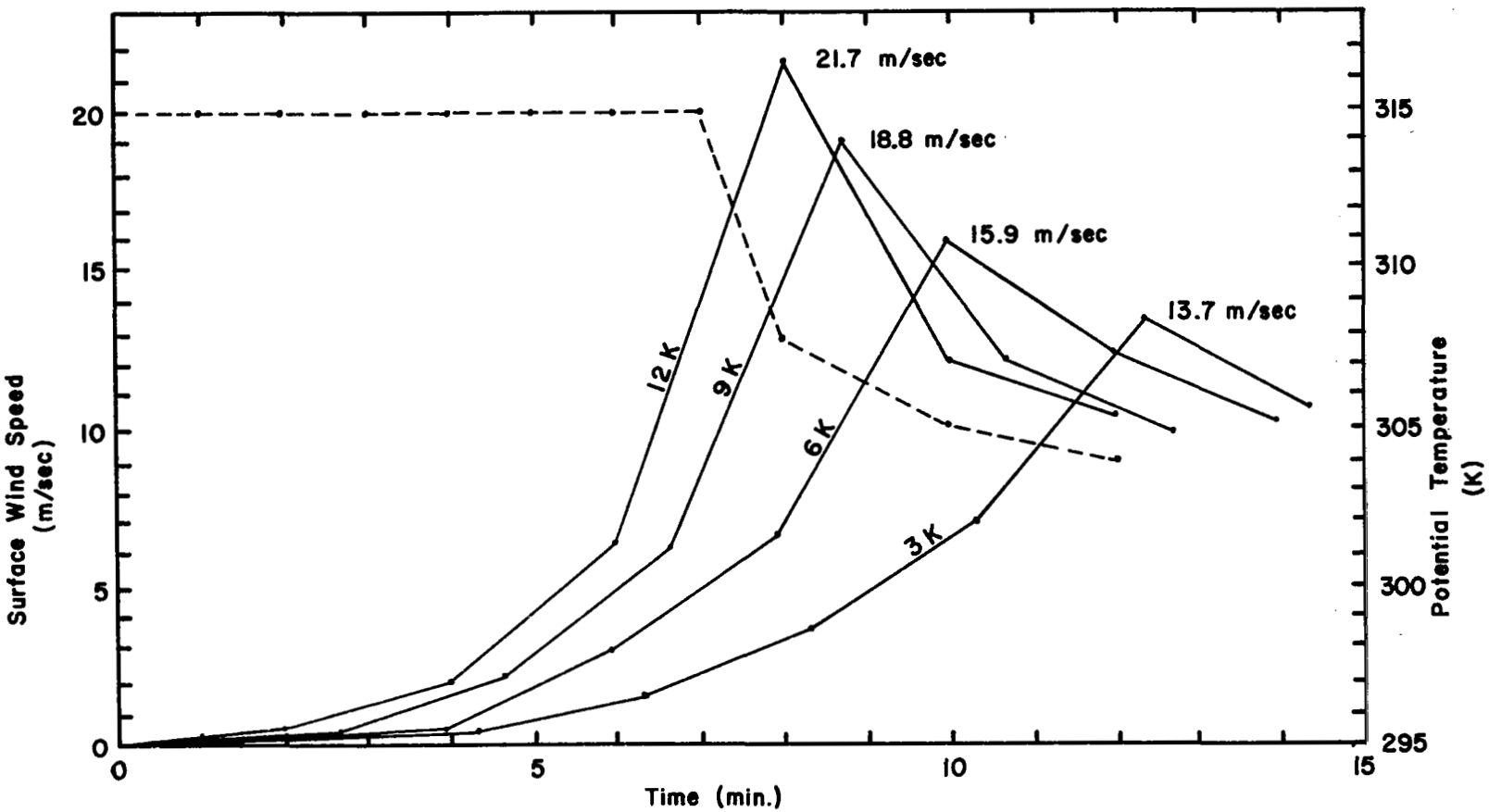

Figure 27. The local variation of wind speed with time at a fixed point at the surface is given for each case by the solid lines. Each profile is labeled with the temperature decrease and the maximum surface wind speed that occurred during frontal passage. The dashed line gives the surface potential temperature variation corresponding to the 12 K case.

the 4 K, 6 K, 9 K, and 12 K cases respectively. These front propagation speeds nearly equal the respective peak surface wind values denoted in Figure 27. This strong correlation between front speed and maximum surface wind just behind the front was observed in all model experiments.

It is interesting to further observe in Figure 27 that after frontal passage, the surface wind speed decreased to nearly the same value (about 12 m/sec) in all four cases. But we have already pointed out that the maximum winds in the strong wind core above the surface were significantly greater in the colder trials (Figure 26). It follows then, that the vertical shear between the surface winds and the strong wind core aloft (labeled C in Figures 14 and 23) is much larger in the colder trials -- increasing from 10 m sec^{-1} km^{-1} in the 4 K case to 23 m sec^{-1} km^{-1} in the 12 K case.

The results in this section have shown that the temperature decrease across the front, or equivalently, the downdraft temperature depression, is an important factor in determining the intensity of a given gust front. But, as Figures 22 through 24 have illustrated, the mature-stage structure of even the coldest case does not depart from that described for the reference case in Section 3.2. Thus, the magnitude of cooling in the downdraft does not appear to alter the quasi-steady configuration of the gust front phenomenon.

4.2 Surface Drag

The accelerating force for the model gust front is the horizontal pressure gradient force that exists between the larger hydrostatic pressure within the cold surge and the lower hydrostatic pressure of

the warm ambient air. The decelerating forces are surface drag and internal shearing stresses. Since the model gust front reaches a steady configuration during its evolution, a dynamic balance must develop between surface drag and shear stresses and the pressure gradient force.

An obvious question then, but one of considerable importance, is how changes in the relative magnitude of these forces might affect the dynamic balance and, in turn, the quasi-steady configuration of the gust front. In the previous section, the pressure gradient force was essentially varied over a large range by varying the temperature contrast across the front. It was found that, although the intensity of the gust front was affected, the steady configuration was not altered.

In this section, we investigate the results from a series of model trials that used a large range of surface drag values. It is found that a very small amount of drag is necessary to explain certain features of the now familiar quasi-steady configuration described in the reference case. However, for all larger values of drag, the gust front quickly reaches and maintains this same configuration.

The nature of the dynamic balance during the mature stage is also examined here. The circulation theorem is utilized to suggest that strong solenoidal accelerations at the front offset the retarding effects of surface drag.

4.2.1 Varying the Drag Coefficient. To test the effects of drag, five model trials were run using the following values of the drag coefficient, C_D in (12): 0.08, 0.04, 0.01, 0.005 and 0.00. Except

for the changes in the drag coefficient, these additional trials are identical to the reference case in which $C_D = 0.02$. It is difficult to specify which coefficient most realistically represents the magnitude of drag expected in the atmosphere. Comparison of model results with available observations seems to suggest that a value of C_D around 0.01 is reasonable. However, our goal in this section is not to determine the most realistic value of C_D, but rather to determine the role of surface drag by varying the value of C_D by more than an order of magnitude.

The most significant results derived from these experiments concern the changes in the horizontal wind field. Figures 28, 29, and 30 depict the horizontal winds when the front is about 12 km from the downdraft for the cases in which C_D equals 0.00, 0.005, and 0.04. These may be compared with the reference case (Figure 14).

When $C_D = 0.00$ (Figure 28), the strongest horizontal winds occur at the surface. Only when drag is introduced (Figure 29) are the surface winds retarded and a core of maximum winds observed above the surface. Surprisingly, for much larger values of the drag coefficient, the height of this maximum wind core does not increase significantly (upper diagram of Figure 31), and the values of the maximum winds observed in the core decrease only slightly (lower diagram of Figure 31).

However, while the maximum wind core aloft is affected relatively little by increasing the drag, the surface winds are significantly affected. This is illustrated in Figure 32, which shows for all six trials the time variation of the surface wind as the gust front approached and then passed a fixed point. As expected, the peak surface wind at the front (labeled A in Figures 14, 29, and 30) was much less for larger

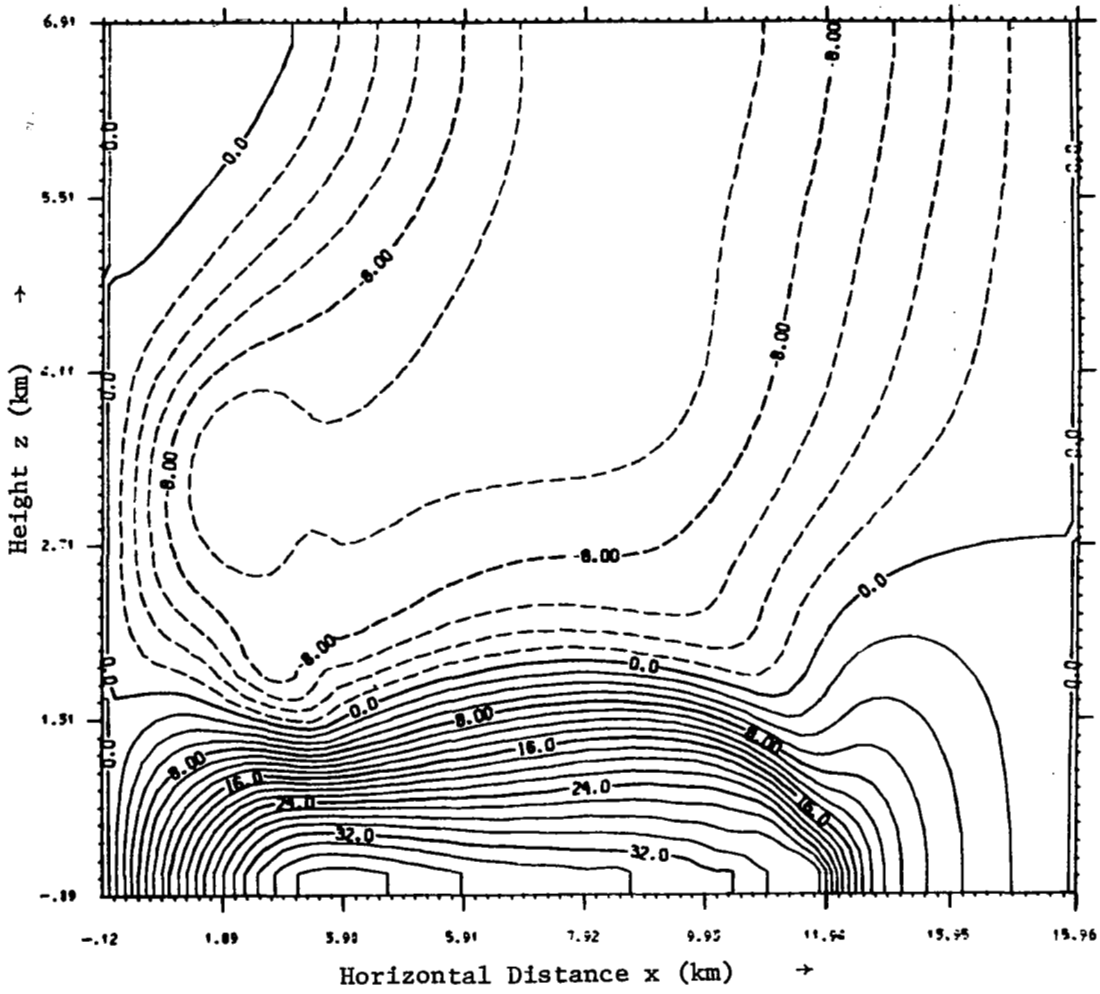

Figure 28. The horizontal wind field (m/sec) at 10.00 minutes for the case in which there is no surface drag (C_D = 0.00). The maximum horizontal winds occur at the surface. Contour interval is 2.0 m/sec.

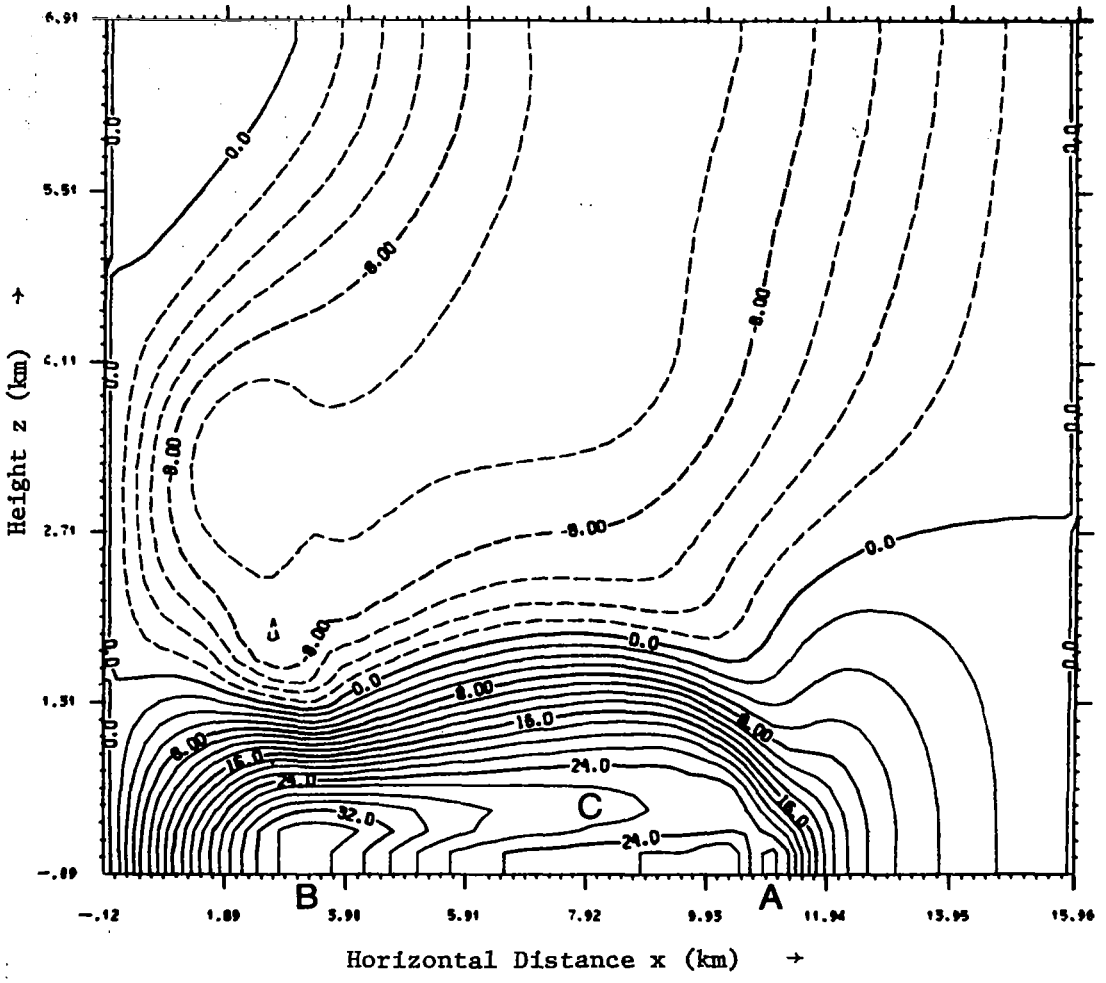

Figure 29. The horizontal wind field (m/sec) at 10.00 minutes for the case in which C_D = 0.005. The relatively small value of surface drag has induced the core of maximum winds above the surface (C) and the two surface wind maxima (A and B). Contour interval is 2.0 m/sec.

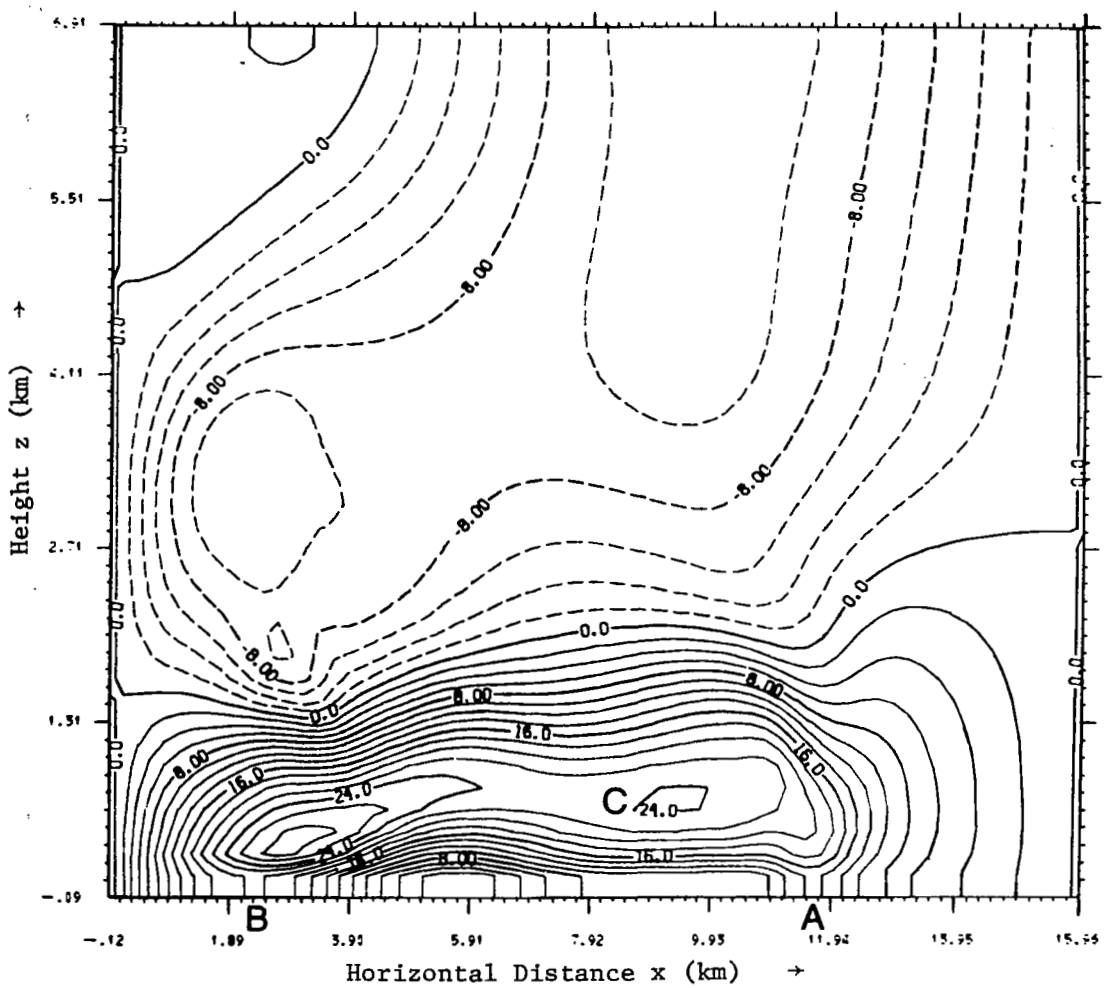

Figure 30. The horizontal wind field (m/sec) at 12.00 minutes for the case in which C_D = 0.04. The relatively large value of surface drag has significantly decreased the surface wind speeds resulting in large vertical shears below the maximum wind core (C). Contour interval is 2.0 m/sec.

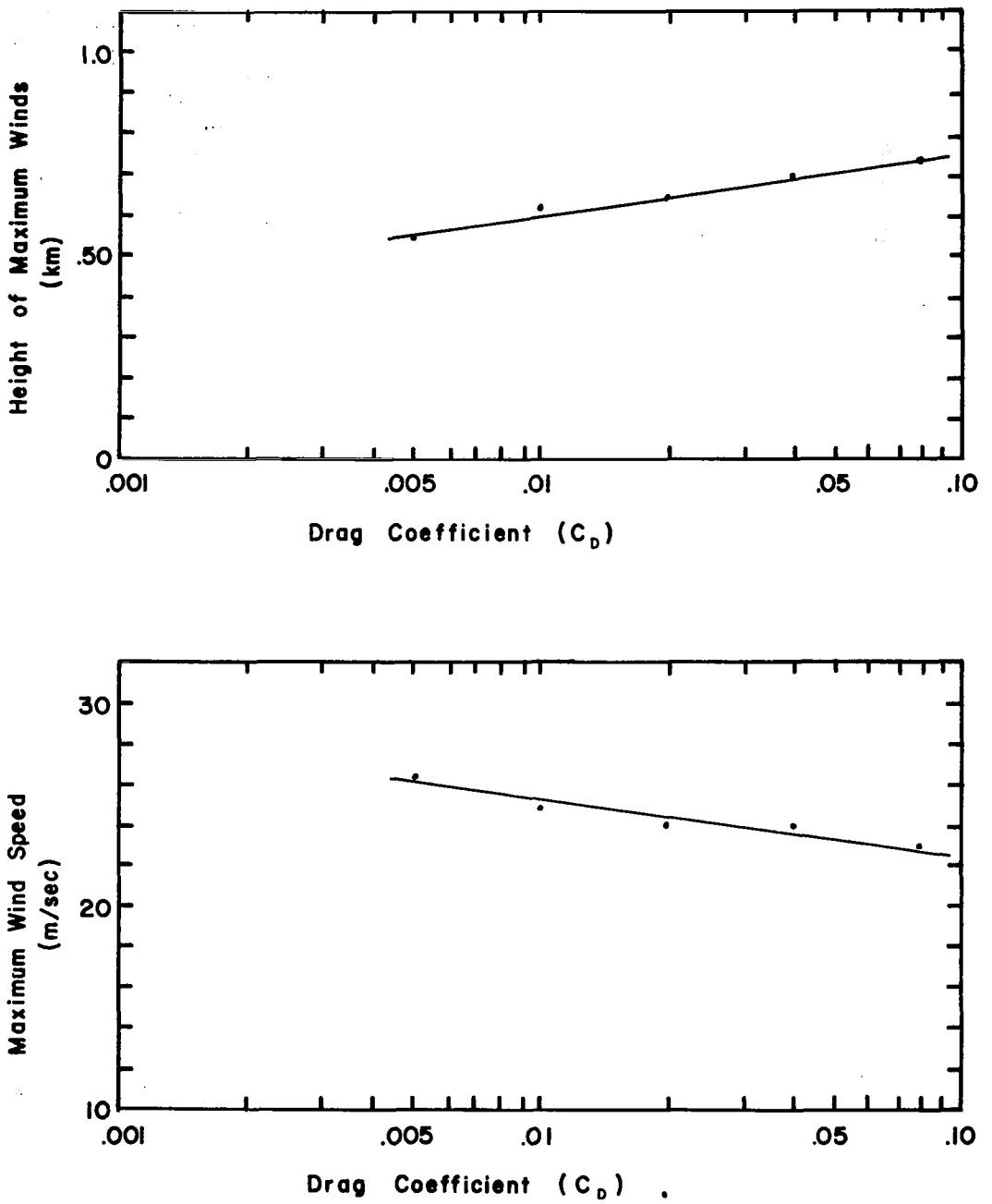

Figure 31. The effect of increasing the drag coefficient, C_D, on the height of the maximum wind core (upper diagram) and on the magnitude of the maximum horizontal winds (lower diagram). The values were determined when the front in each case had propagated outward 12 km.

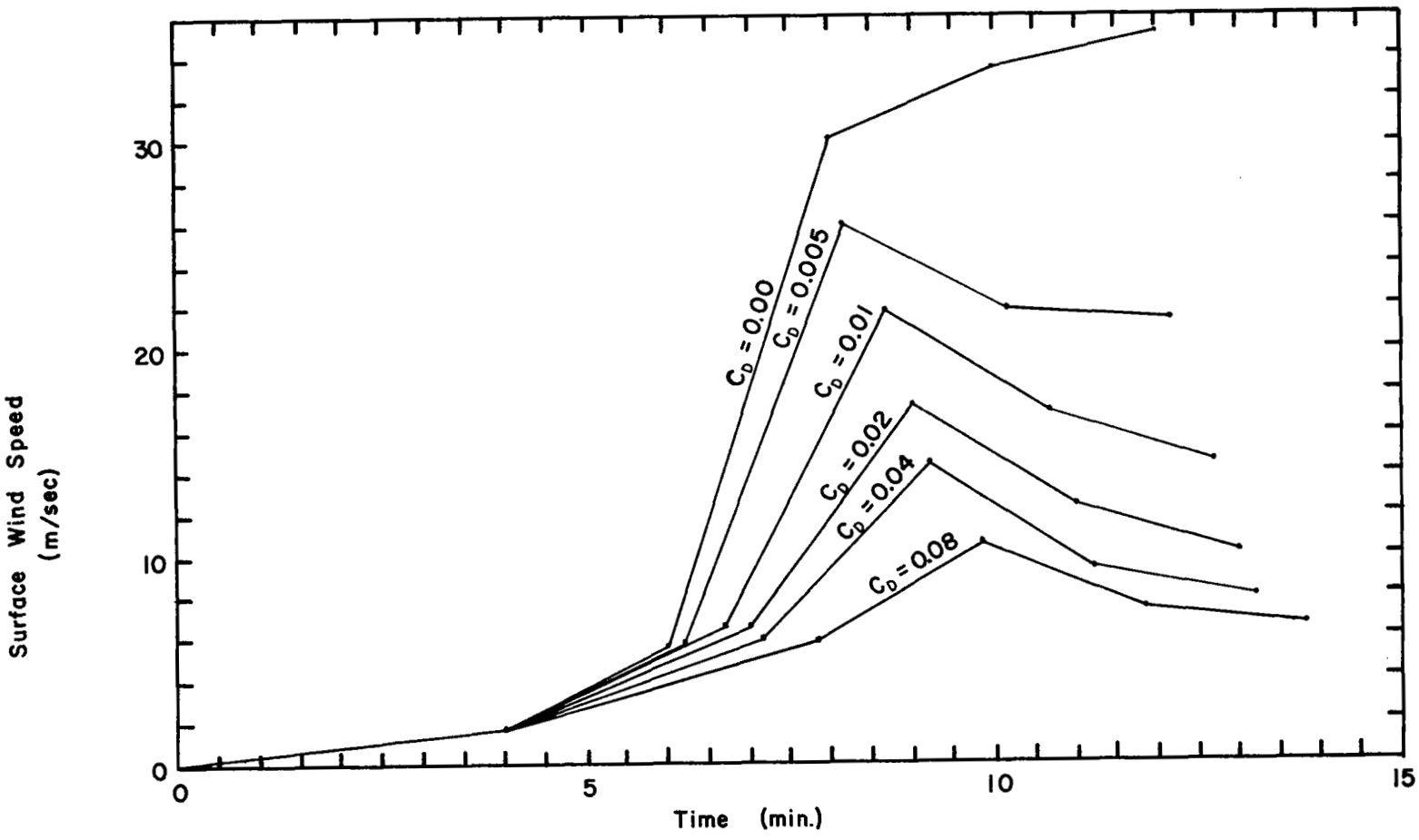

Figure 32. The local variation of wind speed with time at a fixed point at the surface is given for each surface drag case.

drag values. Furthermore, it is evident that, since the peaks occurred sooner in the cases of small drag, the front traveled faster in these instances.

But the most significant fact evident in Figure 32 is the cause and effect relationship between surface drag and the wind velocity jump at the front. For the single case in which there was no drag, the wind speeds increased sharply as the cold surge approached and then they continued to increase, though more slowly, after the cold surge passed. This is verified by Figure 28 in which only one surface maximum is evident far upstream from the front near the downdraft. Yet, for all cases in which drag was included, the wind speeds exhibited a distinct velocity increase and then an abrupt decrease as the front passed. This same result concerning the role of surface drag was observed by Pearson (1973) in his numerical study of a sea-breeze front.

To gain further insight into the wind velocity jump, we consider in Figures 33 and 34 the pressure field that was coincident with the horizontal wind field of the reference case in Figures 14 and 15. The pressure pattern in Figure 33 features two regions of large surface pressure gradient, one at the front and one under the downdraft. But between the front and the downdraft, a region of near-zero pressure gradient is observed.

Figure 34 shows that the surface wind maximum at the front in Figure 15 coincides exactly with the point of transition from large surface pressure gradient to nearly vanishing surface pressure gradient. It is apparent, then, that the increase in the surface wind velocity profile is induced by the strong acceleration provided by the pressure surge coincident with the frontal interface. The sudden falloff of the

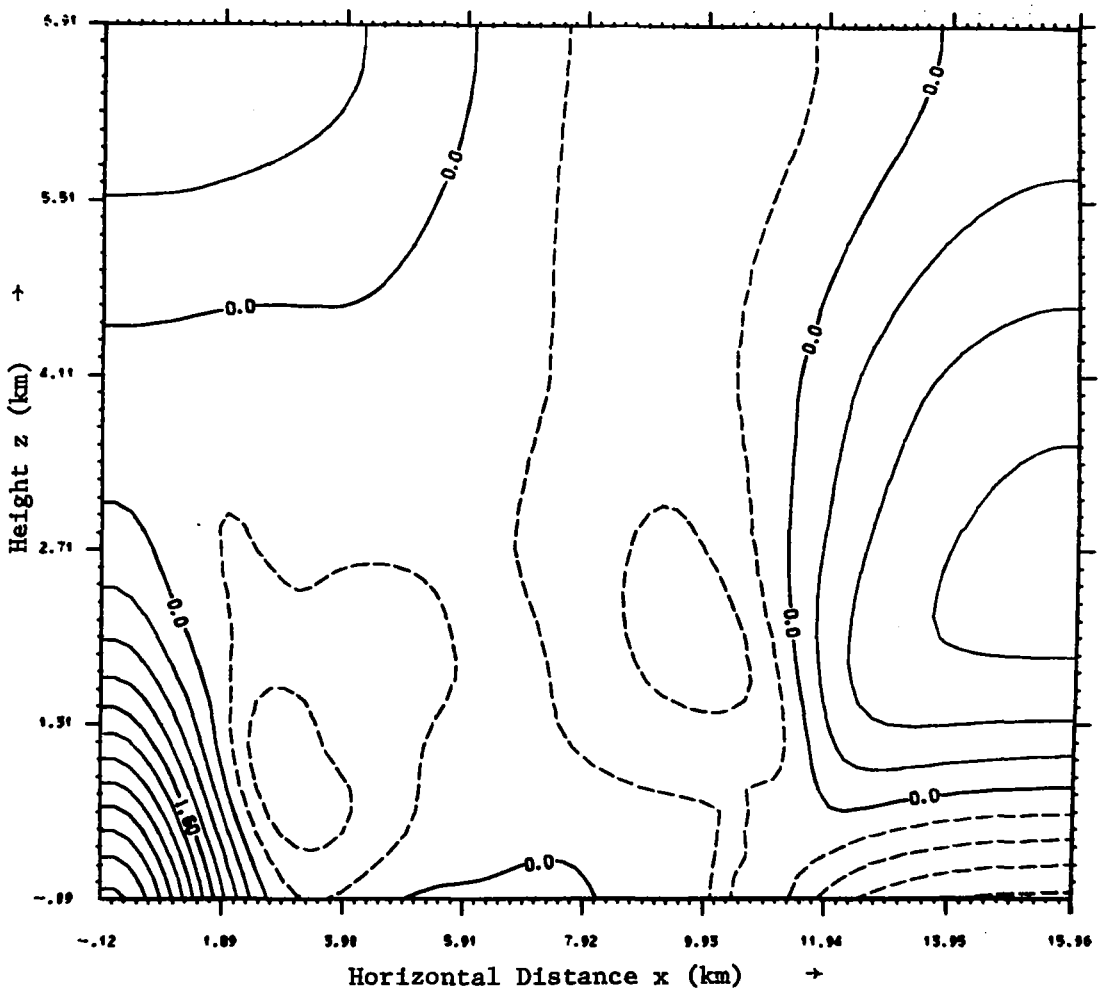

Figure 33. The pressure field accompanying the reference case horizontal wind field at 12.00 minutes in Figure 14. Pressure deviations (mb) from a mean value at each level are given by contours at intervals of 0.40 mb. Solid contours indicate positive deviations. Two regions of large surface pressure gradient are evident near x = 1.5 km and x = 12.0 km.

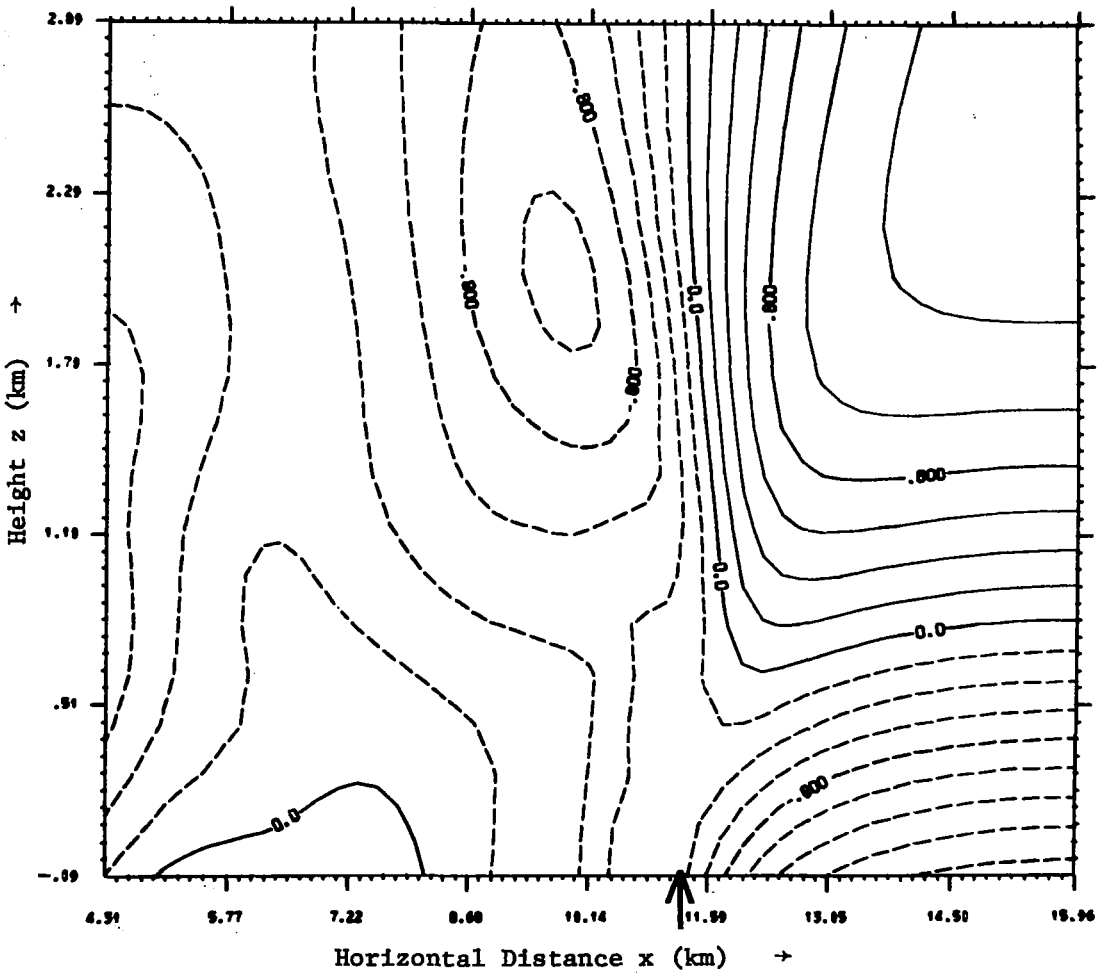

Figure 34. An enlargement of the pressure field in Figure 33 in the region of the front. The arrow denotes the position of the surface wind maximum that is labeled A in Figure 15. Contour interval is 0.20 mb.

wind profile is due to the abrupt decrease in the pressure gradient force just behind the front where the winds rapidly lose momentum to surface drag.

The amplitude of the surface wind velocity jump, though mostly dependent on the relative magnitude of surface drag and pressure forces, may also be influenced by a transfer of momentum from the stronger horizontal winds above the surface. Figure 35 depicts an enlargement of the reference case streamline flow pattern given in Figure 16. A slight downward dip in the flow pattern coincides exactly with the relative maximum of downward motion (A) in Figure 20, as would be expected. More importantly, the surface wind maximum (A) in Figure 15 is located exactly at the transition point between downward and upward motion as indicated by the arrow in Figure 20 and Figure 35.

The maximum of downward motion is related to the subsidence of the coldest, densest air behind the front. It does not appear only intermittently, but is a permanent feature of the gust front motions in the mature stage. Its unique relationship with the position of the surface wind maximum was observed in all model trials. Thus, the subsidence of cold air behind the front appears to transfer momentum downward from the strong horizontal winds aloft and thereby aids in maintaining the surface wind maximum against surface drag.

4.2.2 Shear Effects vs. Solenoidal Accelerations. Since the surface winds behind the front are subject to almost unlimited retardation for increasing values of surface drag (Figure 32), while the strong winds aloft are little changed (Figure 31), large shears of wind speed develop in the model trials with moderate to large drag ($C_D = \geq 0.01$). During actual gust front occurrences, wind tower observations invariably reveal similarly large vertical shears (Colmer, 1971,

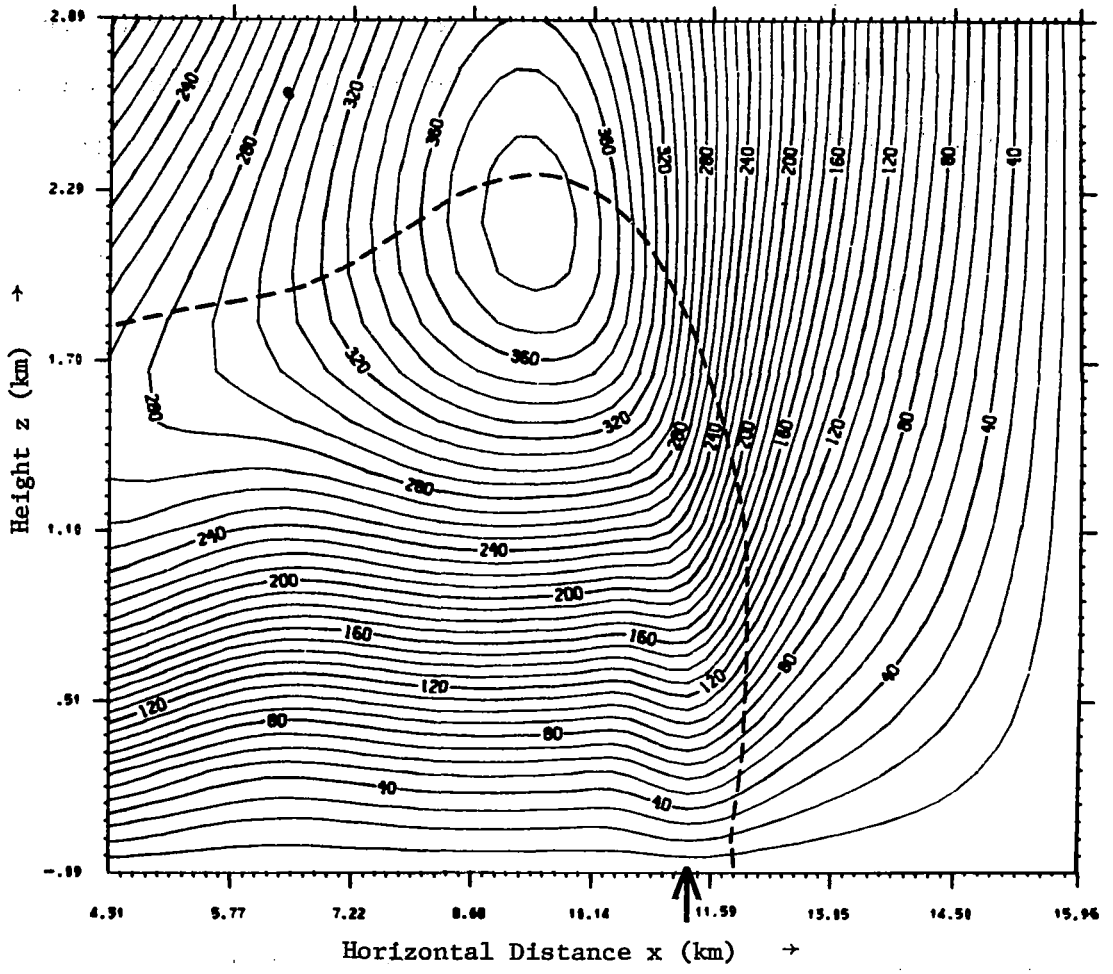

Figure 35. An enlargement of the reference case streamline flow pattern at 12.00 minutes given in Figure 16. The arrow indicates the position of the dip in the flow pattern that coincides with the position of the surface wind maximum in Figure 15. The dashed line represents the frontal interface. Contour interval is 1.0 x 10^7 cm^2/sec and labels are scaled by 1.0 x 10^{-6}.

Charba, 1972, Sinclair, 1973). From such observations, it has long been intuitively realized that a strong wind core above the surface must indeed be a dominant feature within the thunderstorm cold outflow.

This general picture of the wind structure has led several investigators (Colmer, 1971, Charba, 1972) to suggest the repeated occurrence of a collapsing protruding nose phenomenon at the forward edge of the cold outflow. The general argument is depicted in Figures 36 and 37. Due to the faster upper level current, cold air aloft is advected out and beyond a retarded surface front. This protrusion of cold air gives the density interface a nose profile. However, the surface retardation of the density interface is limited by the overturning of the dense air aloft. Once the nose of cold air has extended out far beyond the warm air beneath, it is thought to collapse into the warmer air, then in time reform again as surface friction acts.

Colmer (1971) measured, at various levels up to 478 m, the peak gusts within a gust front, then converted his wind tower measurements at a point to spatial measurements using a mean front propagation speed. The vertical profiles of wind speed that he derived in this manner from many cases were extremely variable and showed both backward and forward slopes. In attempting to relate these wind profiles to the slope of the cold surge thermal profile, Colmer suggested that a protruding nose of cold air forms intermittently and collapses. Charba (1972) mentioned that he had observed wind and thermal structures at the leading edge of several gust fronts "suggestive of all stages of this cyclic process" of nose formation and collapse. In one case, Charba (1972) inferred that at a height of 700 m a protruding nose extended out as much as 1.3 km ahead of a retarded surface front.

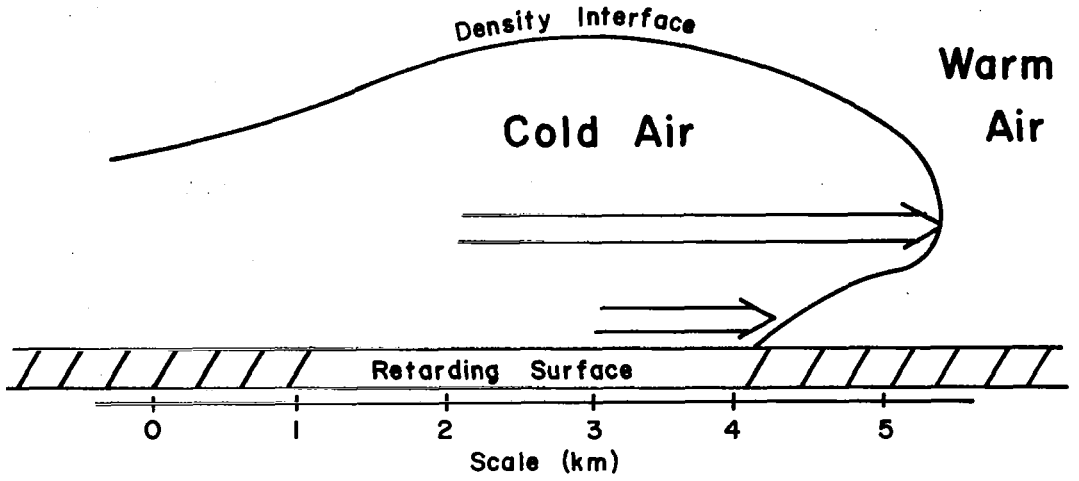

Figure 36. An illustration of the general argument that suggests a large protruding nose of cold air is induced at the cold outflow front by surface drag.

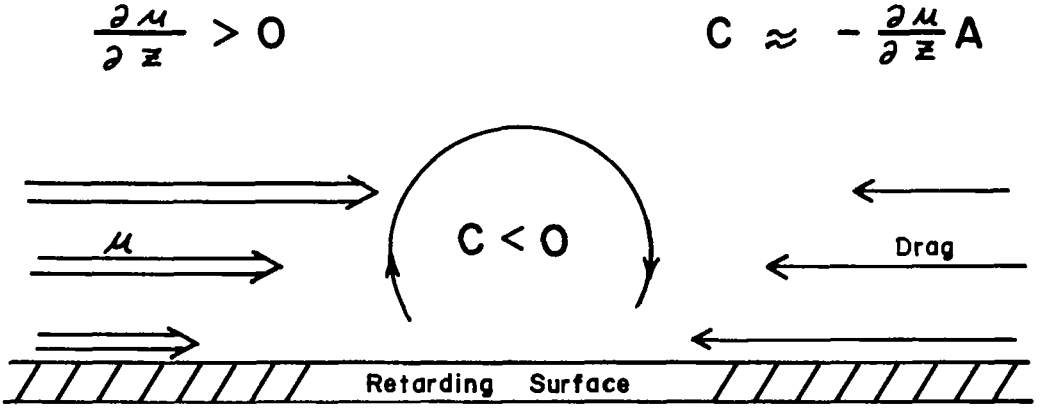

Figure 37. Schematic diagram showing that a large protruding nose of cold air must be associated with a negative circulation.

Studies such as these seem to indicate that surface frictional forces control the behavior of the front. But this conclusion is intuitively dependent on the assumption that the vertical shear of the horizontal wind at the front is large (Figure 36). In Section 3.2, it was shown that at the frontal interface, the vertical shear of the horizontal wind was in fact small. In this section, the circulation theorem is invoked to suggest that solenoidal forces at the front offset the effects of surface friction and reduce the vertical shear at the front.

Figure 38 shows the properly scaled potential temperature surfaces during the mature stage for the three cases in which C_D = 0.01, 0.04, and 0.08. Many of the previous figures in this work are stretched in the vertical to enhance visual resolution, but this stretching tends to deemphasize any protruding nose profile. In Figure 38, the scaling is such that 1.0 km in the horizontal is represented by the same distance as 1.0 km in the vertical.

For drag values as large as C_D = 0.01, it is apparent that no protruding nose of cold air develops in the model and that the frontal interface is vertical in the low levels. In the second case (C_D = 0.04), a slight nose is apparent, but only in the extreme case (C_D = 0.08) does a significant protruding nose become evident, and then it extends out beyond the surface front by only 0.7 km. Furthermore, from 6 minutes to 14 minutes this nose maintained the configuration shown without showing any tendency to protrude further and collapse. Thus, in virtually all model trials in which a protruding nose was observed, it was a steady feature and did not exhibit a cyclic process of formation and collapse.

Figures 39 and 40 show an enlargement of the horizontal winds and vertical velocities in the vicinity of the front at 12 minutes for the

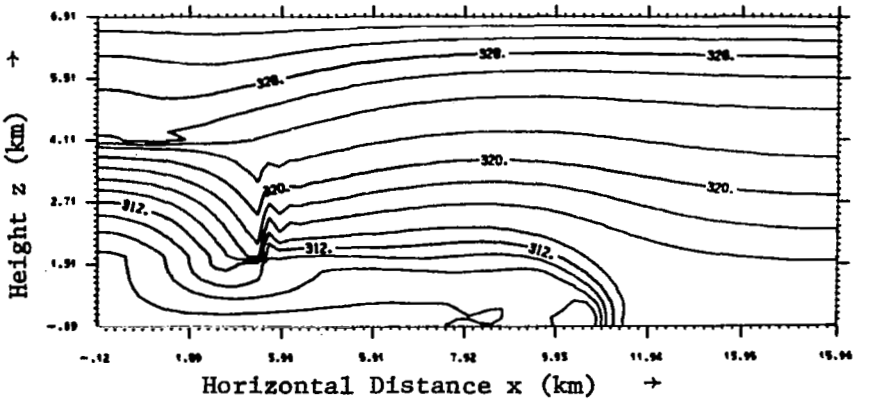

A. C_D = 0.01

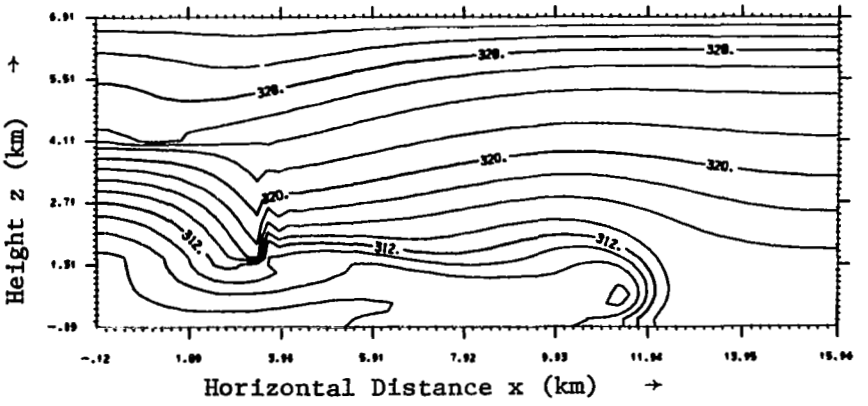

B. C_D = 0.04

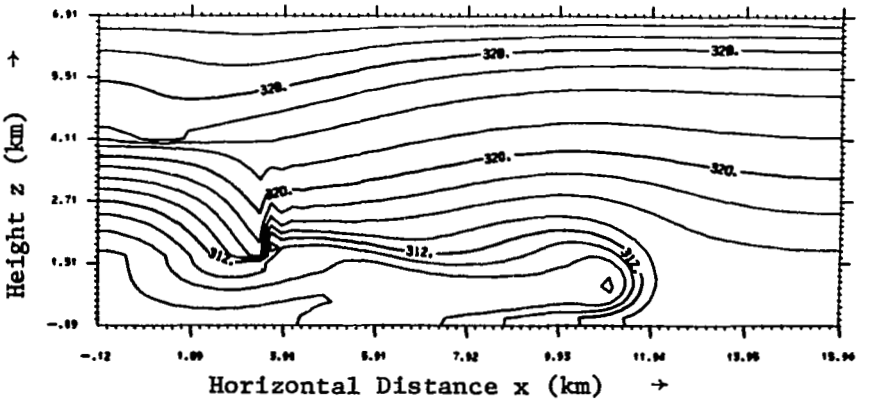

C. C_D = 0.08

Figure 38. The mature-stage potential temperature fields (K) for three surface drag experiments illustrating that a significant nose of cold air formed at the frontal interface only in the most extreme case, C_D = 0.08. Contour interval is 2.0 K.

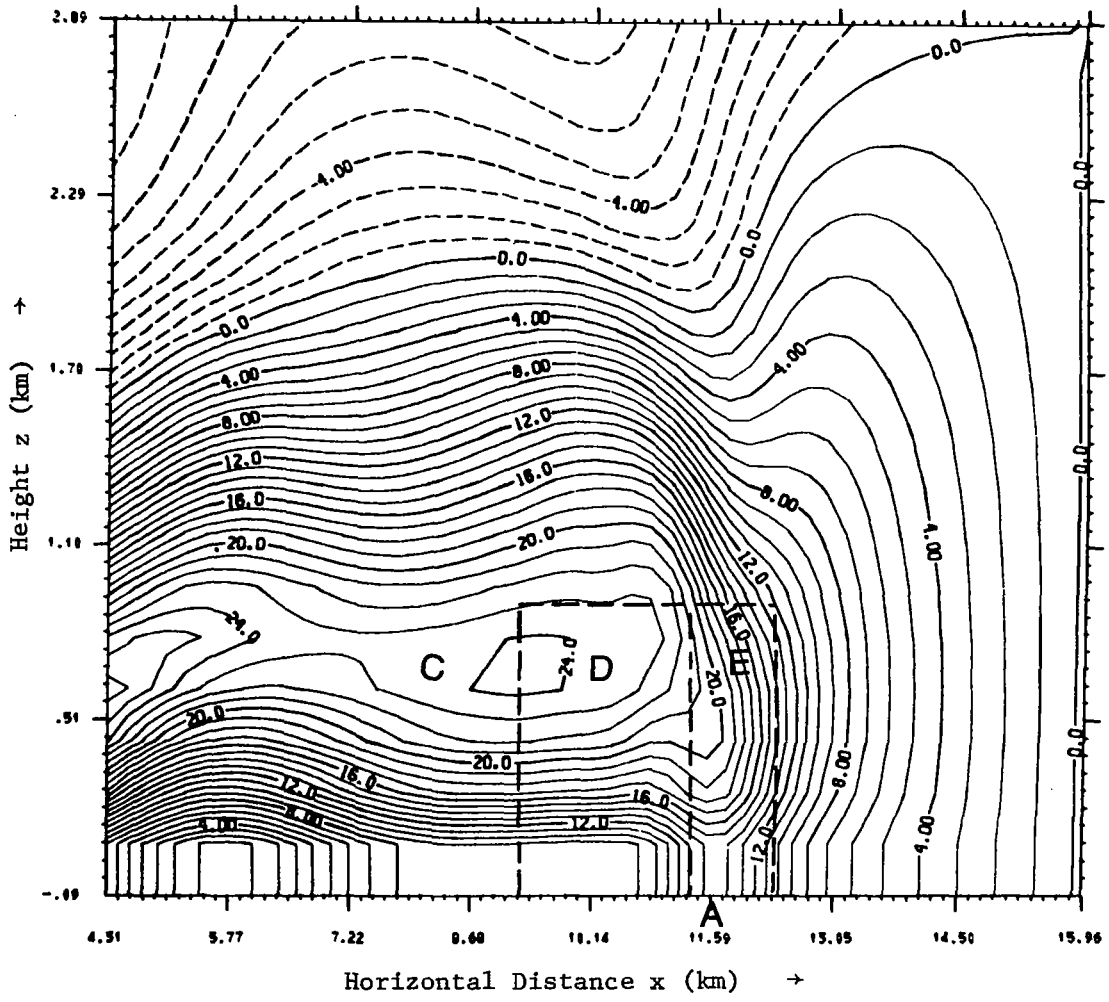

Figure 39. An enlargement of Figure 30 showing the horizontal wind field (m/sec) at the front at 12.00 minutes for the case in which C_D = 0.04. The two boxes labeled D and E are regions of negative and positive circulation respectively. Contour interval is 1.0 m/sec.

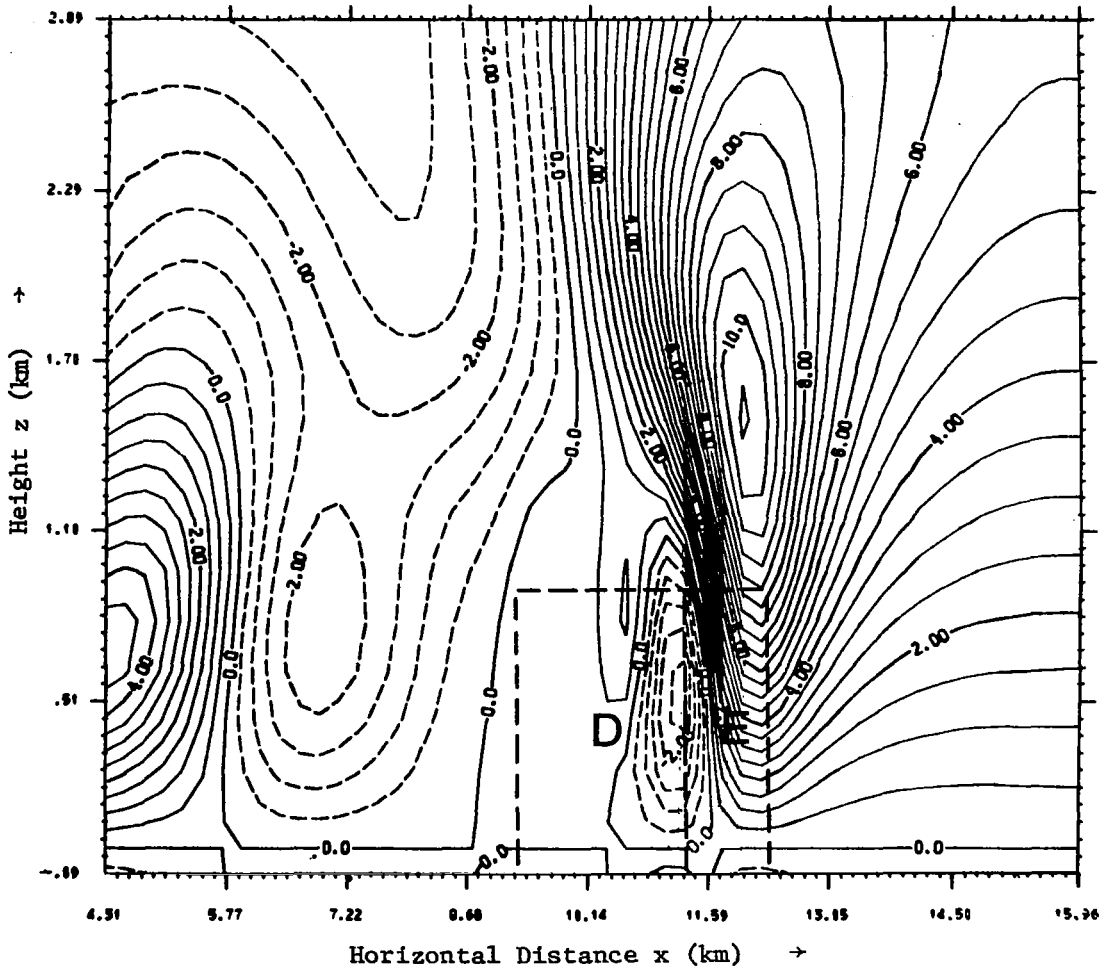

Figure 40. An enlargement of the vertical velocity field (m/sec) at the front at 12.00 minutes for the case in which C_D = 0.04. The two boxes labeled D and E are regions of negative and positive circulation respectively. Contour interval is 0.50 m/sec.

$C_D = 0.04$ case. The boxed-in regions indicate areas in which we shall examine the implications of the circulation theorem.

The circulation, C, is defined as the integral

$$C = \oint (\underset{\sim}{V} \cdot \underset{\sim}{\tau})\, ds \tag{31}$$

of the fluid velocity component parallel to a given closed path. Qualitatively, then, the circulation is a measure of fluid spin. The circulation of the given regions in Figures 39 and 40 can be determined from the vorticity, ξ, by using Stokes's theorem and the mean value theorem to express (31) equivalently as

$$C = \bar{\xi}(A) = \left(\overline{\frac{\partial w}{\partial x}} - \overline{\frac{\partial u}{\partial z}}\right)A \quad , \tag{32}$$

where A is the area of the region and the overbar denotes the average over the area.

The arguments that suggest a collapsing nose feature is dominant in the motions at the front never address the importance of the $\frac{\partial w}{\partial x}$ term in (32). Rather, the $\frac{\partial u}{\partial z}$ term is emphasized, which implies a negative circulation at the front as pictured in Figure 37.

From Figures 39 and 40, it is apparent that region D, which is behind the front, is indeed characterized by a large negative circulation since friction dominates and the $\overline{\frac{\partial u}{\partial z}}$ term is large. Even the smaller $\overline{\frac{\partial w}{\partial x}}$ term contributes to a negative circulation. But in region E, which is at the front, the isotachs of the horizontal wind are nearly vertical (Figure 39), but the horizontal gradient of vertical velocity is large and positive (Figure 40). Thus in region E, a large $\overline{\frac{\partial w}{\partial x}}$ term dominates a small $\overline{\frac{\partial u}{\partial z}}$ term, resulting in a strong positive circulation.

In Section 3.2 it was shown that air parcels in the strong wind core above the surface travel significantly faster than the front. The front associated with Figures 39 and 40 propagated at a mean speed of 15 m/sec between 6 and 14 minutes while winds in the strong wind core attained speeds of 24 m/sec. Consequently, parcels in the strong wind core pass through region D and into region E, thereby attaining a strong positive circulation. This process was evident in Section 3.2 in the strong upward curvature experienced by air parcels as they approached the frontal interface.

The circulation theorem can be used to further study the positive change in circulation with time following these air parcels. The theorem that applies to system (1) - (4) (without the viscosity terms) is given by

$$\frac{dC}{dt} = -\iint_A \underset{\sim}{\eta} \cdot (\nabla\alpha \times \nabla P)\, dA \quad , \tag{33}$$

where α is specific volume, $1/\rho$, and $\underset{\sim}{\eta}$ is the outward unit normal perpendicular to area A. For the purposes of this analysis, (33) can be more conveniently expressed as

$$\frac{dC}{dt} = -R\iint_A \underset{\sim}{\eta} \cdot (T\,\nabla \ln\theta \times \nabla \ln P)\, dA \quad . \tag{34}$$

This states that a solenoidal field, which exists when potential temperature surfaces are inclined to pressure surfaces, accelerates the fluid parcels within the given area, A, to produce a change in the circulation. The change will be positive or negative depending on the orientation of the potential temperature gradient to the pressure gradient.

The relationship in (34), when applied at the forward edge of the cold surge, illustrates that the configuration of the strong solenoidal field is consistent with the positive circulation acceleration of air parcels at the front. This is illustrated in Figure 41, which shows the large potential temperature gradient and the large angle between it and the pressure gradient. The bottom of Figure 41 further illustrates that the orientation of the gradient vectors indicates a positive circulation acceleration.

It is now more apparent how a dynamic balance is achieved at the front. Upstream from the front, a large vertical shear of wind speed is indeed induced by surface drag. However, when the fastest moving parcels enter the strong solenoidal field at the front, the positive circulation acceleration induces a large vertical velocity component and the parcels curve sharply upward. The vertical shear of the horizontal wind is thereby greatly reduced at the front and the frontal interface remains nearly vertical.

The strong solenoidal field at the front is, of course, strongly related to the strong local pressure gradient. In fact, the consideration of solenoidal accelerations may be viewed as an alternate, and sometimes more informative, method of examining pressure gradient forces. Thus, the analysis in this section has further confirmed the balance that is achieved between surface drag forces and pressure gradient forces at the front.

The cold surge modeled here is similar to the gravity currents modeled in laboratory tank experiments in which a lateral partition is placed initially between two fluids of different density. When the partition

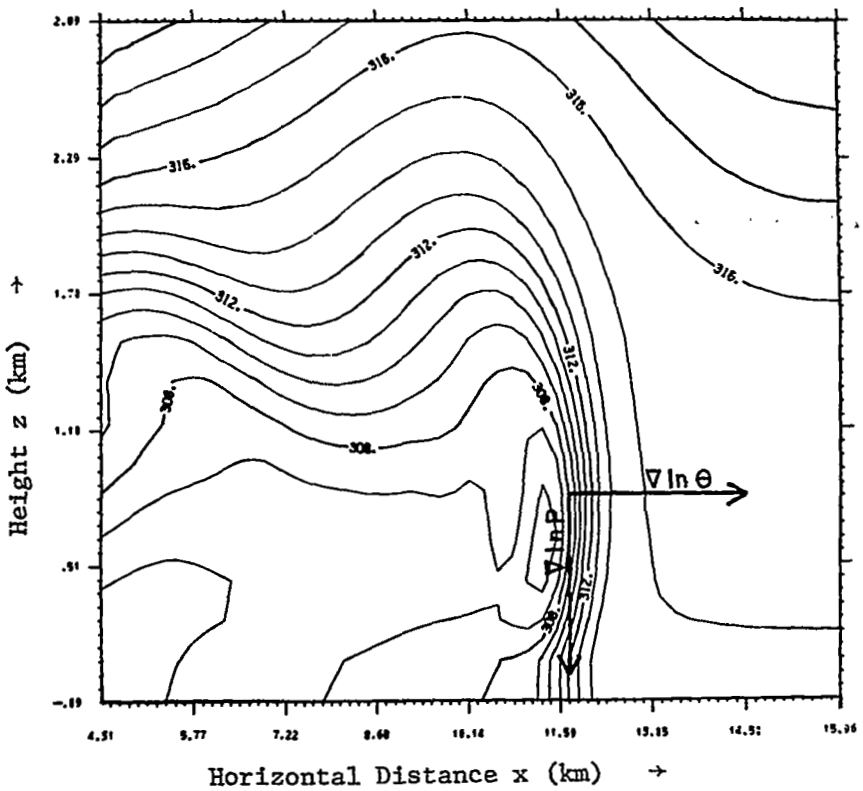

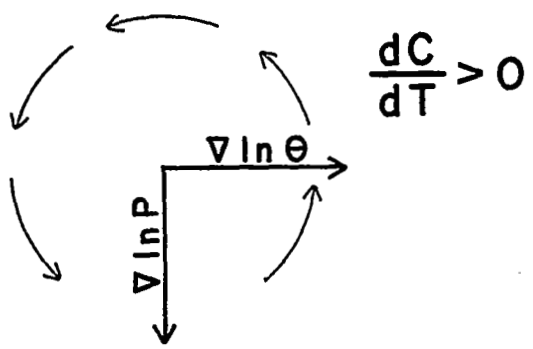

$$-(T\ \nabla \ln \theta \times \nabla \ln P)$$

Figure 41. An enlargement of the potential temperature field (K) at the front at 12.00 minutes for the case in which $C_D = 0.04$. The orientation of the potential temperature gradient vector and the pressure gradient vector indicates a positive circulation acceleration at the front.

is removed, a transient stage is observed during which the more dense fluid begins to move out and undercut the less dense fluid.

In a short time however, these laboratory density surges also achieve a quasi-steady configuration. They often exhibit a constant displacement speed and a steady geometric shape led by an elevated head of dense fluid with a projecting nose profile. As in the present model, the nose is a steady feature and projects over the ambient fluid only slightly (Simpson, 1969). Furthermore, Benjamin (1968) determined that a dynamic balance also exists between shear stresses and the pressure gradient force in the steady phase of gravity currents. It is apparent from these results that a high degree of dynamic similarity exists between laboratory gravity currents and the model gust front.

Charba (1972) demonstrated, in a case study of a severe thunderstorm gust front, that thunderstorm cold outflows also appear to be dynamically similar to laboratory gravity currents. He argued that pressure gradient forces and frictional shear stresses were the dominant forces and were in approximate balance within the cold surge. He suggested however, as mentioned before, that frictional forces may dominate at the forward edge of the cold surge.

But if the dynamics of thunderstorm cold outflows are indeed largely determined by pressure gradient forces and frictional forces, the present model prototype (supported by the results of laboratory gravity current experiments) strongly indicates that the mature stage of the gust front may be characterized by a balance of these forces throughout. A cyclic process of formation and collapse of a protruding nose of cold air, though still feasible, must be regarded as a dominant feature only in those cases in which shear effects are large enough to overcome the strong solenoidal accelerations.

4.3 Ambient Stability

In the numerical experiments presented thus far, the ambient stability of the initial state has not been varied. In an attempt to assess the importance of the basic state stability, the model was initialized with five different vertical temperature profiles (Figure 42).

Four of the five profiles in Figure 42 are labeled with a Brunt-Vaisälä frequency, ω, defined as

$$\omega = \left(\frac{g}{\Theta_o(z)} \frac{\partial \Theta_o(z)}{\partial z}\right)^{1/2} \quad , \tag{35}$$

in which $\Theta_o(z)$ is the initial ambient potential temperature profile. Each given ω represents an average value over the lowest 2.0 km of the respective profile. The profile with $\omega = 0.75 \times 10^{-2}$ sec^{-1} was previously given in Figure 2 and was used in all the model trials discussed thus far. The unlabeled profile is characterized by a strong inversion above a neutral lower layer and is representative of the type of profile often associated with very severe thunderstorms. The inversion, however, makes it difficult to determine a representative ω value in this case.

Except for ambient stability, ω, all model parameters are identical in the five trials presented in this section. The surface drag coefficient is $C_D = 0.02$, and the maximum downdraft temperature depression is the same in each trial. But, since the temperature depression is modified by dry-adiabatic warming in the low levels of the downdraft, the resulting thermal contrast at the front is dependent on the lapse rate of potential temperature in the lowest levels. Therefore, the temperature contrast across the front is not equivalent in any of the five cases as shown in the upper diagram of Figure 43. It varies significantly from 11 K for the neutral case to 3 K for the most stable case.

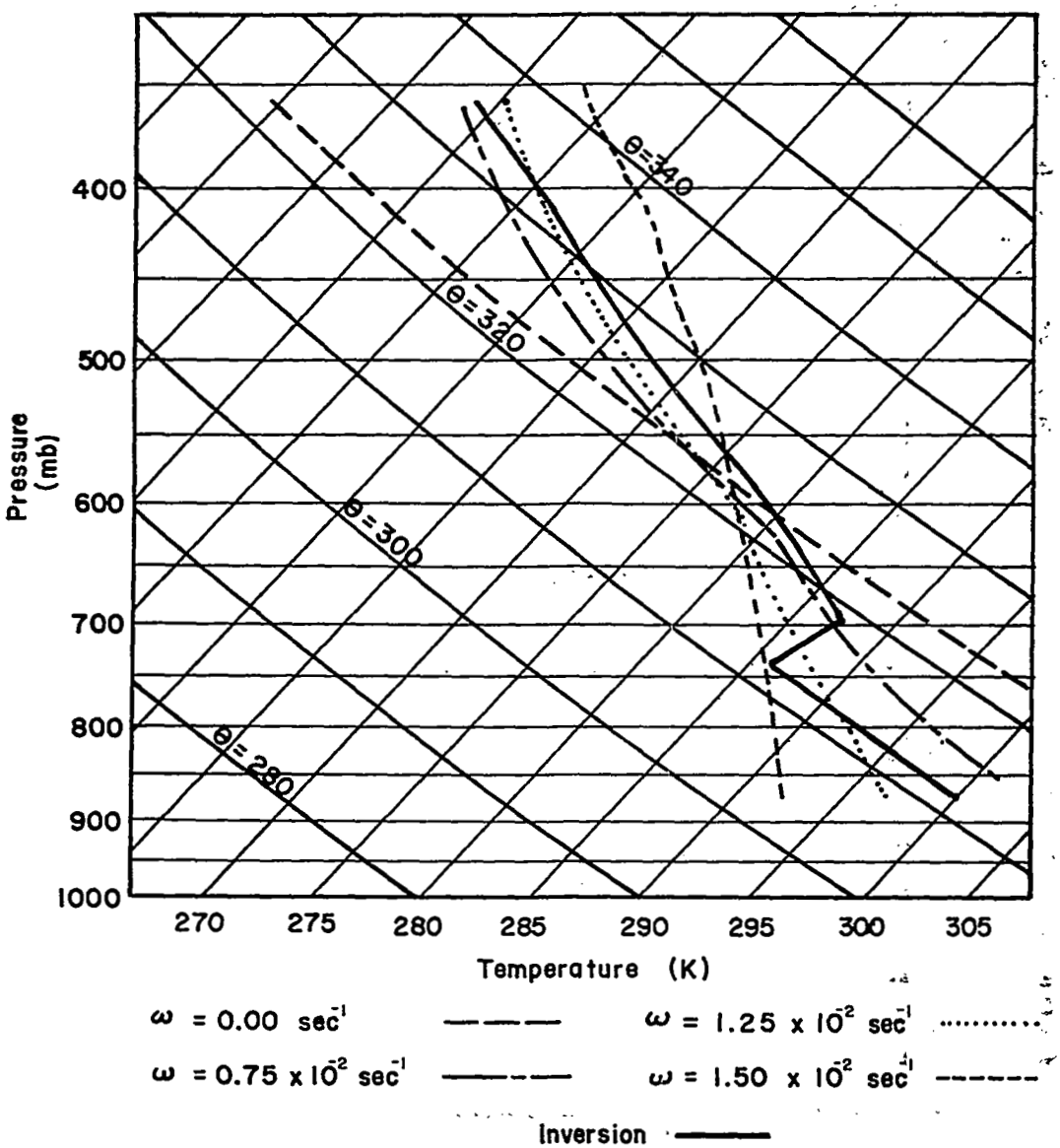

Figure 42. Skew T-Log P diagram showing the ambient temperature profiles that were used in the five stability experiments.

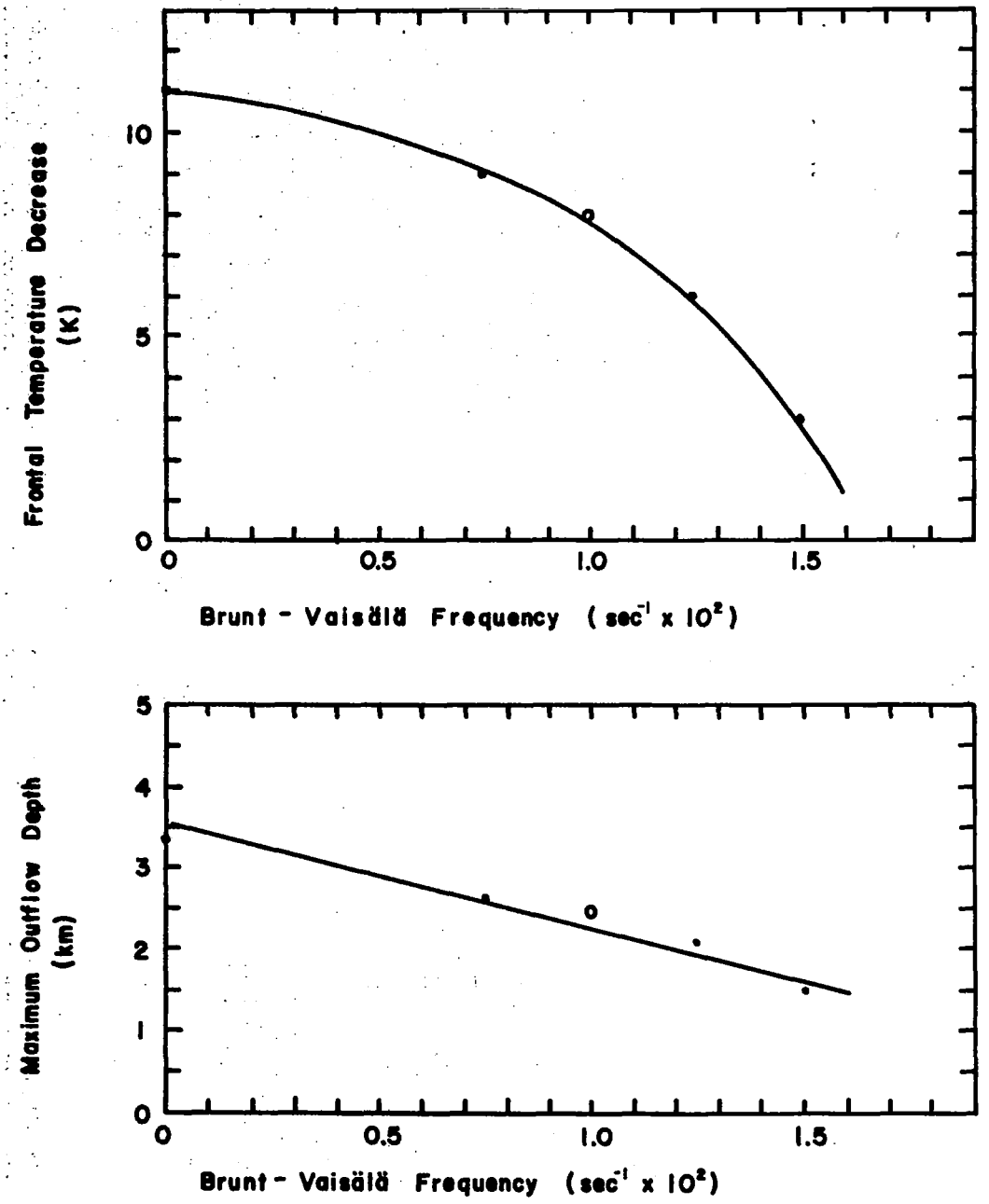

Figure 43. The temperature decrease across the front is larger (upper diagram) and the cold outflow depth is larger (lower diagram) in those cases with neutral or nearly neutral ambient stability. The open circle dot in these graphs represents the inversion case.

Thus, the results from these trials concerning ambient stability are significantly influenced by the effects of varying the magnitude of the temperature contrast across the front. But since these effects were examined independently in Section 4.1, it is possible to discern here those effects resulting primarily from the variations in basic state stability. The stability effects are illustrated in Figures 44 through 50. Figures 45, 46, and 47 give the potential temperature field, horizontal wind field, and streamline flow field respectively at 12 minutes for the neutral case, $\omega = 0.0\ sec^{-1}$; and Figures 48, 49, and 50 give the same fields for the stable case, $\omega = 1.25 \times 10^{-2}\ sec^{-1}$.

From Figures 45 and 48 it is evident that the depth of the cold outflow is much greater for the nearly neutral ambient states. The tendency is shown for all cases in the lower diagram of Figure 43. Simultaneously, the wind surge at the front is deeper and the maximum wind core aloft is observed at a higher level (upper diagram of Figure 44 and Figures 46 and 49).

The streamline flow patterns of Figures 47 and 50 clearly illustrate why, in general, all height scales are larger in the neutral cases. The vigorous downdraft in the neutral case literally rebounds off the surface since there is no damping of vertical motions by stable stratification. The coldest air is carried aloft until it finally collapses to the surface. This gives rise to a larger relative maximum of downward motion behind the front in the neutral case (lower diagram of Figure 44).

This strong subsidence of cold air is also evident in the larger amplitude dip in the streamline pattern at the front (Figure 47) and indicates a greater transfer of momentum from aloft to help sustain a larger surface wind maximum. This observation is supported by comparing

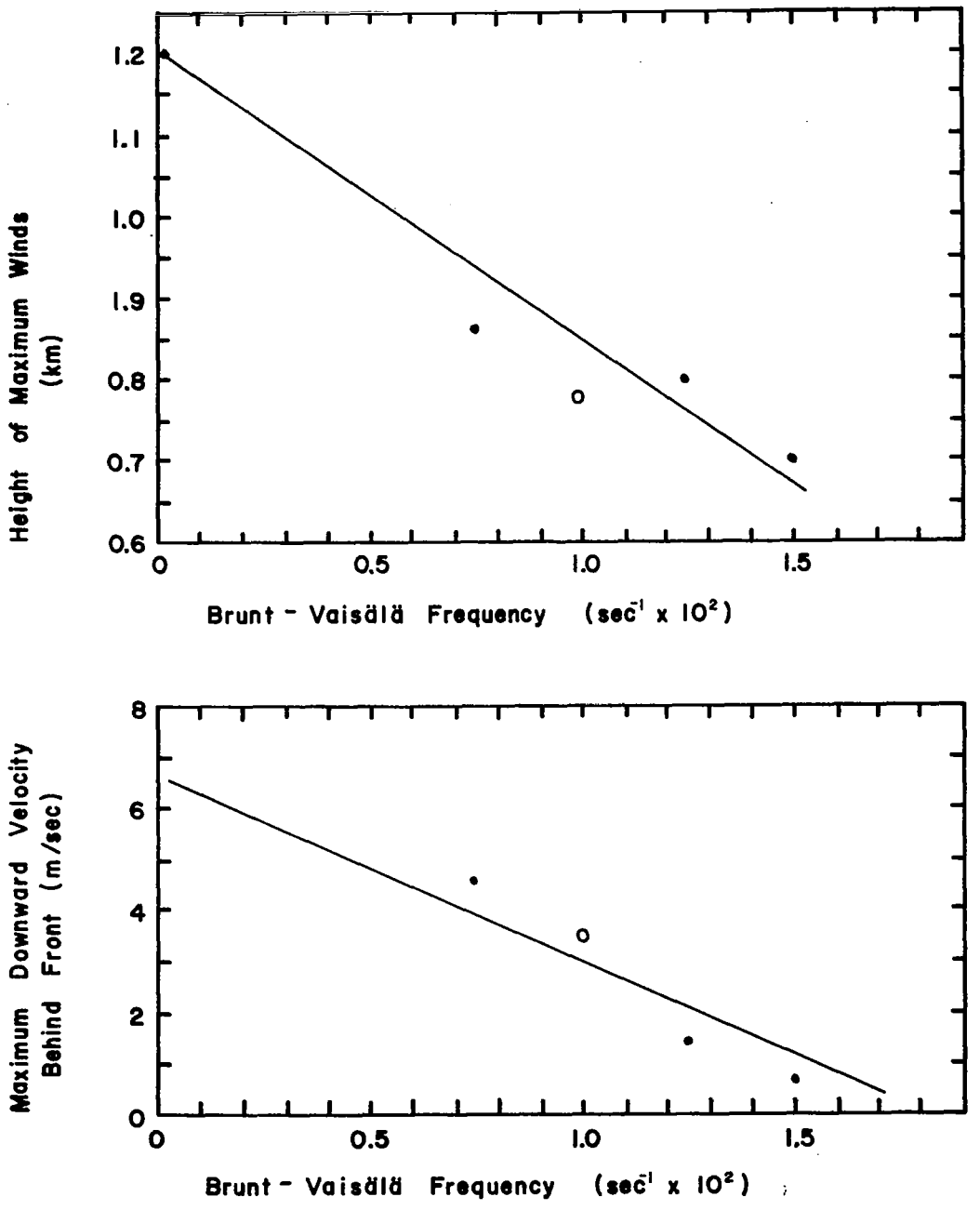

Figure 44. The height above the surface of the core of maximum winds is greater (upper diagram) and the subsidence of cold air just behind the front is greater (lower diagram) in those cases with neutral or nearly neutral ambient stability. The open circle dot in these graphs represents the inversion case.

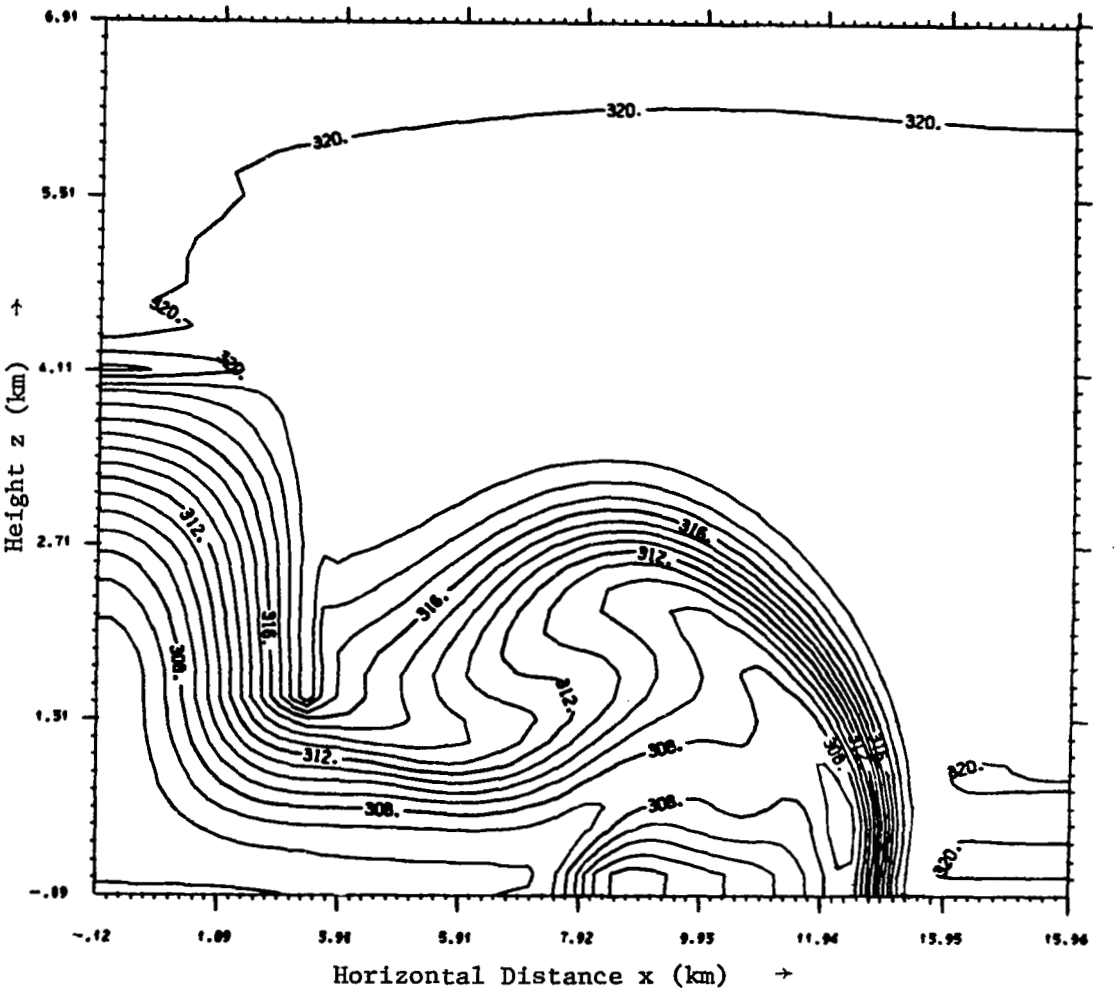

Figure 45. The potential temperature field (K) at 12.00 minutes for the neutral case in which $\omega = 0.00$ sec^{-1}. The cold outflow exhibits a maximum depth of 3.40 km. Contour interval is 1.0 K.

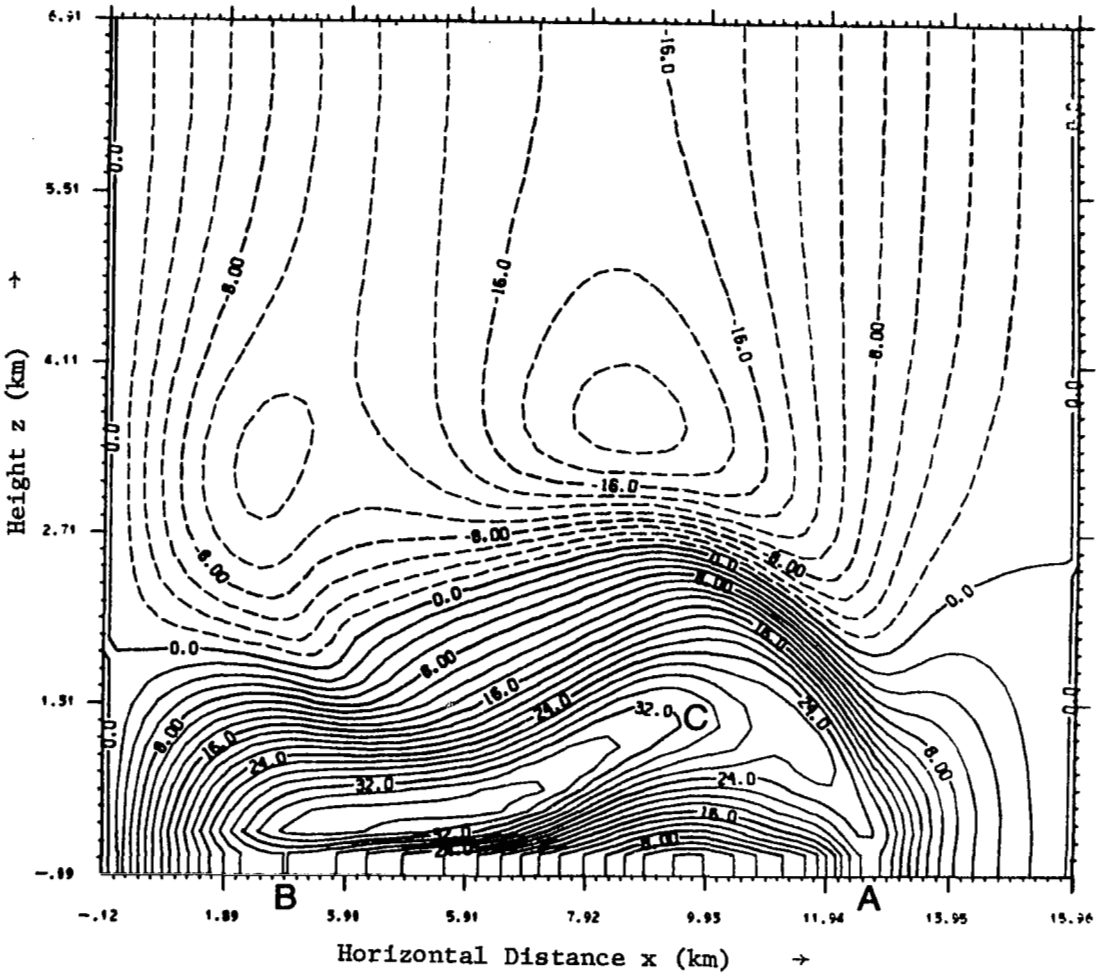

Figure 46. The horizontal wind field (m/sec) at 12.00 minutes for the neutral case in which $\omega = 0.00\ sec^{-1}$. The core of maximum winds above the surface (labeled C) is observed at a maximum height of 1.20 km. Contour interval is 2.0 m/sec.

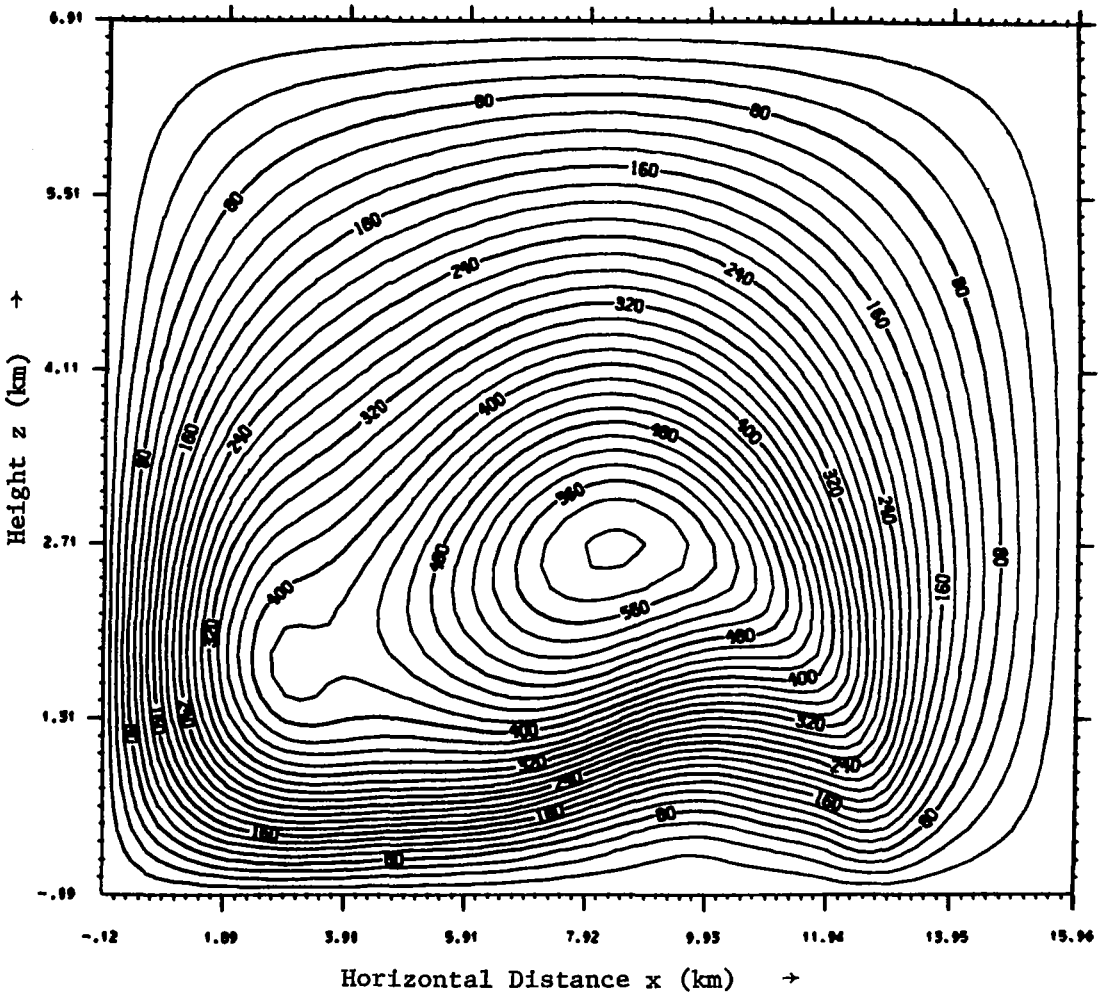

Figure 47. The counterclockwise streamline flow pattern at 12.00 minutes for the neutral case in which $\omega = 0.00\ sec^{-1}$. A large amplitude dip in the flow pattern is evident in the low levels between x = 10.0 km and x = 13.0 km. Contour interval is $2.0 \times 10^7\ cm^2/sec$ and labels are scaled by 1.0×10^{-6}.

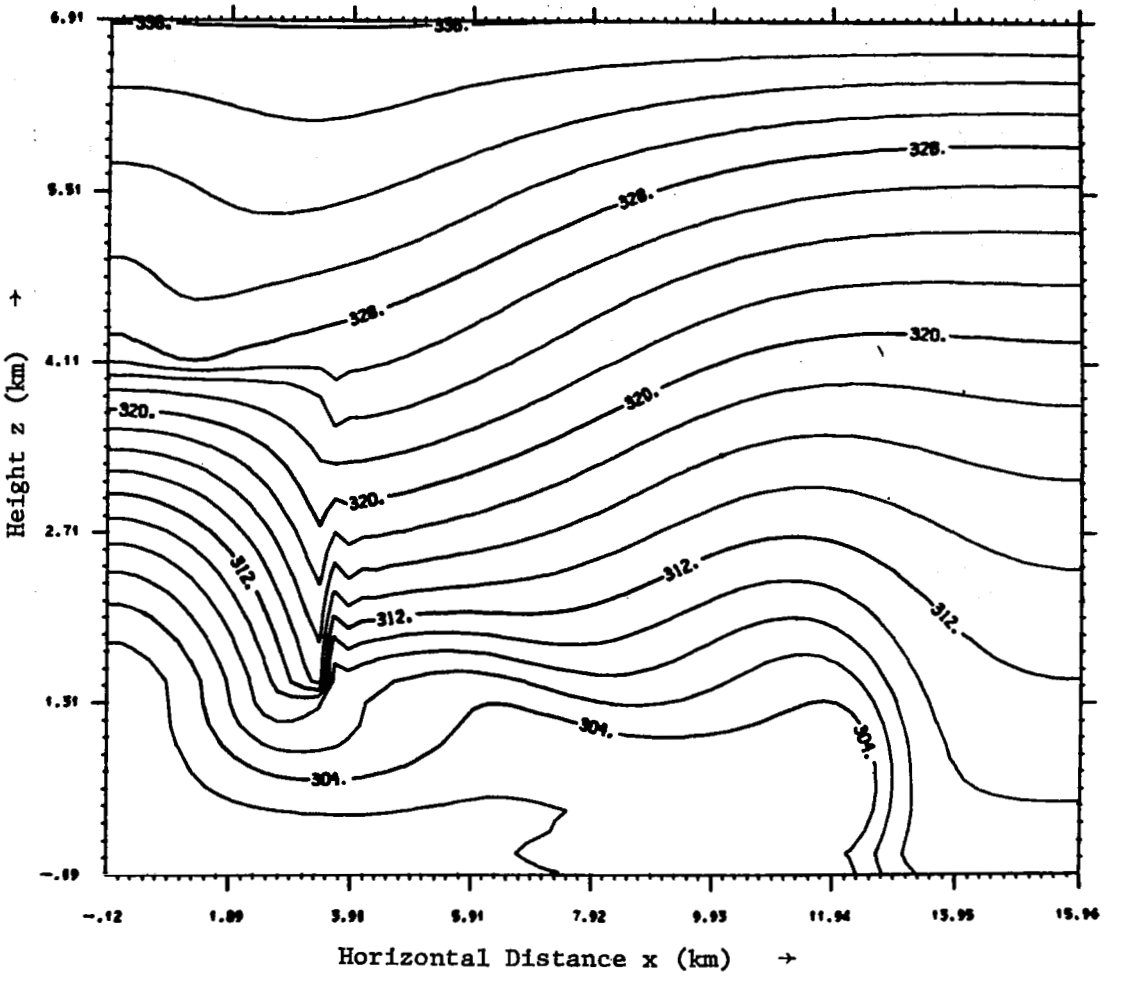

Figure 48. The potential temperature field (K) at 12.00 minutes for the stable case in which $\omega = 1.25 \times 10^{-2}$ sec^{-1}. The cold outflow exhibits a maximum depth of 2.10 km. Contour interval is 2.0 K.

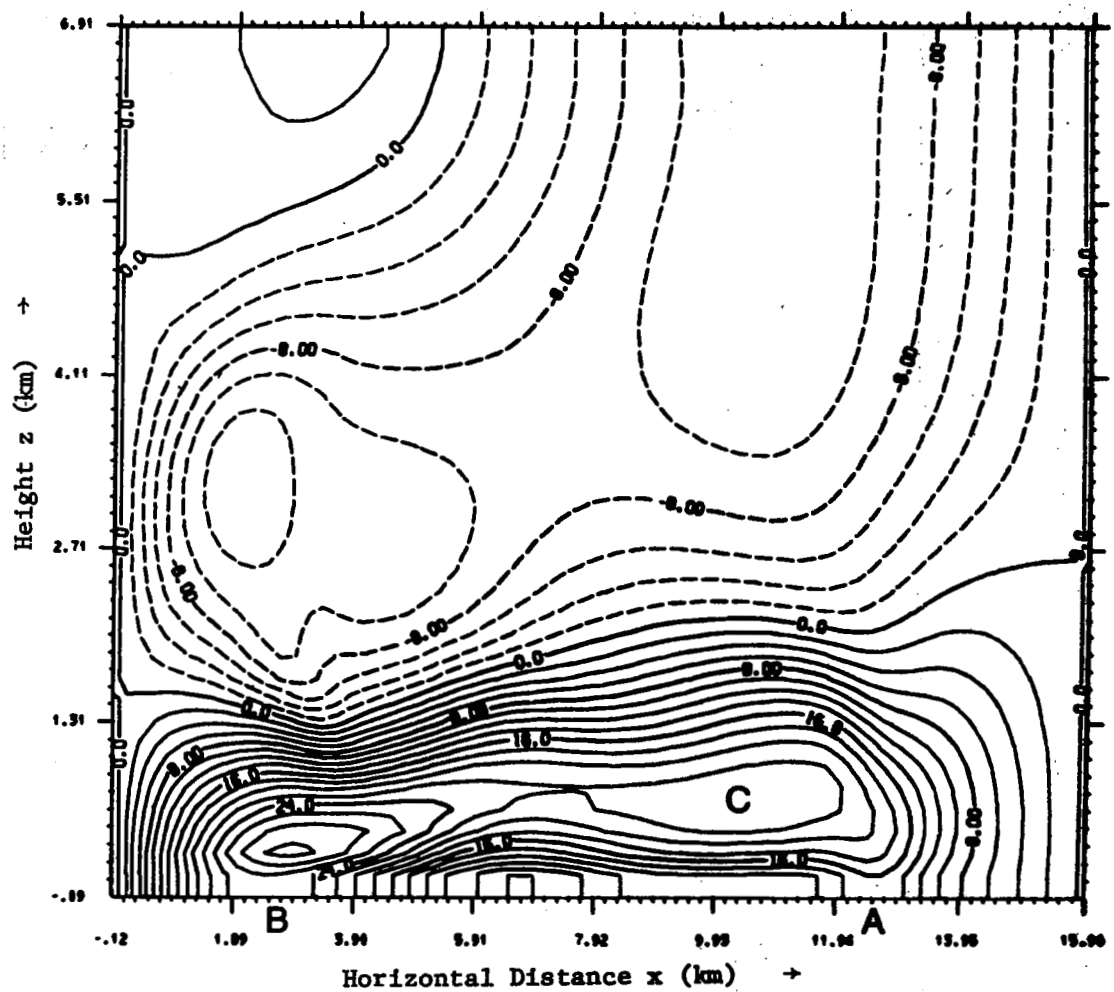

Figure 49. The horizontal wind field (m/sec) at 12.00 minutes for the stable case in which $\omega = 1.25 \times 10^{-2}$ sec^{-1}. The core of maximum winds above the surface (labeled C) is observed at a maximum height of 0.80 km. Contour interval is 2.0 m/sec.

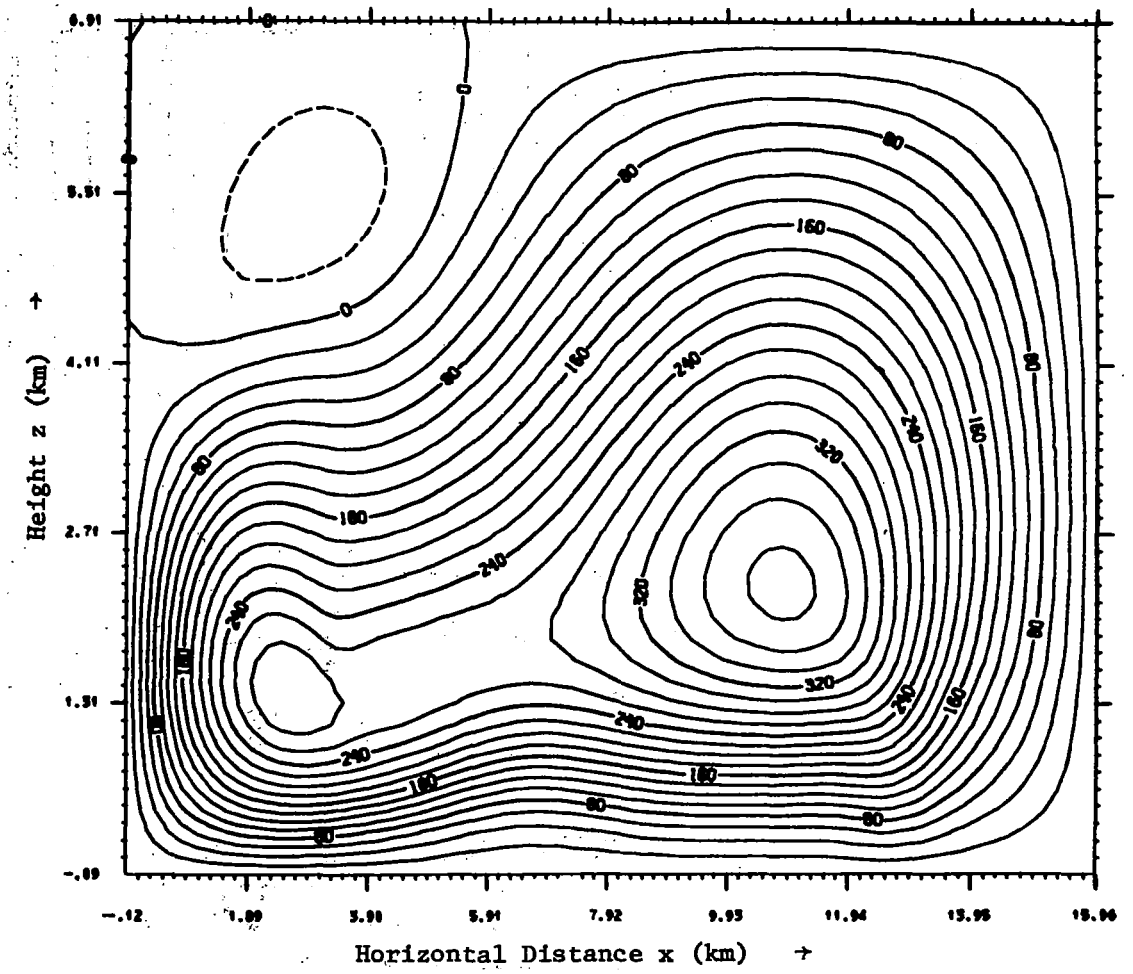

Figure 50. The streamline flow pattern at 12.00 minutes for the stable case in which $\omega = 1.25 \times 10^{-2}$ sec^{-1}. Solid streamlines depict counterclockwise flow. Contour interval is 2.0×10^{7} cm^2/sec and labels are scaled by 1.0×10^{-6}.

Figure 46 to Figure 23, where it is observed that the surface wind maximum is larger in the purely neutral case than in the case in which a 12 K temperature drop existed across the front in Section 4.1.

In the stable case (Figure 50), there is only a very slight rebounding of the downdraft at the surface and therefore, the coldest air is advected out along the surface and is not carried aloft. Consequently, the streamline pattern shows almost purely horizontal flow within the cold surge, as the stable stratification strongly limits upward motion.

The gust front of the special inversion case did not exhibit any unique features. This case was assigned an ω value of 1.0×10^{-2} sec^{-1} in Figures 43 and 44 because it exhibited a structure with characteristics similar to both the stable cases in which $\omega > 1.0 \times 10^{-2}$ sec^{-1}, and to the unstable cases, in which $\omega < 1.0 \times 10^{-2}$ sec^{-1}. It was very similar to the stable cases in that it was fairly shallow and close to the ground. But, it was also more intense like the unstable cases, since a greater temperature contrast existed across the front.

In general, the other tendencies that were observed in the stability experiments can be attributed to the differences in the temperature contrast across the front. The neutral and nearly neutral cases are characterized by more intense wind surges and by stronger winds in the wind core aloft. This is because the maximum downdraft temperature depression in these cases is not significantly affected by the adiabatic warming, and therefore a larger thermal contrast results across the front.

Dry-adiabatic warming may affect the evaporative cooling process in actual thunderstorm downdrafts. Caplan (1969) argued that air parcels descending in a rain-cooled downdraft rarely descend moist adiabatically because the right combination of rainfall rate and droplet size spectrum

required for saturated descent in a given humidity-temperature regime probably occurs infrequently. In the real atmosphere then, depending on the extent to which dry-adiabatic warming occurs in convective downdrafts, the ambient stability may significantly affect the cooling potential of the evaporation process and therefore affect the intensity of the resulting gust front. The ambient stability, in any case, will strongly influence the height scale of the gust front and cold surge.

5.0 CONCLUSION

The thunderstorm gust front is an intense wind surge at the leading edge of the cold outflow from a thunderstorm. The sudden onset of the front with its strong winds presents a significant hazard for aviation. But efforts to develop techniques for prediction of the arrival or intensity of the gust front have been largely unsuccessful, for two related reasons. First, because of the small scale of the gust front, the collection of observed data is too limited to suggest a coherent picture of its structure. Second, little knowledge about the dynamics of the gust front has been established in the absence of this empirical guidance. These same reasons motivated the development of a numerical model of the thunderstorm gust front.

A non-hydrostatic, primitive equation model was utilized in this attempt to study the dynamics and structure of the gust front. The model included sound waves, but they were strongly damped by a high frequency filter that left the gravity wave modes virtually untouched. To resolve the small scale features, a fine resolution grid was used. The model was very stable computationally and conserved mass and energy as well. The chief limitation was the short time step necessitated by the non-hydrostatic degree of freedom.

The effect of evaporative cooling in producing a vigorous downdraft was parameterized by an arbitrary local cooling function. This function was applied to produce a steady downdraft of cold dense air to drive the cold outflow and associated gust front.

5.1 Summary of Results

The model gust front and associated cold outflow provided a classic example of a direct circulation. The cold air in the downdraft was rapidly accelerated downward by gravity and spread out horizontally upon reaching the surface. The larger hydrostatic weight of this dense air relative to the ambient air produced a large surface pressure gradient that rapidly accelerated a strong outward flow of cold air away from the downdraft region.

This horizontal current of cold air passed through a relatively brief transient stage and then achieved a distinct quasi-steady configuration described here as the mature stage. This stage represented a dynamic balance between the pressure gradient forces and the surface drag forces.

The real feature of interest was the strong wind surge wall, called the gust front, which accompanied the forward edge of the cold outflow. Its main characteristic was an extreme horizontal shear of wind speed on the order of 10 m sec^{-1} km^{-1}. Given the typical gust front propagation speed in the model of 20 m/sec, this wind shear produced a rapid increase of wind speed from nearly zero to 20 m/sec in 3 or 4 minutes as the front passed a fixed point.

This wind surge was maintained against the decelerations of surface drag mainly by a large local pressure gradient associated with the forward edge of the cold outflow. The extremely rapid transition from warm to cold air, plus the added depth of the cold air at the front due to an elevated head, combined to produce the large pressure gradient at the front. The strong winds near the surface at the front were also supported by a downward transport of momentum from the stronger winds aloft. This

was accomplished by the relative maximum of downward motion of the coldest air behind the density interface of the front.

After the gust front passed, surface friction caused a rapid decrease of surface wind speeds since the horizontal pressure field behind the front was nearly flat. Thus, surface friction produced a distinct wind velocity jump at the front.

Since the surface winds behind the front were significantly retarded, a core of maximum winds was consistently observed between the downdraft and the front at about 700 m above the surface. This feature represented the strongest forward current of cold air within the cold outflow and was driven by the large horizontal pressure gradient that existed under the cold downdraft. Between the surface and the level of this maximum wind core, strong vertical shears around 20 m sec^{-1} km^{-1} were consistently observed.

These large vertical shears of horizontal wind speed observed upstream from the front were not observed at the gust front itself. Although the maximum winds aloft behind the front were consistently faster than the front propagation speed, it was shown that the trajectories of the fastest moving air parcels curved shaprly upward at the front forming an elevated head or upward bulge of cold air. The circulation theorem was used to show that large solenoidal accelerations at the front produced a positive circulation acceleration, which supported this upward deflection of air parcels.

The positive circulation was evident in the large gradients of upward motion, which dominated the small vertical shears of the horizontal wind at the front. Thus, the isotachs of horizontal wind speed were

nearly vertical at the front, as was the density interface. Consequently, no large protruding nose of cold air extended over a retarded surface front since the horizontal winds were nearly constant with height. In relation to this, the propagation speed of the gust front was found to be strongly correlated to the maximum surface wind speed accompanying the front. This would not be true if the frontal interface aloft traveled significantly faster than the front at the surface.

Even for large values of the drag coefficient, the solenoidal accelerations at the front balanced the effects of surface friction, and the cold surge front still quickly achieved the typical quasi-steady configuration of the mature stage. In virtually all model trials, then, no cyclic process of formation and collapse of a protruding nose of cold air was apparent.

Thus, the geometric shape of the density interface of the cold surge was constant during the mature stage. It was characterized by a nearly vertical slope in the low levels, and then rose to form an elevated head or crest of cold air. Upstream from the crest, the cold surge boundary sloped downward and tended to level off to a near constant depth. The cold outflow was typically shallow, usually having a depth of only 2.0 to 2.5 km.

The basic structure of the gust front was not affected by generating colder air in the downdraft. However, the maximum downdraft temperature depression was an important parameter to consider in determining the intensity of the resulting gust front. Colder downdrafts resulted in deeper cold outflows, stronger winds in the maximum wind core aloft, stronger peak surface winds, stronger vertical and horizontal shears, and faster front propagation speeds. The stronger peak surface wind

and the faster front propagation speed resulted in a more intense wind surge or wind velocity jump because at a point the stronger peak winds were attained over a shorter time interval.

The stability of the ambient air was also found to be an important parameter. It was the dominant factor in determining the depth of the cold outflow, and therefore, the vertical extent of the gust front. In addition, if the evaporatively cooled air in a thunderstorm downdraft does not descend strictly moist adiabatically, then the ambient stability may in large part determine the final density contrast across the front. This in turn, as mentioned above, will affect gust front intensity.

5.2 Suggestions for Further Research

Any subsequent attempts to model the thunderstorm gust front might consider several options to either enhance the efficiency of the numerical computations or to include more of the physics associated with the gust front phenomenon.

A variable vertical grid spacing could be incorporated to greatly improve the resolution in the lowest two kilometers. Only a crude resolution is necessary in the upper levels to maintain the rather uniform return flow of the direct circulation.

The short time step required in the model was very costly and prevented extensive experimentation. Comparative numerical integrations could be performed with a hydrostatic primitive equation system or an anelastic system in which $\frac{\partial \rho}{\partial t} = 0$ to see if such models could produce similar results more efficiently. Even an incompressible system applicable to shallow convection could be tried for comparison; although

results given here suggest that since the negative convection of the downdraft is fairly deep, shallow convection assumptions may not be applicable.

The physics could be improved by considering an ambient vertical wind shear to study the possible role of the downdraft in transferring higher momentum air from mid-tropospheric levels into the cold outflow. Also a more sophisticated treatment of the boundary layer in which direct attention is given to non-linear eddy viscosity would be beneficial.

Ultimately, the microphysics of evaporative cooling in the downdraft will have to be explicitly treated. However, to do this realistically without modeling the entire convective cell would be difficult; but to model the entire convective cell and still retain enough resolution to explicitly examine gust front structure would be a tremendous challenge. Yet, such a treatment with a fully three-dimensional model might be necessary to completely understand the evolution of the thunderstorm gust front.

REFERENCES

Asselin, R., 1972: Frequency filter for time integrations. Mon. Wea. Rev., 100, 487-490.

Ball, F. K., 1960: A theory of fronts in relation to surface stress. Quart. J. Roy. Meteor. Soc., 86, 51-66.

Benjamin, T. B., 1968: Gravity currents and related phenomena, Part 2. J. Fluid Mech., 31, 209-248.

Berson, F. A., 1958: Some measurements of undercutting cold air. Quart. J. Roy. Meteor. Soc., 84, 1-16.

Browning, K. A., 1964: Airflow and precipitation trajectories within severe local storms which travel to the right of the winds. J. Atmos. Sci., 21, 634-639.

Browning, K. A., 1968: The organization of severe local storms. Weather, 23, 429-434.

Caplan, P. M., 1969: On thunderstorm downdrafts. Proc. Sixth Conf. on Severe Local Storms, Am. Meteor. Soc., Boston, Mass., 68-70, (unpublished manuscript).

Charba, J., 1972: Gravity current model applied to analysis of squall-line gust front. National Severe Storms Laboratory, NOAA Tech. Memo. ERL NSSL-61, 58 pp.

Clarke, R. H., 1961: Mesostructure of dry cold fronts over featureless terrain. J. Meteor., 18, 715-735.

Colmer, M. J., 1971: On the characteristics of thunderstorm gust fronts. Royal Aircraft Est., Bedford, Eng., 11 pp.

Daly, B. J. and W. E. Pracht, 1968: Numerical study of density-current surges. Phys. Fluids, 11, 15-30.

Fawbush, Lt. Col. E. J. USAF and Maj. R. C. Miller USAF, 1954: A basis for forecasting peak winds in non-frontal thunderstorms. Bull. Am. Meteor. Soc., 35, 14-19.

Foster, D. S., 1958: Thunderstorm gusts compared with computed downdraft speeds. Mon. Wea. Rev., 86, 91-94.

Fujita, T., 1959: Precipitation and cold-air production in mesoscale thunderstorm systems. J. Meteor., 16, 454-466.

(REFERENCES (Continued)

Goldman, J. L., 1969: A numerical model of three-dimensional thunderstorm outflow. Proc. Sixth Conf. on Severe Local Storms, Am. Meteor. Soc., Boston, Mass., 71-74, (unpublished manuscript).

Goldman, J. L. and P. W. Sloss, 1969: Structure of the leading edge of thunderstorm cold-air outflow. Proc. Sixth Conf. on Severe Local Storms, Am. Meteor. Soc., Boston, Mass., 75-79, (unpublished manuscript).

Haltiner, G. J., 1971: Numerical Weather Prediction, New York, John Wiley and Sons, 317 pp.

Idso, S. B., R. S. Ingram, and J. M. Pritchard, 1972: An American haboob. Bull. Am. Meteor. Soc., 53, 930-935.

Keulegan, G. H., 1958: Twelfth progress report on model laws for density currents; the motion of saline fronts in still water. U. S. National Bur. Standards, Rept. No. 5831, 28 pp.

Lawson, T. J., 1971: Haboob structure at Khartoum. Weather, 26, 105-112.

Middleton, G. V., 1966: Experiments on density and turbidity currents; Part I., Motion of the head. Can. J. Earth Sci., 3, 523-546.

Newton, C. W., 1966: Circulation in large sheared cumulus. Tellus, 18, 699-711.

Operations Staff, 1971: The NSSL surface network and observations of hazardous wind gusts. National Severe Storms Laboratory, NOAA Tech. Memo, ERL NSSL-55, 18 pp.

Pearson, R. A., 1973: Properties of the sea breeze front as shown by a numerical model. J. Atmos. Sci., 30, 1050-1060.

Schlesinger, R. E., 1973: A numerical model of deep moist convection; Part II., A prototype experiment and variations upon it. J. Atmos. Sci., 30, 1374-1391.

Shuman, F. G., 1962: Numerical experiments with the primitive equations. Proc. Intern. Symp. Numerical Weather Prediction in Tokyo, Nov. 7-13, 1960, Meteor. Soc. of Japan, 85-107.

Shuman, F. G. and J. B. Hovermale, 1968: An operational six-layer primitive equation model. J. Appl. Meteor., 7, 525-547.

REFERENCES (Continued)

Simpson, J. E., 1969: A comparison between laboratory and atmospheric density currents. Quart. J. Roy. Meteor. Soc., 95, 758-765.

Sinclair, R. W., 1973: Variation of the low level winds during passage of a thunderstorm gust front. Master's thesis, The Pennsylvania State University, 87 pp.

Syono, S. and T. Takeda, 1962: On the evaporation of raindrops in a sub-cloud layer. J. Meteor. Soc. of Japan, 40, 245-265.

*U.S. GOVERNMENT PRINTING OFFICE: 1975 - 635-275/49